Progress in Energy and Combustion Science 59 (2017) 1–31

Contents lists available at ScienceDirect

Progress in Energy and Combustion Science

journal homepage: www.elsevier.com/locate/pecs

Tomographic absorption spectroscopy for the study of gas dynamics and reactive flows

Weiwei Cai[a,b], Clemens F. Kaminski[b,*]

[a] School of Mechanical Engineering, Shanghai Jiao Tong University, Shanghai 200240, China
[b] Department of Chemical Engineering and Biotechnology, University of Cambridge, Cambridge CB2 3RA, UK

ARTICLE INFO

Article History:
Received 4 June 2016
Accepted 12 November 2016

Keywords:
Flow diagnostics
Absorption spectroscopy
Classical tomography
Nonlinear tomography
Reactive flows
Engine testing
Frequency-agile spectroscopy

ABSTRACT

Optical imaging techniques are ubiquitous for the resolution of non-uniformities in gas flows. Planar imaging techniques such as laser-induced fluorescence are well established and applied extensively in turbulent reactive flows, offering both high temporal and spatial resolutions. However, planar imaging suffers from a critical disadvantage, the requirement for spatially continuous optical access over large solid angles in both the excitation and detection paths and this precludes their application in many practical situations, for example those encountered in engine testing. Tomographic absorption spectroscopy, TAS, on the other hand, shares many of the advantages of planar imaging techniques but reduces the demands for optical access, because high quality data can be obtained with sparsely sampled volumes. The technique has unrivalled potential for imaging in harsh environments, for example for in-cylinder/in-chamber engine measurements. TAS is beginning to mature as a technique for the simultaneous imaging of temperature and species concentration, and is experiencing a surge of interest due to progress in laser technology, spectroscopy, and theoretical developments of nonlinear tomography techniques. The recent advancements in broad bandwidth, frequency-agile laser sources massively enrich the spectral information obtainable in TAS. Furthermore, nonlinear tomography enables the recovery of multiplexed information from a single tomographic inversion. The utilization of multispectral information improves the immunity of TAS to experimental noise and makes possible the simultaneous imaging of temperature, pressure, and multiple species. Nonlinear tomography can also be used to empower the imaging potential of sensitive and robust absorption techniques, such as wavelength modulation spectroscopy, for use in harsh and even optically dense environments. In combination, this greatly extends the applicability of TAS for more general and harsh scenarios in combustion technology. In this article we review basic concepts and mathematical foundations of classical absorption tomography, proceeding to more advanced recent concepts based on nonlinear tomography, and providing an extensive review of experimental demonstrations and practical applications in the context of state-of-the-art combustion research.

1. Introduction

Combustion remains the dominant form of energy production in use today, and is an underpinning factor for modern society [1,2]. This dominance is expected to continue for several decades into the future and thus a full understanding and effective control of combustion processes is of paramount importance to improve energy efficiency and to reduce the formation of pollutant species such as particulates, NO_x, SO_x, and greenhouse gases [3,4]. Key to an understanding of combustion is an ability to measure chemical and physical flow parameters at high temporal and spatial resolution, and to untangle the complex interplay between flow dynamics, chemical kinetics, and heat and mass transfer, which remains a formidable scientific challenge to this day [5]. There are several key parameters such as temperature, species concentration, equivalence ratio, heat release rate, and velocity, the quantification of which is essential to any such effort, and requires their measurement under physically realistic conditions. Numerous non-invasive optical sensing techniques have been developed during the past decades for the diagnosis of reactive flows. For simple laminar flames, such as laboratory McKenna and Bunsen flames, point measurement techniques can be used for the measurement of temperature, such as laser induced grating spectroscopy (LIGS) [6], coherent anti-Stokes Raman scattering (CARS) [7–10], and two-line atomic fluorescence thermometry (TLAF) [11–16]; Laser Doppler velocimetry (LDV) [17,18] for point measurements of local velocity; line-of-sight-averaged techniques such as tunable diode laser absorption spectroscopy (TDLAS) [19,20] for the simultaneous retrieval of temperature, species concentration and pressure; and cavity enhanced techniques (CEAS) [21–26] for

* Corresponding author.
E-mail address: cfk23@cam.ac.uk (C.F. Kaminski).

http://dx.doi.org/10.1016/j.pecs.2016.11.002
0360-1285/

Nomenclature

p	line-of-sight-integrated absorbance
R [a.u.]	radius of the region of interest
r [a.u.]	distance to the origin
$f(r)$	spatial distribution of absorbance along the radial direction
η	an integration variable
l	laser beam path
x, y	x and y coordinates
Θ [rad]	angle between beam path and x axis
t [a.u.]	distance from origin to the beam path
$\vec{x}$	image pixel values arranged in a vector format
I	total number of beams
J	total number of pixels
$A_{I\times J}$	weight matrix
$\vec{a}_i$	the ith row of A
β	relaxation factor
Θ	a linear operator
$\vec{\Phi}_k$	eigenfunctions
ζ	eigenvalues
L	regularization operator realized in a matrix format
g	regularization factor
R	resolution matrix
I	identity matrix
$\vec{\Psi}$	a vector of complex numbers
R_j	ratio of integrated absorbance at two transitions of the jth pixel
μ	spatial distributions of the flow parameters
Π	a function describing a physical process
Δ	grid spacing
T [K]	temperature
X	absorber concentration
P [atm]	pressure
LIGS	laser-induced grating spectroscopy
TLAF	two-line atomic fluorescence thermometry
TDLAS	tunable diode laser absorption spectroscopy
PLIF	planar laser-induced fluorescence
LIPS	laser-induced phosphorescence spectroscopy
LOS	line-of-sight
ABNT	absorption-based nonlinear tomography
CFWMS	calibration-free wavelength modulation spectroscopy
TPA	three-point Abel
ART	algebraic reconstruction technique
SR	spatial resolution
LSF	line spread function
ESF	edge spread function
ROI	region of interest
MART	multiplicative algebraic reconstruction technique
TRKB	tomographic reconstruction via Karhun-Loeve basis
TSLs	tunable semiconductor lasers
QCLs	quantum cascade lasers
DBR	distributed Bragg reflector
CA	crank angle
α	absorption coefficient
p_c	computed projection
p_m	measured projection
R_T	regularization term for T distribution
R_X	regularization term for X distribution
γ_T	regularization factor for R_T
γ_X	regularization factor for R_X
a [cm^{-1}]	modulation depth
ν [cm^{-1}]	laser frequency
I [a.u.]	laser intensity
i_0 [a.u.]	linear modulation amplitude
i_2 [a.u.]	nonlinear modulation amplitude
σ_m	std of measurement noise
f_m [kHz]	modulation frequency
ψ_1 [rad]	linear phase shift with respect to frequency modulation
ψ_2 [rad]	nonlinear phase shift with respect to frequency modulation
S [cm^{-2}/atm]	line strength
H_k	kth order harmonic coefficients
τ	transmittance
S_{1f} [a.u.] S_{2f} [a.u.]	1st and 2nd orders of harmonic signals
G	scaling factor accounting for electrical and optical gains
$\bar{I}_0$ [a.u.]	average laser intensity at the line-center
F	cost function
T_{SA}	temperature parameter in the simulated annealing algorithm
ξ	annealing rate
e_T, e_X	normalized temperature and concentration errors
T^{true} [K] T^{rec} [K]	ground truth and reconstructed temperature
X_1, X_2	concentration for a two-zone problem
T_1 [K], T_2 [K]	temperature for a two-zone problem
CARS	coherent anti-Stokes Raman scattering
LDV	laser Doppler velocimetry
CEAS	cavity enhanced absorption spectroscopy
PIV	particle imaging velocimetry
FRS	filtered Raman scattering
TAS	tomographic absorption spectroscopy
CAT	classical absorption tomography
SNR	signal-to-noise ratio
FBP	filtered back-projection
MLEM	maximum likelihood expectation maximization
AART	additive algebraic reconstruction technique
SIRT	simultaneous iterative reconstruction technique
MTF	modulation transfer function
PSF	point spread function
DFT	discrete Fourier transform
FDML	Fourier domain mode-locking
TDLs	tunable diode lasers
DFB	distributed feedback
TDC	top dead center
DAS	direct absorption spectroscopy
POD	proper orthogonal decomposition
SA	simulated annealing

the detection of minor flame species with the highest sensitivity. Spatial variations of these scalar quantities can be measured by consecutive measurements in steady laminar flames. However, for more complicated combustion phenomena such as turbulent model flames, ignition, flashback, and supersonic/hypersonic reactive flows, which evolve rapidly and feature scalar gradients, the aforementioned techniques are inadequate and imaging techniques with high temporal resolution are required.

Generally, one can classify imaging techniques into two categories, namely planar and tomographic imaging.

In the former, a specific plane within the flow field is illuminated with light from a pulsed laser source, and the ensuing signal e.g. from Mie [27], Rayleigh [28], and Raman scattering, phosphorescence [29], or fluorescence [30] can then be captured *via* 2D array detectors, often intensified CCD cameras. In most implementations, the signals thus received scale linearly with excitation intensity. Examples of planar imaging techniques include planar laser-induced fluorescence (PLIF) [31–34], particle imaging velocimetry (PIV) [35], and laser-induced phosphorescence spectroscopy (LIPS) [29,36–38]; and filtered Rayleigh scattering (FRS) [28], etc. Volumetric information can be recovered through the sequential scanning of multiple parallel planes [39,40]. The characteristic physical quantities describing the flows such as the profiles of temperature [41–44], velocity [45–49], and mixture fraction [50–52] can then be inferred from the obtained images. For example, two-line atomic fluorescence (TLAF) [53–55] measures the florescence signals of two transitions from the ratio of which temperature can be extracted; and similarly simultaneous imaging of CH_2O and OH yield heat release rate in premixed flames [56–59]. For ultimate spatial resolution, planar imaging techniques are indispensable, offering snapshots of flame chemistry over spatial scales down to tens of micrometers with ns temporal resolution and kHz repetition rate [34,60–66]. Such capability is essential for the resolution of the characteristic length scale of flow turbulence and its interplay with chemical kinetics [67–76]. However, the requirement for optical access often makes them inapplicable in practical flame environments, for example the combustion chamber of an automotive engine or a ramjet/scramjet. Optical engines have been designed and fabricated to mitigate this drawback; nevertheless, the mechanical properties of the original engines cannot be fully replicated. In addition, due to their high costs, optical analogs are impractical to implement for many engine models. Thus, planar imaging techniques are ideal for the measurements of model flames for computational model validations, but less suited in the practical design of better practical combustion technologies.

Tomography is the other imaging category, and here some of the latter disadvantages are less prominent. In tomography one reconstructs scalar fields from multiple projections, which represent signal integrals along various directions [77]. For applications in which optical access is ample and where volumetric illumination is possible, tomographic reconstructions of 3D fields can be realized without spatial sweeping of the illumination fields and thus without associated loss of time. Examples of volumetric tomography techniques in combusting flows include tomographic PIV for volumetric velocimetry [78,79], tomographic X-ray imaging for fuel mass distributions [80,81], tomographic emission spectroscopy of either radicals or soot distribution [82–84], tomographic deflectometry [85–89], and tomographic interferometry [90–97] for imaging of refractive index, which can then be used to infer temperature distributions. There is great potential also to implement other techniques of value to the combustion community into tomographic variants. For example, tomographic laser-induced phosphorescence could be conceived by combining the work presented in [36] and tomography, hence one could envisage the simultaneous measurement of volumetric temperature and velocity distributions. On the other hand, for applications with limited optical access, planar tomographic variants can be implemented. With both the illumination and detection arranged in the same plane, the requirement for optical access can be greatly reduced. In difference to planar imaging, in which the target field is radiation intensity, the object field of tomography can be other physical quantities, such as absorption/extinction coefficients and refractive indices of flows. For example, absorption spectroscopy can be combined with tomography to image the fields of absorption coefficients of the absorbing species at two or more transitions; the fields can then be processed to simultaneously recover temperature and species concentration fields [98]. A brief review of tomographic techniques for flame diagnostics has been presented in Ref. [99]. Also, tomographic PIV has been the subject of several review articles [100–102] and book chapters [103,104]. Table 1 summarizes the various tomographic techniques discussed so far and their applications in combustion research. The table also lists the range of years over which the cited papers have been published, to give an indication of research trends that have emerged over time.

Among all tomographic methods, tomographic absorption spectroscopy (TAS) is the most promising for engine diagnostics, since it does not require spatially continuous optical access, and mechanical modifications (e.g. the drilling of holes) are minimal to adapt engines for TAS. TAS also offers high species specificity and can be sensitive. These features make TAS a powerful and attractive complement to planar imaging techniques for technical combustion research. The aim with this review is to provide a comprehensive summary of both classical absorption tomography (CAT) and also the newly emerging absorption based nonlinear tomography (ABNT) methods for the study of gas dynamics and reactive flows. As indicated by its name, CAT is an implementation of classical tomography [105], where one records projections for one or two optical transitions along various directions, resulting in the recording of so called sinograms. Sinograms can be recorded from multiple line-of-sight measurements across a lateral plane through the sample volume, recorded, for example on a line detector (2D tomography). Using an array detector one can record several such planes at once (3D tomography), as demonstrated in [82,106,107] for chemiluminescence. In either case,

Table 1
Summary of optical tomographic techniques for flow diagnostics.

Name	Measurand	Projection	Applications	References	Year range
Tomographic absorption spectroscopy (TAS)	Absorption coefficient	Absorbance	Temperature, concentration, and pressure	[123–129]	1980–2016
Tomographic emission spectroscopy	Flame radiation	Light intensity	Equivalence ratio and heat release rate	[106,130–138]	1985–2016
Tomographic laser-induced fluorescence	Laser-induced fluorescence	Light intensity	Temperature, concentration, and fuel/air ratio	[139–141]	2015–2016
Tomographic particle imaging velocimetry	Mie scattering	Light intensity	Velocity	[78,79,142,143]	2005–2016
Tomographic interferometry	Refractive index	Fringe shift	Density, concentration, and temperature	[90–97,144]	1994–2015
Tomographic deflectometry	Refractive index	Deflection angle	Density, concentration, and temperature	[85–89,145,146]	1981–2016
Tomographic X-ray imaging	Extinction coefficient	X-ray transmission	Density	[80,81,147–151]	2003–2015

sinograms are obtained which are post-processed to obtain the distributions of fundamental parameters such as temperature and species concentration [108,109]. Since in a CAT process the target field is linearly related to the LOS measurements, i.e. the latter are the line integrals of the former, it is also referred to as absorption-based linear tomography. Theoretically, to make the equation system well-posed, a large number of projections are required to obtain a sufficient number of equations. However, for practical engine measurements only a few projections are usually available due to limited optical access and hence the obtainable linear equation system often becomes rank-deficient [110,111]. To alleviate this problem, many algorithms that were originally developed for X-ray tomography techniques, where similar problems exist, have been adapted to CAT for combustion diagnostics [112,113]. For practical implementations, irregular beam arrangements ('regular' means the projections are arranged in an equiangular manner and the rays in each projection are equidistant) were also adopted. Such methods maximize the spatial sampling efficiency, but come at the cost of increased experimental complexity [114]. A further problem in classical tomography is that it necessarily is only applicable for measurands that are integratable (accumulative) along the LOS. This greatly limits its compatibility with more advanced variants of absorption techniques. For example, the calibration-free wavelength modulation spectroscopy (CFWMS) technique [115] cannot be combined with classical tomography in scenarios where the optical depth is thick [116], since in this case the harmonic signals cannot be linearized and the line of sight measurements do not represent the integrals of any physical quantity.

These and related shortcomings can be addressed and overcome by the recently proposed concept of nonlinear tomography [117,118]. Absorption based nonlinear tomography, ABNT, takes advantage of rich spectral information that becomes accessible through use of novel broad-bandwidth, wavelength-sweeping laser sources [117,118]. The extra information afforded by ABNT can enhance the immunity of the technique against noise and successful reconstructions with ABNT were recently demonstrated from only two orthogonal projections, when multiple absorption transitions were probed simultaneously. This would be difficult to achieve with CAT and opens the potential for ABNT to be used for engine measurements where optical access is restricted [119]. The simultaneous processing of information from a multitude of spectral transitions furthermore enhances the immunity of the technique against experimentally generated noise [120,121]. In addition, ABNT enables use of advanced, noise immune absorption techniques, such as CFWMS, which offers enhancements in signal-to-noise ratios, SNR, of 10–100 times over standard absorption techniques and is exempt from a requirement to fit baselines, offering immunity to laser intensity fluctuations. All these features are highly desirable for the harsh conditions prevailing in technical combustion systems [122]. Data from ABNT measurements are fed into a set of nonlinear equations from which temperature, species concentration, and pressure distributions can be recovered simultaneously [117]. In situations where optical access is ample, ABNT achieves a similar spatial resolution as CAT for the same number of projections, but offers improved immunity to noise [108]. However, ABNT is vastly superior to CAT in situations with restricted optical access. In summary, the advantages of ABNT are two-fold: first, it can accommodate more dimensions in the tomographic reconstruction (e.g. multiple spectral channels) and it works more robustly than CAT in data-limited situations, for example where the geometry of the combustor is restricted and, e.g., only two orthogonal projections can be retrieved; second, it allows a combination of tomographic reconstruction methods with absorption techniques such as CFWMS that are more advanced than possible with CAT. These advantages open the field of tomographic absorption imaging to extremely harsh environments such as coal-fired power plant boilers filled with flying ashes or those encountered during in-flight engine monitoring in the presence of vibrations, etc.

The purpose of this review is to give the reader a comprehensive introduction into the physical concepts behind absorption based tomographic imaging, exploring both theoretical and experimental concepts. State of the art applications in reactive flow imaging are reviewed and an outlook is given on potential developments in the field. The remainder of the paper is organized as follows: chapter 2 focuses on CAT and begins with foundations of tomographic imaging and an explanation of common inversion algorithms, before presenting experimental considerations and applications of CAT; similarly, chapter 3 includes the mathematical formulation, numerical studies, experimental demonstrations and applications of ABNT. The review concludes in Chapter 4 with a summary and an outlook on how the field might develop into the future.

2. Classical absorption tomography

Classical tomography originated from medical applications and was later extended to other industrial fields such as process engineering [152,153]. As indicated by the name, CAT is a combination of absorption spectroscopy with classical tomography, and reconstructs the distribution of absorption coefficients from integrated line-of-sight (LOS) measurements along various orientations i.e. projections. CAT was initially demonstrated in axi-symmetric flames [129,154] and later applied to more complicated flow scenarios to reconstruct spatial varitions across a measurement plane, e.g. the combustion process in an automotive engine [114,155,156]. In this chapter, we summarise the mathematical formulation, inversion algorithms, experimental implementations, and applications of CAT.

2.1. Algorithms for 1D classical absorption tomography

In some applications the scalar field to be investigated can be mathematically represented in terms of only one independent spatial variable, for example for a field that is rotationally symmetric. In this case, the projections along arbitrary orientations are equivalent. Thus a measurement of one single projection is sufficient to enable tomographic reconstruction of the field and this is called 1D tomography. The concept is illustrated in Fig. 1(a). For a target field that varies only along the radial direction, its spatial distribution can be described by a function $f(r)$ and the corresponding LOS measurements along the vertical line at x can be expressed as [157,158]:

$$p(x) = 2\int_x^R \frac{f(r)rdr}{\sqrt{r^2-x^2}} \tag{2.1}$$

The LOS signal $p(x)$ can be calculated from an absorption measurement using the Beer-Lambert law to be $p(x) = -ln[I_\lambda(x)/I_\lambda^0(x)]$, where $I_\lambda(x)$ and $I_\lambda^0(x)$ denote the measured transmitted and incident light intensities at the wavelength λ, respectively. There are a number of algorithms available to retrieve the field distribution $f(r)$ from Eq. (2.1), including two-point/three-point Abel transformation, the so called onion peeling algorithm [157–165], and finally the filtered back-projection algorithm [166], which will be introduced in detail in Section 2.2.1, because of its importance for non-axisymmetric tomography applications. These algorithms have been thoroughly reviewed and compared in Ref. [166] and for 1D applications the three-point Abel (TPA) transform wins, as it is the easiest to implement, the fastest to compute, and the least sensitive to noise of all three methods. The derivation of TPA is briefly summarized below for the reader's convenience.

The analytical inversion of Eq. (2.1) is known as the Abel transform [157]

$$f(r) = -\frac{1}{\pi}\int_r^R \frac{p'(x)dx}{\sqrt{x^2-r^2}} \tag{2.2a}$$

where $p'(x)$ denotes the gradient of the LOS signals along the x axis. As can be seen, $f(r)$ is encoded in the *variations* of the projection data

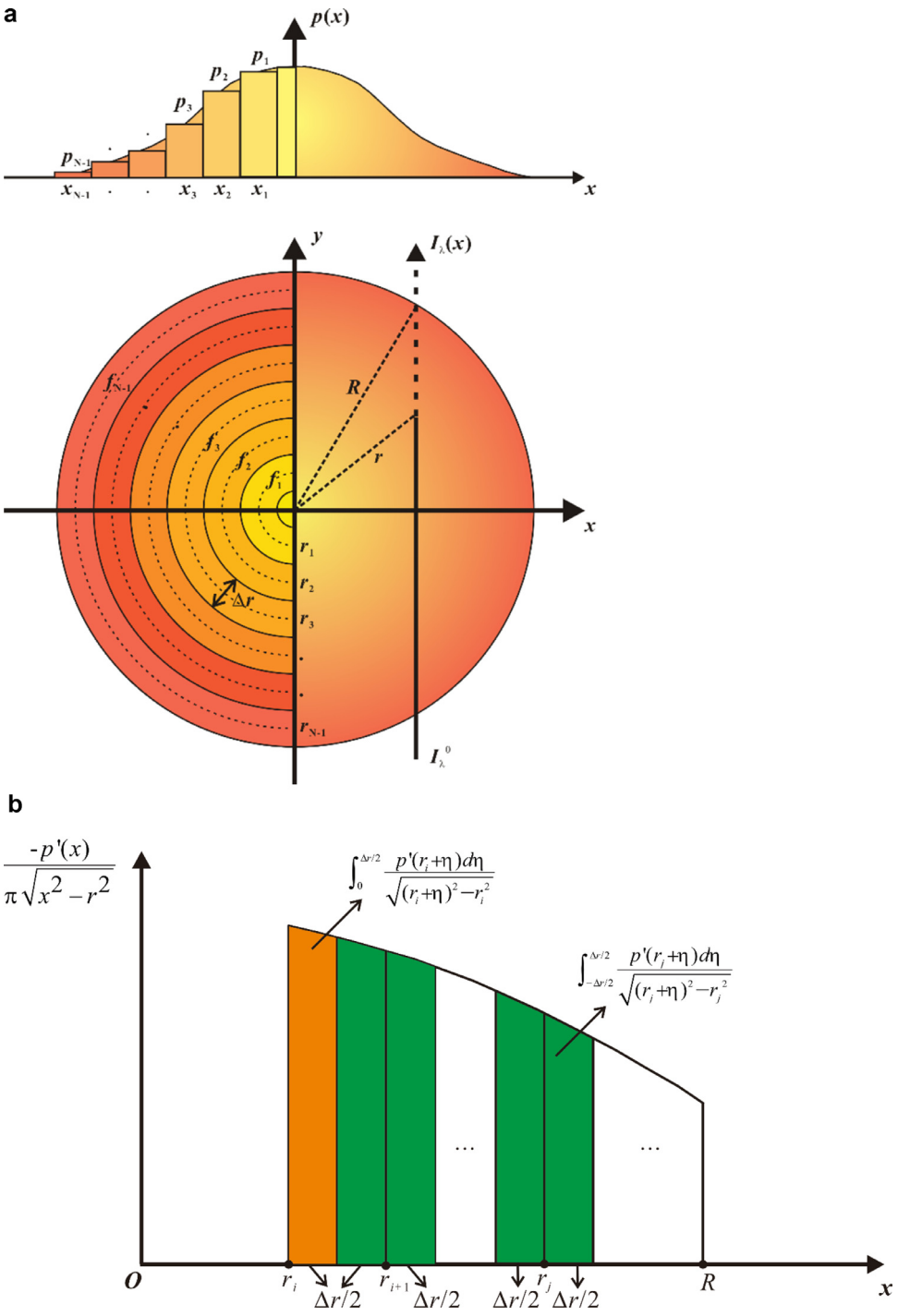

Fig. 1. (a) Axisymmetric geometry of a scalar field, $f(r)$ to illustrate the inversion algorithms. The region of interest shown in the bottom panel is discretized into annuli, and the corresponding LOS measurements along the vertical direction are plotted in the top panel. The figure was adapted from [158]. (b) Illustration of integration by segments (Eq. (2.2b)). The width of the first segment (the orange region) is $\Delta r/2$ and is Δr of other segments (the green regions). (For interpretation of the references to colour in this figure legend, the reader is referred to the web version of this article.)

i.e. $p'(x)$. As illustrated by Fig. 1(b), the Abel transform equals to the sum of segments which can be calculated according to

$$f(r_i) = -\frac{1}{\pi}\sum_{j=i}^{N-1}\int_{0.j=i}^{\Delta r/2}_{-\Delta r/2, j>i}\frac{p'(r_j+\eta)d\eta}{\sqrt{(r_j+\eta)^2-r_j^2}} \tag{2.2b}$$

where η is the integration variable. For TPA $p'(x_j)$ can be approximated using discrete values in a quadratic form as

$$p'(r_j+\eta) = [p(r_{j+1})-p(r_{j-1})]/(2\Delta r) + [p(r_{j+1})+p(r_{j-1})-2p(r_j)]\eta/\Delta r^2 \tag{2.3}$$

By combining Eqs. (2.2b) and (2.3), $f(r)$ can be analytically calculated for every r_i. A detailed review for the computational implementation of the TPA can be found in Ref. [166] and examples for its use to investigate axisymmetric flames are reviewed in Ref. [157].

2.2. Algorithms for 2D classical absorption tomography

In most applications, the field can only be adequately described with two independent variables. In this case, many projections are required for the reconstructions along various directions. The

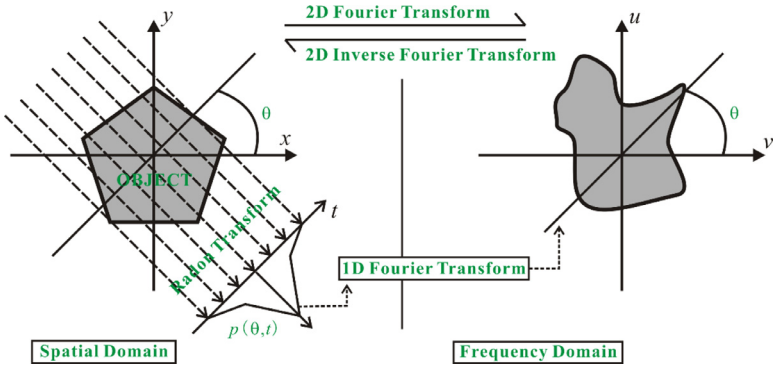

Fig. 2. Illustration of the central slice theorem and the filtered back-projection algorithm. The left panel defines the Radon transform and the right panel shows the sinogram in the Fourier space. The figure was adapted from [157], with the permission from American Inst of Aeronautics and Astronautics; and the permission is conveyed through Copyright Clearance Center, Inc.

recovery of the field as a function of two spatial variables is defined as 2D tomography. There are typically two categories of algorithms to perform 2D inversions, they are either analytical (or transform-based) or algebraic-iterative methods, respectively. The filtered back-projection (FBP) algorithm is an example of an analytical algorithm and has been widely applied in industrial X-ray tomography [167]. On the other hand, the algebraic-iterative methods formulate the inversion problem in a discrete manner and arrive at the solution through iterative computation. Examples include the algebraic reconstruction technique (ART) [168], the Landweber algorithm [114,169], the maximum likelihood expectation maximization (MLEM) algorithm, and variants thereof. Other algorithms such as the finite domain direct inversion method [170], adaptive finite domain direct inversion [171], level set method [172], and the low third derivative method [40,173] also exist, but are less widely used in practice. The basic working principles of the most important algorithms will be introduced in the following sub-sections.

2.2.1. Filtered back-projection algorithm

The filtered back-projection, FBP, algorithm is based on the analytical solution of the Radon transform [174–176], defined as

$$p(\theta,t)=\int_l f(x,y)dl \tag{2.4}$$

where $p(\theta,t)$ is the line-of-sight measurement at an inclination angle of θ with respect to the x-axis and located at a distance t from the origin as shown in Fig. 2; and l specifies an integration path. Obviously, p is a 2 dimensional function and it is of key importance in tomography. It is essentially the assembly of all projections into a 2D format. The process of recovering the original function f from p is the essence of classical/linear tomography. The foundation of the FBP algorithm lies in the so-called central slice theorem, which states that the Fourier transform of a projection at a specific angle is equivalent to one slice of the 2D Fourier transform of the field at that same angle, as illustrated in Fig. 2. Based on this theorem, the algorithm can be implemented in two steps: 1) take the Fourier transform of each projection sequentially and organize the results into a 2D map. The map then contains information of the original object in Fourier space; and 2) take the inverse Fourier transform of the map obtained to recover the object. However, due to the finite sampling size of the LOS measurements, the low frequency image information is amplified in the Fourier space. As a result, performing a direct inverse Fourier transformation usually results in image blur, even when the measured projections are free of noise. To de-blur the reconstruction, an additional step is included, namely the filtering of the original projection data. The entire operation is captured by the following equation:

$$f(x,y)=\underbrace{\underbrace{\int_0^{\pi}\int_{-\infty}^{+\infty}\underbrace{\int_{-\infty}^{+\infty}p(\theta,t)e^{-i2\pi wt}dt}_{\text{FT of a projection}}\underbrace{|w|}_{\text{filtering}}e^{i2\pi wt}dw\,d\theta}_{\text{inverse FT}}}_{\text{back-projection}} \tag{2.5}$$

where $|w|$ is a ramp filter used to remove blurring.

The FBP algorithm works well if a large number of projections are obtainable from the measurement object. One of its disadvantages is

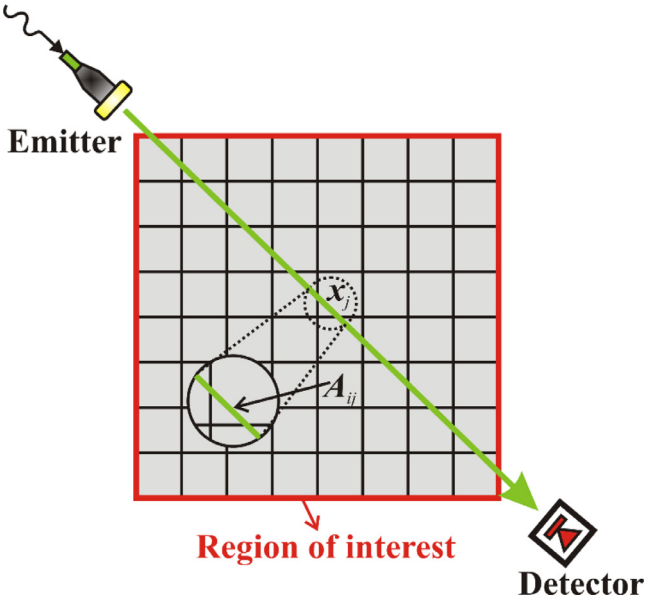

Fig. 3. Discrete formulation of the CAT problem. The region of interest is defined by the red square. The absorption length of the ith beam (the green line) within the jth pixel is labeled as A_{ij}. (For interpretation of the references to colour in this figure legend, the reader is referred to the web version of this article.)

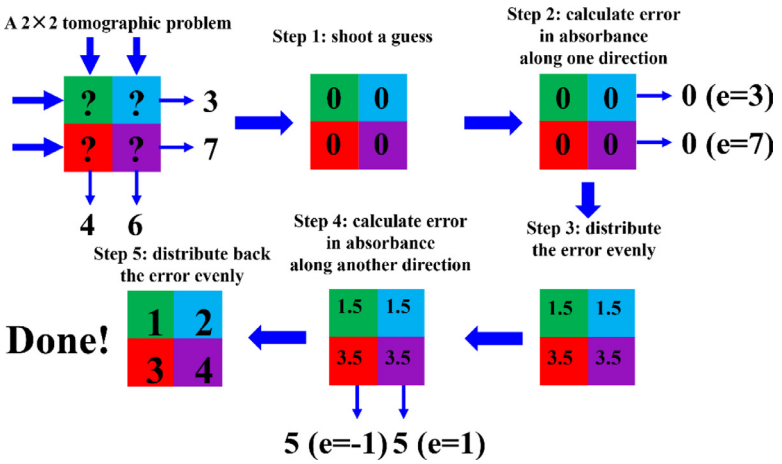

Fig. 4. Illustration of the working principle of the AART algorithm with one iteration step on a simple 2 × 2 tomographic problem sampled with two orthogonal projections.

that the projections need to be arranged at regularly spaced angles to permit the Fourier transformations [177]. Thus, FBP is recommended for applications where optical access is ample and many projections can be arranged freely along arbitrary orientations. Some example applications, ranging from simple flat flames to exhaust flows from scramjet combustors, where the FBP algorithm came to use, are found in Refs. [178–188].

2.2.2. Algebraic reconstruction technique

The CAT problem can also be formulated in a discrete format as illustrated in Fig. 3. For this purpose, the region of interest (ROI), to be probed in the measurement object is discretized into square pixels which are probed by numerous laser beams. One representative beam, with index i, is highlighted in green and the absorbance measured for it denoted as p_i. The absorption coefficient for the jth pixel in the sample is labeled as x_j and correspondingly the absorption length of the ith beam within the jth pixel as A_{ij}. The absorption lengths of all beams within every pixel can be compiled into an $I \times J$ matrix. The forward projection process can then be described by the following equation

$$\vec{p} = A_{I\times J}\,\vec{x} \tag{2.6}$$

where $\vec{p}$ and $\vec{x}$ represent the sinogram and the original map of the absorption coefficients, respectively, both organized in a vector format. Since the tomographic problem is here modeled with a linear equation system, classical tomography is also referred to as linear tomography. Intuitively, the system can be solved by either calculating the inverse of the matrix A or using Gaussian elimination. However, in practice, the available number of projections is always limited, which can lead to an underdetermined equation system, and because of noise, which is always present, the matrix A is typically ill-conditioned.

The ART algorithm is iterative and features several critical advantages that can overcome the ill-posedness of the tomographic problem typically encountered in combustion applications [68]. These advantages include 1) robustness in the presence of noise; 2) ability to reconstruct a field from a limited number of views; 3) ability to incorporate *a priori* information (e.g., smoothness or boundedness) into the formulation to improve reconstruction fidelity; and 4) the flexibility with the geometry of the projections which need not necessarily be arranged in an equiangular manner [112,123,124,189–200].

The ART algorithm is recommended for usage when the number of the LOS measurements is moderately small (ca. 100–1000). It is discrete in nature [60,77] and has numerous variants such as the additive ART (AART) [201] and multiplicative ART (MART) [39] algorithms, and the simultaneous iterative reconstruction technique (SIRT) [9,10,69], each with their own advantages in certain application domains. Among these, AART is the most widely used variant and is introduced in detail in the following paragraphs.

Fig. 4 illustrates the working principle of the AART algorithm on a simple 2 × 2 tomographic problem, sampled with two orthogonal projections. The upper left panel defines the tomographic problem. The numbers in this panel indicate the measured projections. The objective is to find the values for each pixel that give rise to the measured projections. As a first step (middle panel on the top) the algorithm begins with a guessed solution, e.g. here assigning each pixel the value 0; in Step 2 the differences e between the guessed and measured projections are calculated for every LOS; in Step 3 e is divided up evenly and distributed among (in practice: added to) all pixels along the LOS and their values are updated; and the same procedure is repeated for the second projection as shown in Steps 4 and 5. These steps constitute one iteration in the algorithm. The iteration stops when a termination criterion is met. For example, the algorithm can be terminated when the relative difference between the measured and predicted projections is smaller than an acceptable error. We want to point out that for the convenience of illustration, a 2 × 2 tomographic problem, which is fully determined, was used here as an example. In practice, TAS measurements will normally lead to an underdetermined problem in combustion diagnostics. A rigorous mathematical expression of the algorithm is encapsulated in the following equation [202]:

$$\vec{x}_{k+1} = \vec{x}_k + \beta \vec{a}_i \frac{p_i - <\vec{a}_i, \vec{x}_k>}{<\vec{a}_i, \vec{a}_i>} \tag{2.7}$$

where $\vec{x}_k$ is the estimated solution at the kth iteration; β a relaxation factor that controls the rate of convergence; $<, >$ denotes the inner product operation; p_i the measured absorbance of the ith beam; and $\vec{a}_k$ the ith row of the weighting matrix $A_{I\times J}$. It is obvious that the computational cost is directly proportional to the number of projections and computational iterations.

The ART algorithm has been widely adopted in cases where a moderately small number (c.a. 100–1000) of LOS measurements is available. A few example applications can be found in [98,196,198,203,204]. The major drawback of this algorithm lies in the fact that it is only semi-convergent [205,206], i.e. ART approaches the true solution at an early stage but diverges away as the iteration steps increase. A detailed description of this problem and ways of mitigation are found in [207].

2.2.3. Landweber algorithm

Having become the most commonly used method in electrical tomography [208], the Landweber algorithm is another iterative method that has been widely adopted in CAT problems [67,114,155,156,169,209,210]. The values of x^- in Eq. (2.7) can be initialized using the equation $\vec{x}_1 = A^T \vec{p}$, which essentially performs the

Table 2
Summary and comparison between algorithms used for TAS.

Algorithm:	FBP	ART	Landweber	MLEM	TRKB
Merits:	Non-iterative and efficient	Most efficient among iterative al-gorithms; handles irregular beam arrangement	Handles irregular beam arrangement	handles irregular beam arrange-ment; fewer artifacts than FBP	Requires minimum number of LOS measurements
Limitations:	Large numbers of pro-jections are required in equi-angular arrangement	Semi-convergence	Semi-convergence	Slow convergence	Needs extensive prior information
# of LOS measurements	> 1000 [179]	100–1000 [155]	20–100 [155]	> 1000 [128]	10–30 [220]
Example references	[174, 179]	[98,196,198]	[114,155,209,210]	[128,178,212]	[220–222]

linear back-projection operation. Here A^T is used to approximate the inverse of A. The subsequent steps of the algorithm can be described by

$$\vec{x}_{k+1} = \Theta[\vec{x}_k + \beta A^T(\vec{p} - A\vec{x}_k)] \tag{2.8}$$

where the subscript k indicates the index of the current iteration; β is again a relaxation factor to controls the rate of convergence; and Θ is an operator that enforces additional constraints, such as the non-negativity of the pixel values. Median filters as well as wavelet filters can also be incorporated in each iteration step in Θ to smooth the reconstruction and remove artifacts, which usually appear as high-frequency components in the reconstruction [177]. As seen from the equation, the errors in the estimated projections $\vec{p} - A\vec{x}_k$ are back-projected through simple matrix multiplications. The Landweber algorithm has been effectively used in applications, where only a very limited number of LOS measurements are available (20–100) and is the most suitable for harsh environments, e.g. during in-cylinder/in-chamber measurements [155]. Similar to the ART algorithm, the Landweber algorithm also suffers from semi-convergence, which, in this approach, can be alleviated e.g. by defining an appropriate termination criterion [211].

2.2.4. Maximum likelihood expectation maximization

The maximum likelihood expectation maximization (MLEM) is another iterative algorithm and has been widely used for tomographic PIV [212–217]. Similar to the ART and the Landweber algorithms, the measured projections are used to update and correct initially guessed values of the pixels. The pixel values are updated one by one during each iteration. The correction for the jth pixel can be written as

$$x^j_{k+1} = x^j_k \sum_i \frac{p_i}{< a_i, x_k >} \frac{A_{ij}}{\sum_i A_{ij}} \tag{2.9}$$

All the beams passing through the specific pixel are used simultaneously to update the value with the absorption lengths used as weighting factors. Compared with the FBP algorithm, the MLEM algorithm does not require equally spaced projection data and can produce fewer artefacts [218]. But the major issue with MLEM is its slow convergence and high computational cost. In [219] the ART and MLEM algorithms were compared for medical imaging applications and shown to exhibit similar reconstruction performance, however the former was estimated to be up to an order of magnitude less costly computationally than the latter for a given task. Thus, the MLEM algorithm seems to be appropriate only in cases which are well-posed and where large numbers (> 1000) of LOS measurements are available, and computational efficiency is not an issue. Examples of MLEM in TAS are presented in [128,212].

2.2.5. Tomographic reconstruction via Karhunen-Loeve basis

For many combustion applications only a limited number of LOS measurements are available and thus the inversion problem becomes underdetermined. The tomographic reconstruction *via* Karhun-Loeve basis (TRKB) algorithm [220–222] is a method that takes advantage of available *a priori* information and thus greatly reduces the dimensionality of the inversion problem. The *a priori* information used in the method is contained in what is called a training set, for example distributions of the target field obtained from computational fluid dynamics simulations or from alternative experimental methods. By performing a so called proper orthogonal decomposition, the eigenfunctions can be extracted and used to approximate the reconstruction as described by

$$\vec{x} = \sum_{i=1}^{Ne} \zeta_i \vec{\Phi}_i \tag{2.10}$$

where $\vec{\Phi}$ and ζ_i are the eigenvectors and corresponding eigenvalues (i.e. the relative weights), respectively; *Ne* denotes the total number of eigenfunctions used in the approximation. The eigenfunctions obtained through POD are optimal since the minimal number of terms is required to reproduce the original training distribution for a given desired accuracy. The first eigenfunction is simply the mean of the training set and the second represents the most prominent fluctuation from this mean. By utilizing both the *a priori* (the training set) and *posterior* (the measured projections) information, the eigenvalues can be obtained by optimizing the following least-square problem

$$\| P^{eigen} \vec{\zeta} - \vec{p}\, m \|_2^2 \tag{2.11}$$

where $\| \ \|_2$ denotes 2-norm, $\vec{p}\, m$ are the measured projections, and P^{eigen} is a matrix with each column containing projections that are calculated treating each eigenfunction as the real distribution. The reconstruction can then be obtained using Eq. (2.10). Typically, only a few eigenfunctions (ca. 10–30), are needed for the tomographic reconstruction; compared with the previous inversion formulation, the number of variables is greatly reduced, making this method especially suitable for scenarios where only a small number of LOS measurements are available.

To summarize, the transform-based and iterative algorithms are the most widely adopted methods for TAS to date. Although they have been used in a number of specific applications, there has been little discussion so far on how and why a specific algorithm was chosen instead of another. In Table 2 we summarize the major algorithms adopted in the context of TAS and point to relevant literature and indicate relative merits and limitations.

2.3. Regularization

The CAT measurements typically result in an ill-conditioned linear equation system. For example, for an overdetermined case in which the ROI is densely sampled and the number of beams is greater than the number of grids, the ill-conditioning is dictated by

the noise from the LOS measurements. This leads to instability during the deconvolution process and small perturbations to the measurement data incur huge errors in the solution. This case is called a discrete ill-posed problem. On the other hand, when the equation system is underdetermined, i.e. the number of beams is smaller than them number of grid points, the ill-conditioning is dominated by the non-unique nature of the solution. This is referred to as a rank-deficient problem. Because the mathematical manifestations of ill-posedness vary, the appropriate strategy must be adopted to alleviate ill-conditioning in a given case. We describe these in the following sections.

2.3.1. Regularization for discrete ill-posed problem

For discrete ill-posed problems, two regularization methods are commonly used: The truncated singular value decomposition method and standard Tikhonov regularization. Both are subjects of this section.

In general, the equations for an overdetermined linear problem can be solved using a least square minimization approach:

$$\vec{x}^{LS} = \arg\min(\| A\vec{x} - \vec{p} \|^2) \tag{2.12}$$

When A is ill-conditioned, the noise present in $\vec{p}$ will be amplified into a large error in the solution $\vec{x}^{LS}$. A singular value decomposition (SVD) can be applied to A to analyze how noise is amplified during the inversion process as follows

$$A = USV^T \tag{2.13}$$

where $U \in R^{I\times I}$ and $V \in R^{J\times J}$ are orthonormal matrices and $S \in R^{I\times J}$ contains singular values along its diagonal in a descending order. The least square solution can now be expressed as

$$\vec{x}\,LS = \sum_{j=1}^{J} \frac{\vec{v}_j}{\sigma_j} \vec{u}_j^{\mathrm{T}} \vec{p} \tag{2.14}$$

where the $\vec{u}_j$ and $\vec{v}_j$ are the jth column vectors of U and V respectively and $\vec{p}$ is the jth singular value. When $\vec{p}$ is contaminated with noise then the above equation can be reformulated as

$$\vec{x}\,LS = \vec{x}^{exact} + \vec{x}^{error} = \sum_{j=1}^{J} \frac{\vec{v}_j}{\sigma_j} \vec{u}_j^{\mathrm{T}} \vec{p}^{exact} + \sum_{j=1}^{J} \frac{\vec{v}_j}{\sigma_j} \vec{u}_j^{\mathrm{T}} \Delta\vec{p} \tag{2.15}$$

where $\vec{x}^{exact}$ and $\vec{x}^{error}$ are the exact solution and the reconstruction error respectively, and $\Delta\vec{p}$ represents the measurement noise. As can be seen from the right-most term, the reconstruction error is inversely proportional to singular values and will be greatly dominated by the smallest ones. The solution can be improved by removing a certain number of terms with the smallest singular values in Eq. (2.15). This method is called truncated SVD regularization.

Alternatively, standard Tikhonov regularization can be used to mitigate the negative impact from measurement noise. Here the problem can be formulated as:

$$\vec{x}_{Tik} = \arg\min(\| A\vec{x} - \vec{p} \|^2 + g^2 \| \vec{x} \|^2) \tag{2.16}$$

where g is a parameter that weights the regularization. Eq. (2.16) can be solved and organized as

$$\vec{x}^{LS} = \sum_{j=1}^{J} c_i \frac{\vec{v}_j}{\sigma_j} \vec{u}_j^{\mathrm{T}} \vec{p} \tag{2.17}$$

where c_i are weighting factors, defined as

$$c_i = \frac{\sigma_j^2}{\sigma_j^2 + g^2} \tag{2.18}$$

As can be seen, g is used to regulate the relative weights between the SVD components, resulting in a weakened influence of the components with the smallest singular values.

To summarize, the ill-posedness of an overdetermined CAT problem can be alleviated by either removing (via truncated SVD regularization) or reducing the weights (via standard Tikhonov regularization) of the detrimental SVD components. For a more in depth review of these methods, the reader is referred to [127].

2.3.2. Regularization for rank-deficient problems

In contrast to the discrete ill-posed problems, in which the reconstruction error is dominated by noise contamination, the rank-deficient (underdetermined) problems suffer from insufficient posterior information, i.e. an insufficient number of LOS measurements. To compensate for this, additional *a priori* information should be included in the analysis [116]. In CAT, the mostly widely used prior information is the non-negativity constraint and a smoothness condition for the target flow field. In this case one can perform a so called constrained first order Tikhonov regularization, which accommodates this information as follows

$$\vec{x}_{Tik} = \arg\min\left(\| A\vec{x} - \vec{p} \|^2 + g^2 \| L\vec{x} \|^2\right) \textit{ subject to } \vec{x} \geq 0 \tag{2.19}$$

where L is a Laplacian matrix that is used to enforce the smoothness condition. It is defined as

$$L_{i,j} = \begin{cases} 1 & i = j \\ -1/n_i & i \text{ neibors } j \\ 0 & \text{otherwise} \end{cases} \tag{2.20}$$

where n_i is the number of neighboring pixels for the ith pixel.

We note that constrained first order Tikhonov regularization can also be applied to discrete ill-posed problems discussed in the previous section; in this case, the regularization not only damps the instability caused by small singular values, but also enforces *a priori* information such as non-negativity and spatial smoothness. For this to be effective, g needs to be carefully chosen so that neither the *a priori* (smoothness) nor *a posterior* (measurements) information dominates over one another. So far, two methods have been reported for successful estimation of g in absorption tomography, the so-called L-curve method or a method based on SVD. The former approach will be illustrated in detail in Section 3.2.2. The SVD method suggests that the first I values (corresponding to the number of beams) of singular values of the augmented matrix $[A;\ \lambda L]$ should not be larger than the singular values of $[A]$ alone. In contrast the remaining $(J\text{-}I)$ singular values of $[A;\ \lambda L]$ should be as large as possible. In this case, the regularization does not significantly affect measurement fidelity while at the same time providing additional SVD components (from the smoothness condition), which provide maximal noise immunity. Other interesting techniques might be feasible for a determination of g, such as the unbiased predictive risk estimator method or the generalized cross validation method, however their merits in CAT have yet to be demonstrated. For more details the interested reader is referred to [209].

2.3.3. Regularization via Bayesian formulation

As mentioned, the negative effects of ill-posedness can be mitigated through incorporation of prior information, as was shown for the constrained Tikhonov regularization in the previous section. An alternative approach has recently been demonstrated for CAT and shown promise. It is based on a Bayesian formulation of the problem, which provides a versatile tool to integrate a variety of prior information in the inversion process. This can then be solved *via* maximum a posterior (MAP) estimation. Here, we provide one example to show how the spatial smoothness and non-negativity priors can be utilized in combination with the measured information in a

Bayesian formulation of the problem that enables improved reconstruction. According to the Bayes' theorem, the CAT inversion can be modeled as a MAP estimation problem as

$$prob(x|p) = \frac{prob(p|x)prob_{NN}(x)prob_S(x)}{prob(p)} \tag{2.21}$$

where $prob(x|p)$ is the probability that a specified flow distribution x is the right one when the measurement data p is observed; $prob(p|x)$ is the probability that the measurement data p occur for a given distribution x; $prob_{NN}(x)$ and $prob_S(x)$ are the probabilities that the specified x satisfies the smoothness and non-negativity priors, respectively; and $prob(x)$ is the marginal probability of the measurement data p.

The values of $prob(p|x)$ are always smaller than unity in the presence of measurement noise and their distribution can be predicted by Eq. (2.22), below, if the noise spectrum is assumed to be normally distributed.

$$prob(p|x) = \frac{1}{\sqrt{2\pi\sigma_m^2}} \prod_{i=1}^{I} \exp\left[-\frac{(p_i - A_i x)^2}{2\sigma_m^2}\right] = \frac{1}{\sqrt{2\pi\sigma_m^2}} \exp\left[-\frac{\| \vec{p} - A\vec{x} \|_2^2}{2\sigma_m^2}\right] \tag{2.22}$$

Here σ_m is the standard deviation of the measurement noise.

The non-negativity condition can now be implemented as

$$prob_{NN}(x) = \prod_{j}^{J} H(x_j) \tag{2.23}$$

where H is a step function that equals zero for $x_j < 0$ and is unity otherwise.

The smoothness condition can on the other hand be defined as

$$prob_S(x) = \exp[-\vartheta \| Lx \|_2^2] \tag{2.24}$$

where ϑ is a scalable factor.

Combining the above equations and setting $g^2 = 2\vartheta\sigma_m^2$, one obtains a likelihood objective function from Eq. (2.21) that can be written as:

$$prob(p|x) = \frac{1}{\sqrt{2\pi\sigma_m^2}} \exp[-\| \vec{p} - A\vec{x} \|_2^2 - g^2 \cdot \| Lx \|_2^2]^{\frac{1}{\sigma_m^2}} * \prod_{j}^{J} H(x_j) \tag{2.25}$$

One can see that Eq. (2.25) can be maximized by minimizing $\| \vec{p} - A\vec{x} \|_2^2 + g^2 \| L\vec{x} \|_2^2$ subject to $x \geq 0$; this turns out to be exactly analogous to a first order Tikhonov regularization with a non-negative constraint.

It has to be noted that by customizing Eq. (2.21), more prior information in addition to smoothness and non-negativity can be easily accommodated. Bayesian formulation can further include temporal information as prior. An example has been demonstrated where data from computational fluid dynamics simulations have been combined with CAT measurements data to improve the reconstruction and the method works well even in low SNR measurement situations [127].

To summarize, the regularization strategy should be chosen according to both the nature of the ill-posedness and how much prior information is available. For discrete ill-posed problems which suffer majorly from the measurement noise, a truncated SVD or standard Tikhonov regularization can be applied to reduce the impairing effects of SVD components with small singular values. For rank-deficient problems, additional prior information such smoothness and non-negativity can be included *via* constrained first order Tikhonov regularization. If more prior information is available, a Bayesian formulation is a powerful and versatile tool to combine the *a priori* and *posterior* information effectively. Since regularization is a universal topic for all variants of tomography, it has been studied extensively and the authors are referred to [127,223–225] for a more comprehensive and detailed discussion.

2.4. Experimental considerations

The objective of a CAT experiment is to collect transmission/projection data as the input for the inversion algorithms. A typical setup consists of light sources to generate the probing beams, a detector to capture the transmitted light intensity, and a data acquisition system. A means to displace the probing beams spatially in a

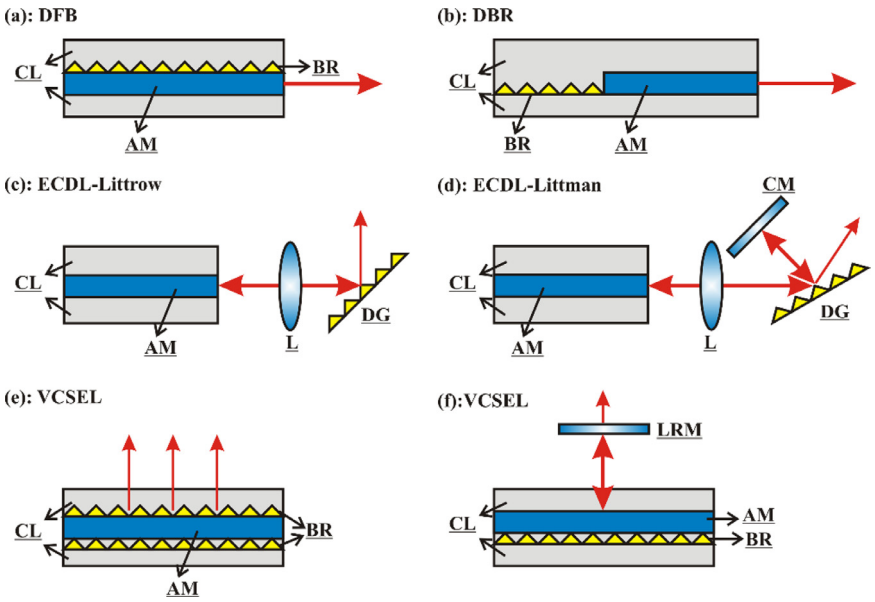

Fig. 5. Cavity structures of different tunable semiconductor lasers. DFB: distributed feedback; DBR: distributed bragg reflector; AM: active medium; BR: bragg reflector; L: lens; DG: diffraction grating; CM: cavity mirror; and LRM: low-reflectivity mirror. Some figure panels were adapted from examples given in [241].

Table 3
Summary of lasers and detectors traditionally used in CAT.

Flow species	Wavelength range	Light sources	Detectors
H_2O	NIR	TDLs [98,163,178–180,193,195,197,229,232]	Ge, InGaAs
NH_3	NIR	DFB-TDLs [196]	InAs
CO_2	NIR, MIR	TDLs [235,250], KCL:Li CCL [171,228], glow bar [251]	InSb, InAs
CO	MIR	DFG [175], TDLs[164]	InSb, HgCdTe
CH_4	NIR, MIR	TDLs [162], HeNe [170,198,221,227]	InAs, PbSe, pyroelectricty detector
Ar	NIR	TDLs [184,185]	Uncooled photodetectors
Hydrocarbon	NIR, MIR	TDLs [114], HeNe [226]	InGaAs, HgCdTe
CO, CO_2, CH_3COOH, and CH_3COCH_3	MIR	FTIR [187]	
O_2	VIS	TDLs [216]	Si
Soot	VIS	Lamp [252]	Photomultiplier tubes
I_2	VIS	Argon-ion laser [188]	Si

reproducible fashion is critical since this determines the spatial sampling efficiency and thus the reconstruction quality. In addition, as an imaging technique, the quantification of spatial resolution is also a crucial topic as it defines the applicability of TAS. The following sub-sections will reflect on these considerations.

2.4.1. Light sources and detectors

Various light sources have been used, or proposed, for tomographic CAT measurements including HeNe lasers [170,198,221,226,227], KCl-Li color-center lasers [171,222,228], semiconductor lasers (both tunable and single-mode) [112,114,155,162–165,174,178–180,184,185,193–197,199,200,216,229–236], ND:YAG lasers, dye lasers [237], Ar-ion lasers [188], light-emitting diodes [183], tunable fiber-ring lasers [119,238], Fourier Domain Mode-Locking (FDML) lasers [239,240], supercontinuum radiation sources [117], and frequency-combs [161].

The most widely adopted technology consists of tunable semiconductor lasers (TSLs), which offer advantages of low cost, narrow emission line-width, rapid wavelength-tunability, and operation at room-temperature. Furthermore, a broad wavelength range is available, e.g. 400–3000 nm for tunable diode lasers (TDLs), 3 to 6 μm for interband cascade lasers (ICLs), and 6 to 14 μm for quantum cascade lasers (QCLs) [242,243]. Note that lead-salt lasers used in early applications [235] can today be replaced with QCLs [235]. Depending on how the laser radiation is emitted, TSLs can be categorized into surface-emitting and edge-emitting lasers, respectively. The selection of longitudinal laser modes in TSLs can be realized either within the cavity itself or externally and a few popular geometries are shown in Fig. 5 above. The structures of TSLs include distributed feedback (DFB), distributed Bragg reflector (DBR), external-cavity Littrow (EC-Littrow), external-cavity Littman (EC-Littman), and vertical cavity surface-emitting as illustrated in Fig. 5 [241,242,244–247]. Panel (a) shows the structure of a DFB laser, where a Bragg reflector is positioned above the gain medium. The Bragg reflector is made of hundreds of dielectric layer pairs, each containing two layers with slightly different refractive indices and acting as a reflective filter with a narrow bandwidth (tens of MHz). Typically, one facet of the DFB laser is high-reflection (HR) coated so that most of the light can be channeled out through the other end which is anti-reflection (AR) coated. Wavelength tuning can be realized by either modulation of the driving current (fine tuning) or chip temperature (coarse tuning), which induces thermal expansion and mechanical strain, causing variations in the periodicity of the Bragg reflector [248]. Panel (b) shows the structure of a DBR laser in which the Bragg reflector is positioned adjacent to one AR coated facet and the other facet is low-reflection (LR) coated. For DFB/DBR lasers, the wavelength-selection element is integrated in the semiconductor chip. However, wavelength selection can also be implemented outside of the chip. For example Panel (c) shows the external cavity Littrow (EC-Littrow) configuration in which one facet is HR-coated and the other one AR-coated [246]. The emitted light is collimated with a lens and shone on a diffraction grating, which feeds the first order diffracted beam back into the chip. Both the output wavelength and the propagation direction can be adjusted by rotating the grating. The uncertainty in beam orientation limits its applications for CAT. Panel (d) shows the EC-Littman structure in which the grating is fixed and an additional reflective mirror is introduced. This configuration guarantees a fixed output direction and a narrower line-width at the cost of reduced power since the loss incurring, and wavelength-dependent, diffraction occurs twice. Panel (e) shows the vertical cavity surface-emitting structure of a laser diode which includes two Bragg gratings both on top and bottom of the gain medium. Compared with DFB/DBR lasers, VCSELs can achieve a broader spectral tuning range and a higher modulation bandwidth, which makes them more suitable for high pressure applications [246]. It has to be noted that CAT has been evolving for decades and some of the lasers that had been used in the past are now obsolete and have been replaced with a new generation of laser sources. Great potential exists for supercontinuum sources, which will be discussed in the nonlinear tomography chapter at a later stage in this review.

For the previous implementations, semiconductor photodetectors as well as photomultiplier tubes were used for signal registration. Table 3 summarizes the lasers and detectors that have been used. A more detailed summary of the detector technologies can be found in [233,236,238,249].

2.4.2. Beam arrangement and optimization

As illustrated in Fig. 6, there are three types of beam arrangement for CAT, which are fan-beam [253], parallel-beam [175], and irregular-beam [114,169,232] arrangements respectively. In fanned beam implementations, a diverging beam arrangement is used to produce various projections directions as shown in Fig. 6(b). Mathematically, the fan-beam setting (Panel (b)) is equivalent to the parallel-beam version (Panel (a)). However, in an experimental sense, the optics is simpler to set up for the former. On the other hand, the energy density of the fanned beams is lower than the line illumination that is usually used in a parallel-beam arrangement, resulting in a smaller SNR. Irregular-beam arrangements (Panel (c) and (d)) have also been used in practical scenarios, in cases where optical access is extremely limited, such as internal combustion engines [114,155,169,177].

The motivation for optimizing the beam arrangements is four fold [169,255–257]: 1) limited optical access in most practical applications; 2) beam obstructions, e.g. the beams cannot pass the central axial of the drive shaft of an internal combustion engine; 3) cost caused by requirement for multiple lasers and detection systems; and 4) better beam arrangements to reduce perturbations from measurement noise. The beam arrangement can be optimized using the concept of the resolution matrix [255], which will be derived here. As mentioned earlier, the tomographic problem results in a linear equation system described by Eq. (2.6), which is usually rank-deficient and underdetermined due to the limited number of projections. In order to make the equation system complete, *a priori* information such as the smoothness of the distribution of the absorption coefficients should be included and the optimal solution

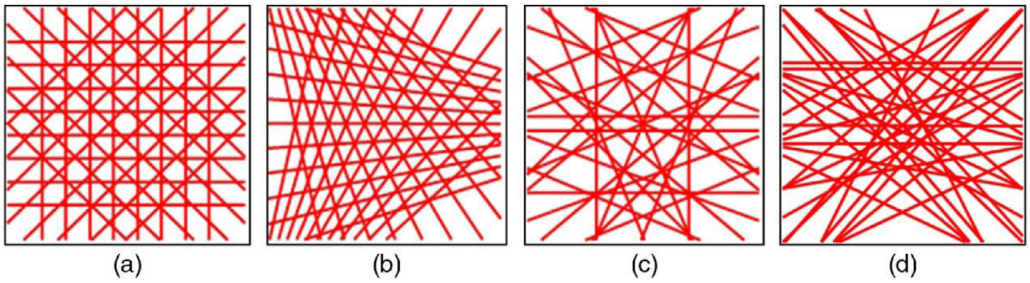

Fig. 6. Illustration of beam arrangements: (a) orthogonal with 32 beams [155], (b) fan arrangement with 33 beams [254], (c) irregular with 27 beams [169], and (d) irregular with 32 beams [169]. The figures were adapted from [255].

can be obtained from a least squares minimization as

$$\vec{x}_{LS} = \arg\min \| A\vec{x} - \vec{p} \|_2^2 + g \| L\vec{x} \|_2^2 \tag{2.26}$$

where L is a matrix operator that performs the regularization and g is the regularization factor that controls the strength of the *a priori* information. By taking the derivative of the RHS, the corresponding Euler equation can be obtained as

$$(A^T A + gL^T L)\vec{x}_{LS} = A^T \vec{p} \tag{2.27}$$

The Euler equation can be directly solved and reorganized as

$$\begin{aligned} \vec{x}_{LS} &= (A^T A + gL^T L)^{-1} A^T \vec{p} \\ &= A\, p^{--} = A\vec{p}\ exact + A\kappa \\ &= \vec{x}_{exact} + (AA - I)\vec{x}_{exact} + A\kappa \\ &= \vec{x}_{exact} + (R - I)\vec{x}_{exact} + A\kappa \end{aligned} \tag{2.28}$$

where R is the so-called resolution matrix and I the identity matrix. The reconstruction error contains two parts, which are the regularization error $(R-I)\vec{x}^{exact}$ and the perturbation error $A\kappa$, respectively. For applications with limited optically access, the equation system would not be complete and the regularization is used as a filter that selects a solution that satisfies the measurements and at the same time matches the *a priori* information best. It has been shown that for limited-data tomography, the perturbation error is negligible over a wide range of g and the regularization error dominates [113]. In this case, the optimal beam arrangement can be achieved when the regularization error is minimized. The error can be quantified as the Frobenius norm [255] of $(R\text{-}I)$, defined as

$$F(\vec{\Psi}) = \| R(\vec{\Psi}) - I \|_F^2 \tag{2.29}$$

where I is the identity matrix, $\vec{\Psi}$ is a vector of complex numbers, each of which contains the position t (real part) and orientation θ (imaginary part) of a specific beam. The beam arrangement optimization can now be converted into a minimization problem, which can be solved with a global minimizer such as the genetic algorithm [256]. However, F is a good predictor for the reconstruction error only when the number of beams are the same for all arrangements. Otherwise, F has to be normalized by the number of beams so that arrangements with different numbers of beams can be compared in terms of efficiency.

2.4.3. Quantification of spatial resolution

As an imaging technique, the spatial resolution (SR) of CAT is a critical parameter for practical applications. However, there are only a few studies available so far on this topic, for the following reasons: 1), the tomographic images are synthetic (i.e. reconstructed) and the quantification of SR is not as straight-forward as is the case for planar imaging techniques; 2), there is a plethora of ways to define SR (see [258]); 3), an experimental determination of SR is non-trivial for CAT, because valid experimental phantoms are difficult to construct for gaseous flows; 4), the SR for practical turbulent flames cannot easily be inferred by applying the same tomographic system to validation phantoms, because the SR does not only depend on the spatial sampling (i.e. the beam arrangement) used, but also on the SNRs of the individual LOS measurements. These may be dramatically different for different measurement objects; 5), even *within* a flow field, the SR may thus differ from position to positon, as they are sampled with different beams and thus likely to result in various SNRs; and finally 6), since noise levels of the LOS measurements evolve over time, the SR changes even for the same position within the imaging plane. There is still a lot of work to be done to provide a framework for a quantitative comparison of SR between different measurement scenarios in CAT. We provide an introduction to the topic in this section, so that the reader can appreciate the challenges and current thinking on this topic. We follow the approach taken in [258], where SR was defined as a measure of the ability to resolve non-overlapping features within the imaging space. In the article, the authors quantified the SR through the calculation of a modulation transfer function (MTF). The latter can theoretically be obtained either from measurements of a point spread function (PSF), a line spread function (LSF), or an edge spread function (ESF). However, it is almost impossible in practice to fabricate point or line phantoms with gaseous flows, and the authors demonstrate that the generation of an ESF via two parallel flows is much more convenient to achieve [258]. From the ESF, one can calculate the LSF, and PSF as follows:

$$\frac{d}{dx} ESF(\sigma, \rho) = LSF(\sigma, \rho) \overset{\rho = \rho_0}{\rightarrow} LSF(\sigma, \rho_0) = PSF(\sigma, \rho_0) \tag{2.30}$$

where ρ and σ are the axis parallel and perpendicular to the edge respectively; and ρ_0 defines a specific location along the edge. The assumption here is that the PSF is rotationally symmetric, in which case the LSF is a good approximation for it. The MTF can then be calculated as a measure of SR as follows:

$$DFT[PSF(\sigma, \rho_0)] = MTF(f_s) \tag{2.31}$$

where *DFT* means discrete Fourier transform and f_s stands for the spatial frequency along the σ axis. The MTF thus obtained provides the experimentalist with a useful measure to adjust experimental parameters, such as spatial sampling, beam size, to maximize SR and also to assess reconstruction artefacts that come from measurement noise and discretization errors.

2.5. Applications

2.5.1. Overview

CAT has found numerous applications in practical flow diagnostics. The applications are summarized into the following three categories:

i) Laboratory flames

Wondraczek et al. demonstrated their system using a DFG-based laser source on a flat-flame burner [175]; Villarreal and Varghese demonstrated their system on an axis-symmetric flat-flame burner [235]; Wang at al. demonstrated their system on NH_3 flows [196] and also a premixed methane/air [98] flame; Liu et al. demonstrated their fan-beam system on an axis-symmetric flat flame [254,259]; McNesby et al. performed tomographic analysis to provide a correction to low-pressure stoichiometric premixed CH_4/O_2 flame

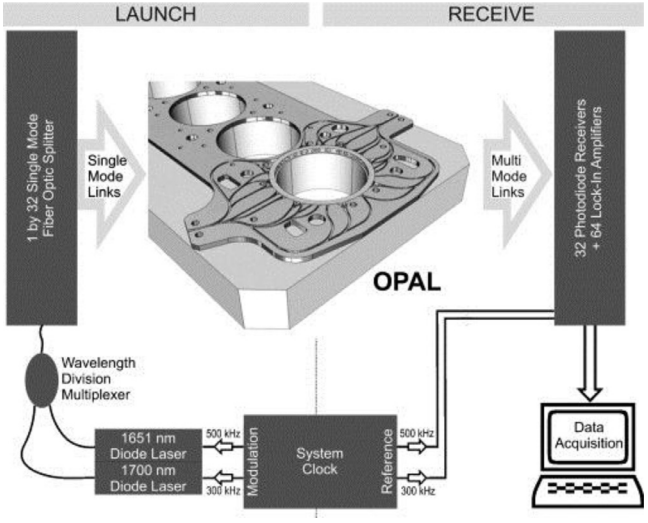

Fig. 7. Schematic overview of a tomographic system for engine measurements. Figure adapted from [114], with the permission from Elsevier.

temperature measured with LOS two-line thermometry [164]; Hall et al. used CAT to image the temperature of sooting flames [252]; Ouyang et al. demonstrated their system on an axis-symmetric porous ceramic burner to measure the CO_2 concentration [165]; Silver et al. used CAT to measure spatial distribution of H_2O in laminar non-premixed μg flames [163]; Dahm et al. used CAT to map local mixture fraction in a microgravity vortex ring diffusion flame [162] to study how differential diffusion affects flame-votex interactions; Baum et al. used CAT to obtain the field of mixture fraction of a plume to evaluate predictive fire models [187]; Gouldin et al., demonstrated their technique on a flat burner [228], a non-reacting laminar flow [170], a steady non-reacting flow of methane and argon [221], and forced jet flows to study dynamics and structures of these jets [171]; Santoro et al. applied their system to an off-axis turbulent methane-air free jet to determine the mean methane concentration throughout the mixing region [227]; and Shimizu and Sakai demonstrated a tomographic system on a pulsed jet flame for temperature and sodium number density imaging [260].

ii) Practical combustors

Kawazoe et al. applied their system to an internal combustion gasoline engine to investigate the hydrocarbon fuel distribution [186]; McCann's group has developed tomographic systems for the measurement of hydrocarbon fuels within automotive engines [114,155,156,199,231,236,238,249]; Dahm et al. tested their sensor on a model gas turbine combustor for potential monitoring of premixing degree of fuel and air [198]; Bryner et al. demonstrated a proof-of-concept system for simultaneous imaging of both temperature and species concentration on a flat burner [180]; the system was later applied to the exhaust plane of the University of Virginia's Supersonic Combustion Facility (UVaSCF) as well as at the NASA Langley Direct-Connect Supersonic Combustion Test Facility (DCSCTF) [178,179] to calculate the combustion efficiency; Deguchi et al. developed a CAT system for measurements of 2D temperature distributions in diesel engine exhausts [229]; and Lindstrom et al. used CAT to study the shock train structure in the isolator section of the supersonic combustion facility at Wright-Patterson AFB [232].

iii) Other applications

Belotti et al. used CAT to reconstruct distributions of CO_2 over a volcanic site [250]; Bennett et al. were the first to demonstrate the fan-beam tomography for tomography of gas dynamics and measured the distribution of an iodine-vapor plume to experimentally confirm a predictive noise theory [188]; Zhang et al. used their system to study development of arcjet plumes as well as how the mass flow rates and discharge current affect maximum temperature and argon number density [184]. Kasyutich et al. used CAT to recover water vapor concentration to better understand the chemical mechanisms of the chemical vapour deposition process, aiding in the design of new coating heads and providing a possible tool for process control leading to optimized film properties [195]; Salem et al. used their tomographic sensor to map the H_2O concentration to investigate the breakthrough of a packed bed adsorber [197]; and Kauranen et al. demonstrated their high-sensitivity system for the measurement of weak-absorbing O_2 gas flows [216].

2.5.2. Principle of two-line imaging thermometry

The principle of CAT for simultaneous imaging of temperature and species concentration is summarized here. By performing the tomographic reconstructions at two pre-selected transitions (ν_1 and ν_2) with different temperature dependencies, two maps of integrated absorbance can be obtained. According to Beer's law, the integrated absorbance at frequency of ν in the jth pixel is defined as

$$\int \alpha_\nu \cdot L \cdot d\nu = \int P \cdot \Phi(\nu) \cdot S(T) \cdot X \cdot L \cdot d\nu = P \cdot S(T) \cdot X \cdot L \tag{2.32}$$

where α_ν [cm^{-1}] is the absorption coefficient at a frequency of ν, P [atm] the pressure, Φ *is the lineshape*, S [cm^{-2}·atm^{-1}] the line strength of temperature T, T [K] the real temperature, X the species concentration, and L [cm] the absorption path length. As can be seen, the integrated absorbance is a nonlinear function of T, but a linear function of both X, and P. The ratio between the integrated absorbance at ν_1 and ν_2 for the jth pixel can be

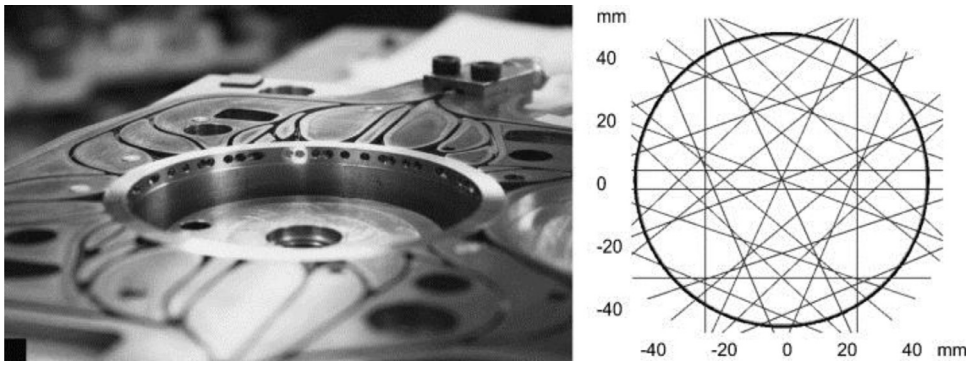

Fig. 8. (a) The OPAL during manufacture: fiber protection channels, coolant galleries and a fiber entry/exit port (upper right) are all clearly visible. (b) The 27 beam arrangement implemented by the OPAL shown in (a). Adapted from [114], with the permission from Elsevier.

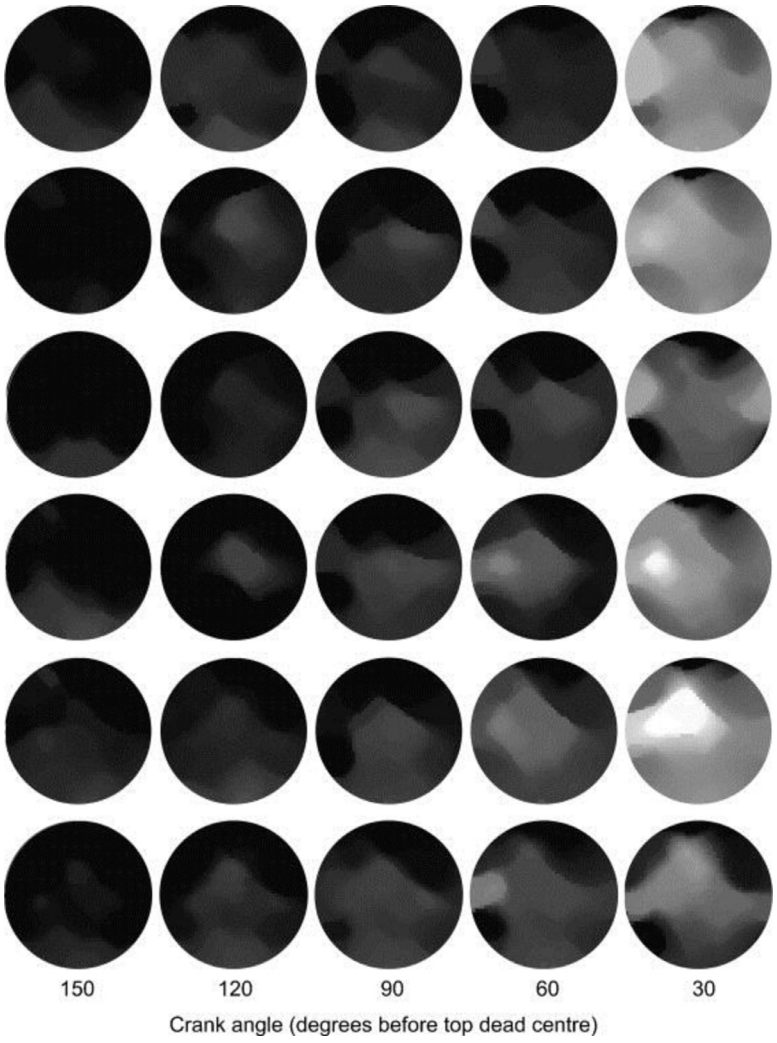

Fig. 9. Exemplar reconstructions of hydrocarbon distributions during 6 consecutive engine cycles using 15 qualified beams. Each row represents the reconstructions for a specific engine cycle, and each column represents reconstructions correspond to a specific crank angle during the 6 consecutive engine cycles. Figure reproduced from [114], with the permission from Elsevier.

calculated as

$$R_j = \frac{\int \alpha_{v_1 j} \cdot L \cdot dv}{\int \alpha_{v_2 j} \cdot L \cdot dv} = \frac{S_1(T_j)}{S_2(T_j)} = \frac{S_1(T_0)}{S_2(T_0)} \exp\left[-\frac{hc(E_1'' - E_2'')}{k}\left(\frac{1}{T_j} - \frac{1}{T_0}\right)\right] \tag{2.33}$$

where T_0 [K] is the reference temperature, T_j [K] the real temperature of the jth pixel, h [J·s] Planck's constant, c [cm·s^{-1}] the speed of light, k [J·K^{-1}] Boltzmann's constant, and E'' [cm^{-1}] the lower state energy. Therefore, the temperature T_j can be obtained from

$$T_j = \frac{\frac{hc}{k}(E_2'' - E_1'')}{\ln R_j + \ln\frac{S_2(T_0)}{S_1(T_0)} + \frac{hc}{k}\frac{(E_2'' - E_1'')}{T_0}} \tag{2.34}$$

Assuming an atmospheric pressure, the molar fraction X_j can then be calculated as

$$X_j = \frac{a_{v_1 j}}{S_1(T_j)} \tag{2.35}$$

2.5.3. Exemplar engine measurements

As mentioned earlier, CAT is highly complementary to planar imaging techniques and is more suitable for applications where optical access is severely limited such as engine measurements. Fig. 7 shows an exemplar CAT imaging system [114], which was designed for the imaging of hydrocarbon distributions in a 4-cylinder automotive gasoline engine (Ford Duratec New I4). The system was tested extensively in laboratory phantom experiments [169] prior to the engine tests. The key components of the system include an OPtical Access Layer (OPAL), as shown in Fig. 8(a) and an optoelectronic system. The OPAL defines the optimized layout of 27 measurement beams and is illustrated in Fig. 8(b). Two fiber-coupled diode lasers, with a wavelength of 1700 and 1651 nm respectively, were used to probe the reactive flow within one cylinder of the engine. The 1700 nm laser was used to measure the hydrocarbon absorbance, and the 1651 nm laser was used to probe a non-absorbing wavelength for intensity referencing. The intensity of both lasers was modulated at a frequency of 500 kHz and 300 kHz, respectively using a direct digital synthesis module. An integrated wavelength multiplexing fiber coupler and 1×32 splitter connects the sources to the launch channels of the OPAL using single-mode fibers. On the detection side, multi-mode fibers transfer collected radiation to InGaAs photodiodes. The transmitted signals were recovered using lock-in amplifiers for demodulation of both wavelengths before transfer to a PC for post-processing. A relatively homogenous fuel vapor distribution was generated within the cylinder for a validation experiment. The pressure inside the cylinder was monitored with a transducer; and the absorbance was assumed to be independent of temperature (the temperature variation was calibrated up to 150 °C i.e. the limit of the laboratory setup, and was found to be approximately constant [155]). Before reconstruction, the quality of the measurements was

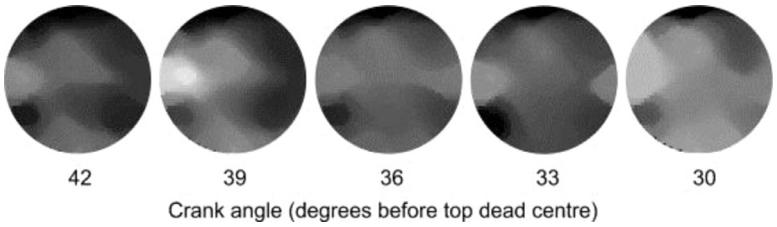

Fig. 10. Five images showing rapid changes in the period from 42° to 30° before TDC at intervals of 3° CA obtained using the same engine conditions and probing beams as Fig. 2.9. The figure reproduced from [114], with the permission from Elsevier.

examined and data with an SNR below a certain threshold were removed. The remaining data were then used for reconstruction.

Fig. 9 shows the reconstructions for six sequential engine cycles using 15 qualified beams. The data sets were collected with the engine running at 1500 rpm and 1.5 bar BMEP (brake mean effective pressure) load, conditions under which the fuel distribution was expected to be homogeneous. Each row represents one of the six fired cycles, over the period between 150° crank angle (CA) and 30° CA before top dead center (TDC) with intervals of 30° CA. The reconstructions were quite homogenous and the absorption increased as the fuel was compressed, as expected. Fig. 10 shows the reconstruction for one engine cycle in the period from 42° to 30° before TDC sampled at 3° CA intervals. They were obtained under the same engine conditions and using the same probing beams as Fig. 9. The distribution of hydrocarbons varies significantly between neighboring crank angles and was successfully captured by the imaging system. The measurements were validated qualitatively by comparing the reconstruction to an estimated homogeneous distribution assumed for the phantom. The same opto-electronic system, with 31 beams arranged in four parallel-beam projections, was successfully used to image fuel distributions in single-cylinder optical research engines, with direct fuel injection, running in both the spark ignition mode [156] and the compression ignition mode [261].

For this application with limited optical access, absorption tomography is uniquely qualified as an imaging technique that can be applied without requirement for significant modification of the mechanical and thermal properties of the engine. Nevertheless, the implemented CAT system suffers from several disadvantages. For example, referencing is mandatory to monitor the measured laser intensity in absence of absorption, and the method is adversely affected by mechanical deformations of the engine, for example due to pressure changes. Furthermore, some probing beams may become unusable due to lens contamination, making the data collection inefficient. The aforementioned limitations can be alleviated/overcome by introducing a new imaging concept, which we have called nonlinear absorption tomography, and its combination with recent developments in frequency-agile absorption spectroscopy and 1*f*-nomalized CFWMS. These will be introduced and discussed in the next chapter.

3. Absorption-based nonlinear tomography

As can be seen from the previous chapter, CAT processes the projections measured at a single transition of the target species in the tomographic reconstruction [196,198]. Theoretically, to make the equation system full-rank, intensive spatial sampling is necessary to obtain a sufficient number of equations. This increases experimental complexity to provide access for projection deliveries. However, in practice, applications such as engine measurements, have only limited optical access and only a few projections will be available; the ill-posed nature of the resulting inversion problem worsens. To alleviate this problem, many algorithms that work well for limited-data tomography have been adopted from X-ray tomography and adapted to CAT for combustion diagnostics. As mentioned earlier, in practical implementations, an irregular beam arrangement was also adopted to maximize the spatial sampling efficiency, which increases the complexity of the experimental setup. In addition, classical tomography is limited in nature since it can only be applied when the physical quantity to be reconstructed is integratable (accumulative) along the LOS. Such requirements greatly limit the compatibility of CAT with more advanced absorption techniques. In addition, for luminous reactive flows, the tunable diode laser is the mainstream laser source but this features only a limited spectral range in the near-infrared, making the simultaneous measurement of multiple species difficult.

Facilitated by recent advances in broadband, narrow linewidth, high repetition rate wavelength-swept laser sources, the simultaneous sampling of numerous absorption features from multiple flame species has now become possible [24,25,262–267]. On the other hand, the recent developments in tunable semiconductor lasers [243,246,268–270] and in frequency-multiplexed CFWMS [271–276] also enable the simultaneous detection of multiple orders of harmonic signals. Encouraged by this progress, a new breed of tomographic techniques, which sample not only the spatial but also the spectral and/or harmonic domains were recently proposed. As opposed to CAT, in which the target field is linearly related to the LOS measurements, the target fields in the new variant have nonlinear dependencies on the LOS measurements. In this case, the inversion problem can be numerically modelled as the solution to a set of nonlinear equations

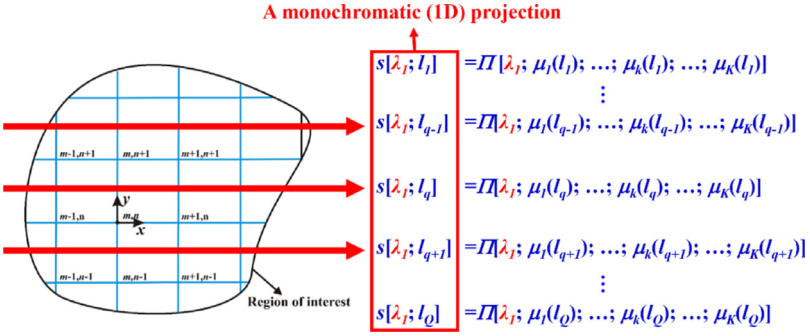

Fig. 11. Definition of a 1D projection in nonlinear tomography.

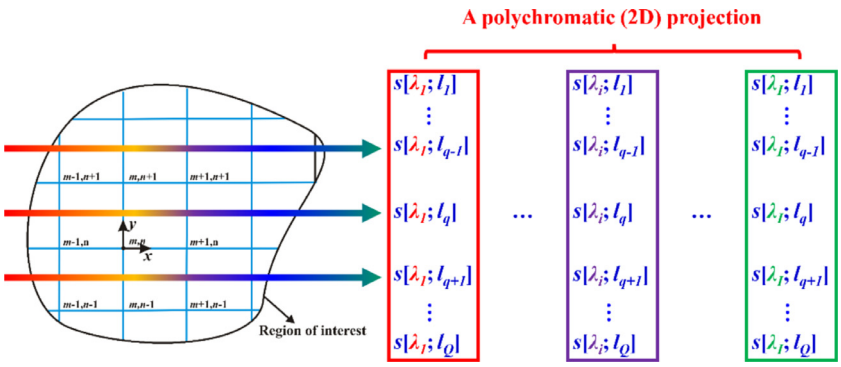

Fig. 12. Definition of a 2D projection in nonlinear tomography.

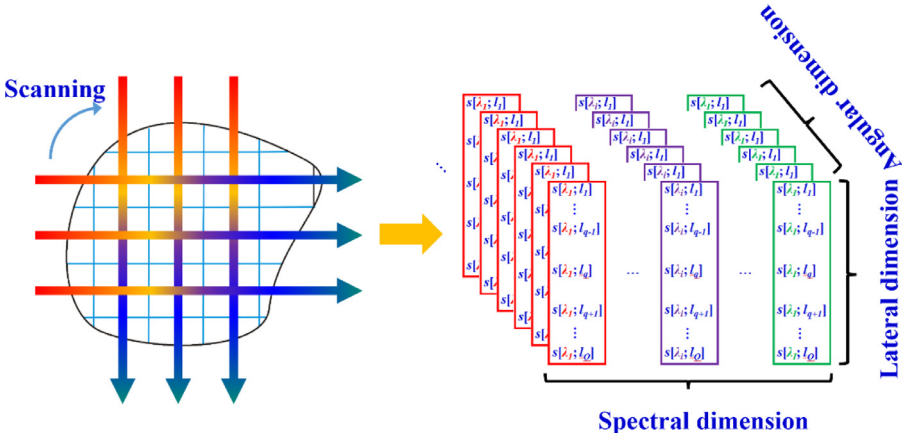

Fig. 13. Definition of a 3D sinogram in nonlinear tomography.

whose variables are the profiles of temperature and species concentration. This circumvents the step of retrieving the distribution of absorption coefficients as required in CAT [117,118]. The result is a new imaging concept, which we call nonlinear tomography, which brings additional capacities. For example, it was numerically demonstrated that pressure imaging is possible with this concept [117], pushing the application limit of absorption tomography to scenarios where pressure non-uniformities cannot be ignored e.g. the flow field in a scramjet where shock waves prevail [277]. The aim of this chapter is to summarize the definition, mathematical formulation, simulative studies, and experimental demonstrations of absorption-based nonlinear tomography, ABNT.

3.1. Mathematical formulation of ABNT

In the previous chapter, it was seen that for linear tomography 1) the field has to be integratable along the LOS, and 2) the integration has to be physically meaningful. Such requirements prevent the implementation of CFWMS with CAT in scenarios where the optical depth is thick [116], since in this case the harmonic signals cannot be linearized and are not integrals of any physical quantity. Similar limitation exists for combination of other advanced spectroscopic techniques with CAT.

To overcome such limitations, the concept of absorption-based nonlinear tomography was recently proposed [117]. As opposed to CAT, which first recovers the profile of absorption coefficients, ABNT circumvents this intermediate process, by directly solving for the distributions of temperature, species concentration, and even pressure, avoiding the requirement that LOS signals have to be integratable.

The mathematical formulation of a typical nonlinear tomographic problem is the focus of this section. As shown in Fig. 11, multiple parallel monochromatic laser beams pass through the region of interest (ROI), which is discretized into a grid of $M \times N$ squares along the x and y directions respectively. The wavelength of the beams is labelled as λ_1; and the laser paths as l_q, with q enumerating all the beams. The measured LOS signals are denoted as 's' and can also be predicted with the function Π, which describes the physical interaction processes between the light and the ROI. They are a function of both the wavelength and the spatial distribution of multiple independent physical parameters denoted as μ's. As in CAT, the assembly of LOS measurements along one orientation in nonlinear tomography is termed *projection*, which leads to a set of nonlinear equations as shown on the right of Fig. 11. If the monochromatic laser beams were replaced with polychromatic ones as shown in Fig. 12, then a 2D (i.e. lateral and spectral dimensions) projection can be obtained as shown on the right of the figure. Through rotational scanning of the ROI, a set of 2D projections can be obtained, resulting in a 3D map (i.e. containing lateral, angular, and spectral dimensions) as shown on the right of Fig. 13. As can be seen, each stack (indicated by a specific color) of the 1D projection shown in the figure is essentially the counterpart of a sinogram in CAT for a specific wavelength. The difference is that each element in the sinogram is treated as a nonlinear equation rather than a linear one as modeled in CAT. In addition, the nonlinear version of the sinogram can bear more dimensions including the harmonic dimension if CFWMS is used to detect multiple orders of harmonic signals. The sinogram contains a set of simultaneous nonlinear equations whose variables are the spatial distributions of the independent variables, i.e. μ. The process of recovering μ from the nonlinear sinogram is called nonlinear tomographic reconstruction.

So far the feasibility of ABNT as an imaging concept has been demonstrated both with DAS [117] and CFWMS [118]. It has been shown that two orthogonal projections are sufficient for a successful tomographic reconstruction featuring intermediate spatial

resolution, but greatly improved temporal resolution. The mathematical formulation for both DAS and CFWMS are summarized in the following sections.

3.1.1. Mathematical formulation of DAS-based nonlinear tomography

In DAS-based nonlinear tomography, the function Π defines Beer's law and μ are the spatial distributions of the flow parameters such as temperature and species concentration. With the aid of nonlinear tomography, the absorption measurements taken at different transitions can be used simultaneously during the reconstruction process, which is not possible with CAT. In this case, by increasing the number of sampled transitions, we can effectively scale up the number of simultaneous equations but at the same time retain the number of variables, i.e. the flow parameters, at every coordinate. The inclusion of additional spectral information can effectively mitigate the harsh requirement for spatial sampling. However, in both the physical and the mathematical senses the spectral information is not equivalent to the spatial counterpart, and thus the deficiencies in spatial sampling can only be compensated to a limited extent by increasing the spectral sampling. However, the incorporation of multispectral information in the tomographic reconstruction will enhance the noise immunity as compared with CAT [120]. Since, in addition to spatial sampling, noise also has a determining effect on spatial resolution, a better immunity to noise will bring beneficial effects to the spatial resolution. In addition, there is no limitation *per se* in the number of projections that can be accommodated by the DAS-based nonlinear tomography, however, this comes with a commensurate loss in temporal resolution, due to the beam scanning requirement [108]. But in this case, DAS-based nonlinear tomography enjoys a much improved reconstruction fidelity, due to better immunity against experimental noise, such as originates from beam steering, window fouling, and etalon fringing [278].

The basic principles of DAS-based nonlinear tomography are illustrated in Fig. 14. To monitor multiple chemical species simultaneously in the reactive flow, broadband light sources such as supercontinuum radiation sources [22,24,25,262–267,279], frequency combs [23,280–282], and Fourier domain mode locking lasers [283–286] could be used to cover a large number of spectral signatures. For the tomographic measurements, the light source is split into multiple beams to map out the ROI or alternatively the beam is translated across the sample volume. This is shown in Panel (a) of Fig. 14, which also serves to illustrate the mathematical formulation of the problem. One of the laser beams positioned at the jth location, denoted by l_j, is directed along the LOS across the non-uniform flow field (left sub-panel). Since the absorbance is accumulative over the absorption path length, the overall absorption spectrum along the LOS is obtained by summing up the spectra of each resolution element traversed by the laser beam (indicated by blue squares in Fig. 14(a). This leads to a projection spectrum (right sub-panel) $p(l_j,\lambda)$ with λ indicating the monitored wavelength. The absorption peaks that can be used for tomographic inversion are named as λ_i with the subscript specifying wavelength indices. The absorbance by the targeting species at λ_i is the summation of contributions from non-negligible neighboring transitions, as expressed by the following equation

$$p(\ell_j,\lambda_i)=\sum_q \alpha_q^{j,i}(T_q,X_q)=\sum_q\sum_k S(\lambda_k,T_q)\cdot X_q\cdot\phi(\lambda_k-\lambda_i,T_q,X_q)\cdot P\cdot\Delta \tag{3.1}$$

where q is the index running through all grid squares crossed by the jth laser beam; λ_k the center wavelength of the kth contributing transition $\alpha_q^{j,i}$ the absorbance at the ith peak wavelength in the qth square; T_q and X_q, the corresponding temperature and concentration respectively; S is the line strength of the contributing transition; P the pressure; Φ the normalized Voigt lineshape function, which approximates the convolution of the two dominant broadening mechanisms (Doppler and collisional); and Δ is the grid spacing. Panels (b) and (c) of Fig. 14 illustrate how different flow parameters affect the spectrum of a specific absorption feature of water vapor. Panel (b) contains three example spectra modeled using data from a spectroscopic database with panel (c) showing normalized versions of the same spectra to allow a better comparison of their shapes. Each spectrum is modeled for a different combination of T_q, X_q, and P_q. Water vapor was chosen in the model due to its prevalence and abundance in hydrocarbon/hydrogen flames, and the availability of frequency agile laser sources to target this species. Collisional and Doppler are the dominant homogeneous and inhomogeneous broadening mechanisms and overall broadening is a convolution of the two, well approximated by a Voigt profile. At atmospheric pressure, the typical full width half maximum (FWHM) of absorption features is ~0.1 cm^{-1} or ~ 0.02 nm in the near infrared and this can easily be resolved by the aforementioned laser sources. We want to point out here that beyond scanning rates of approximately 1 nm per ns, line broadening by the Heisenberg uncertainty principle becomes significant [262]. However, resolution down to 0.1 cm^{-1} resolution is achievable at moderate sweep rates (ca. 100 kHz) [262]. Also,

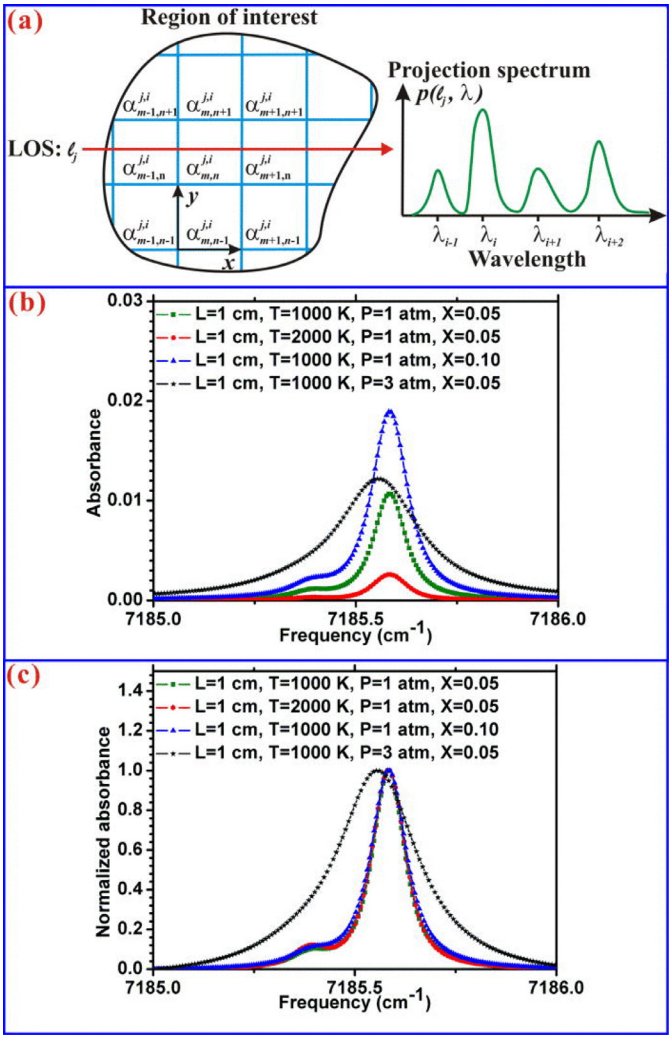

Fig. 14. (a) illustration of the DAS-based nonlinear tomography; (b) spectra of a specific absorption feature of water vapor for different flow parameters; (c) counterpart of Panel (b) with normalized curves. The figures were adapted from [117], with the permission from AIP Publishing.

the features broaden quickly as pressure increases, which make them easier to resolve. It is found that, for the particular feature shown, the absorption intensity decreases with temperature and that the FWHM changes slightly due to the impact of temperature on both line strength and shape. Other spectral features may have different dependencies on temperature. It can also be seen that absorption strength varies almost linearly with concentration. However, the problem is further complicated by the non-uniform distributions of flow parameters. Looking at this problem from another perspective, all information about the flow parameters is contained in $p(l_j,\lambda_i)$; and through suitable mathematical formulation and post-processing, the entanglement of all these factors can be resolved and the spatially-resolved flow field information can be recovered.

The DAS-based nonlinear tomography seeks to reconstruct distributions of flow parameters over ROI and can be formulated into an algebraic nonlinear minimization problem with a cost function defined as

$$D=\sum_{j=1}^{J}\sum_{i=1}^{I}[1-p_c(\ell_j,\lambda_i,T_q,X_q)/p_m(\ell_j,\lambda_i)]^2 \tag{3.2}$$

where J and I denote the total number of laser beams and peak wavelengths used, respectively; $p_m(l_j,\lambda_i)$ the measured projection at the wavelength λ_i along the jth laser beam; and $p_c(l_j,\lambda_i,T_q,X_q)$ the corresponding projection computed with reference to the Beer's law with an appropriate spectroscopic database. The cost function, D, provides a quantitative measure of the similarity between the reconstructed and the actual profiles. The terms contributing to D are the errors in projections, normalized to ensure their equal weighting in the optimization. In an ideal case, where measurements are noise-free and the spectroscopic database is accurate, D reaches its global minimum (zero) when the reconstructions match the true profiles. Additional information, such as smoothness conditions due to thermal and mass diffusion, can be incorporated to steer the optimization process toward a reasonably smooth solution by adding regularization terms into the cost function. For example, the smoothness of temperature can be implemented as the following regularization term:

$$R_T(T^{trial})=\sum_{m=1}^{M}\sum_{n=1}^{N}\left[\left(\sum_{i=m-1}^{m+1}\sum_{j=n-1}^{n+1}|T_{i,j}^{trial}-T_{m,n}^{trial}|\right)/8\right] \tag{3.3}$$

where T^{trial} is the trial temperature distribution for the minimization problem. Obviously, R_T decreases as the distribution becomes smoother and reaches zero when the temperature remains constant (flat profile) across the ROI. Similar term R_X can be implemented analogously for concentration respectively. The cost function can thus be modified as

$$F=D+\gamma_T\cdot R_T(T^{trial})+\gamma_X\cdot R_X(X^{trial}) \tag{3.4}$$

where γ_T and γ_X are weighting parameters employed to regulate the relative significance of *a priori* (smoothness) and *posteriori* (measured projections) information. The regularized minimization problem can then be solved via use of a global minimizer.

3.1.2. Mathematical formulation of CFWMS-based nonlinear tomography

Here, we briefly summarize the basics of the CFWMS with TSLs to facilitate the discussion of CFWMS-based nonlinear tomography. In the CFWMS, the wavelength modulation can be simply realized by imposing a high-frequency sinusoidal modulation on the laser injection current, resulting in laser frequency variations as:

$$\nu(t)=\bar{\nu}+a\cos(2\pi f_m t) \tag{3.5}$$

where $\bar{\nu}$ is the line-center frequency; t the time; and f_m and a are the modulation frequency and depth respectively. The corresponding laser intensity modulation can be described by

$$I(t)=\bar{I}_0\cdot[1+i_0\cos(2\pi f_m t+\psi_1)+i_2\cos(4\pi f_m t+\psi_2)] \tag{3.6}$$

where $\bar{I}_0$ is the average laser intensity at the line-center; i_0 and i_2 the linear and nonlinear modulation amplitudes; and ψ_1, ψ_2 are the corresponding phase shifts with respect to frequency modulation. For small a, e.g. $a<0.1\ \mathrm{cm}^{-1}$, i_2 is negligible and in this case the laser intensity scales linearly with driving current.

According to Beer's law, the transmission coefficient of a monochromatic light beam with frequency ν passing through a *non-uniform* absorbing medium is defined as:

$$\tau(\nu)=\exp[-\alpha(\nu)]=\exp\left\{-\int_{L_1}^{L_2}\sum_{g}S[T(l),\nu_g]\cdot\varphi[T(l),X(l),P\cdot(\nu_g-\nu)]\cdot P\cdot X(l)\right\} \tag{3.7}$$

where L_1 and L_2 are the intersections between the laser beam and the boundaries of the region of interest (ROI); $T(l)$ and $X(l)$ the temperature and concentration profiles along the LOS as a function of distance l respectively; ν_g the frequency of the gth non-negligible transition.

Since $\tau(t)$ is an even function with respect to t, it can be expanded as a Fourier cosine series:

$$\tau\left(\bar{\nu}+a\cos(\omega t)\right)=\sum_{k=0}^{\infty}H_k(\bar{\nu},a)\cos(k\omega t) \tag{3.8}$$

where H_k represents the kth order harmonic coefficient which can be calculated as

$$H_0(\bar{\nu},a)=\frac{1}{2\pi}\int_{-\pi}^{\pi}\tau(\bar{\nu}+a\cos\theta)d\theta \tag{3.9}$$

$$H_k(\bar{\nu},a)=\frac{1}{\pi}\int_{-\pi}^{\pi}\tau(\bar{\nu}+a\cos\theta)\cos k\theta d\theta \tag{3.10}$$

The 1st and 2nd harmonics of the signal (denoted by S_{1f} and S_{2f}) can then be calculated *via* Eqs. (3.11) and (3.12). The laser parameters i.e. i_0, i_2, ψ_1, ψ_2, and a are determined according to the method detailed in [287].

$$S_{2f}=\frac{G\bar{I}_0}{2}\left\{\left[H_2+\frac{i_0}{2}(H_1+H_3)\cos\psi_1+i_2\left(H_0+\frac{H_4}{2}\right)\cos\psi_2\right]^2+\left[\frac{i_0}{2}(H_1-H_3)\sin\psi_1+i_2\left(H_0-\frac{H_4}{2}\right)\sin\psi_2\right]^2\right\}^{1/2} \tag{3.11}$$

$$S_{1f}=\frac{G\bar{I}_0}{2}\left\{\left[H_1+i_0\left(H_0+\frac{H_2}{2}\right)\cos\psi_1+\frac{i_2}{2}(H_1+H_3)\cos\psi_2\right]^2+\left[i_0\left(H_0-\frac{H_2}{2}\right)\sin\psi_1+\frac{i_2}{2}(H_1-H_3)\sin\psi_2\right]^2\right\}^{1/2} \tag{3.12}$$

Here G is a scaling factor accounting for both the optical and electrical gains of the detection system and transmission losses caused by scattering, reflections, beam steering, window fouling, etc. By taking the ratio of Eqs. (3.11) and (3.12), the pre-factor cancels out. The result, labeled as $S_{2f/1f}$, defines the 1f-normalized, 2f signal that provides a calibration-free measurement unaffected by G. The normalized signal thus only depends on laser parameters and absorber properties (i.e. temperature and concentration) [288–290]. For CFWMS-based nonlinear tomography, Eqs. (3.11) and (3.12) actually serve as the function f as introduced in Section 3.1. It has to be noted that a more accurate model for the calculation of the 1f-normalized, 2f signals have been developed [276,291], which will be implemented in a future version of ABNT.

Fig. 15 illustrates how the CFWMS-based nonlinear tomography might be implemented in principle using currently available technology. Multiple laser diodes are used to probe multiple transitions of the target species at the line centers with frequencies of ν_q, and their output is combined using a wavelength multiplexer. Each of the diodes is modulated at a frequency that is different from the others so that its harmonic signals can be differentiated using lock-in amplifiers. The multiplexed laser source can then either be split into multiple beams to map out the ROI, or laterally translated across the ROI in a step-wise fashion at the cost of reduced temporal resolution. As illustrated in Fig. 15, a beam at the jth measurement location, l_j, is attenuated on passage through the ROI by sample absorption, and picked up by a photo detector. The registered signal is digitized and post-processed using a lock-in detection algorithm, implemented in software, to recover the harmonic signals. This recovers Q nonlinear equations for $S_{2f/1f}$ at each l_j, where Q corresponds to the number of transitions probed. Each $S_{2f/1f}$ is a function of the profiles of temperature and species concentration along the LOS. Thus, the tomographic sampling essentially results in a 3D (angular, lateral, and spectral) sinogram and also a system of $l_j \times Q$ coupled nonlinear equations. Similar to DAS-based nonlinear tomography, the current equation system can also be transformed into an optimization problem with an objective function defined as:

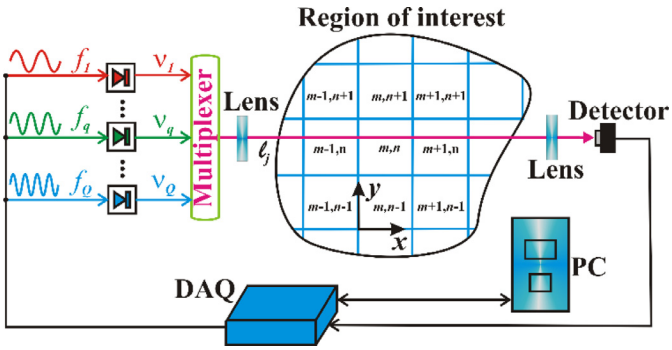

Fig. 15. Illustration of multiplexed CFWMS-based nonlinear tomography. This figure was adapted from [118], with the permission from AIP Publishing.

$$F = D + \gamma_T \cdot R_T(T^{trial}) + \gamma_X \cdot R_X(X^{trial}), D = \sum_{j=1}^{J}\sum_{i=1}^{I}\left[1 - S^{c}_{2f/1f}(\ell_j, \lambda_i, T^{trial}, X^{trial})/(S^{m}_{2f/1f}\ell_j, \lambda_i)\right]^2 \quad (3.13)$$

where indices i and j run through all the probed transitions and measurement locations respectively. $S^{m}_{2f/1f}$ and $S^{m}_{2f/1f}$ are the calculated and measured 1f-normalized, 2f signals respectively. By comparing Eqs. (3.4) and (3.13), we can see that the only difference between the cost functions is the term D, which is the model that is used to predict the measured signal. So far, the pressure distributions have been assumed to be uniform in demonstrations of CFWMS-based nonlinear tomography. For applications with non-uniform pressure distributions, the situation becomes more complicated because the optimal modulation depth is lineshape-dependent, and both pressure and concentration have an effect on the line profile. However, the entanglement between pressure and concentration can be resolved just like in the FAT case because the 1f-normalized 2f signal has different dependencies on pressure and species concentration, i.e. the absorption signal has a strong nonlinear dependency on pressure but scales almost linearly with species concentration.

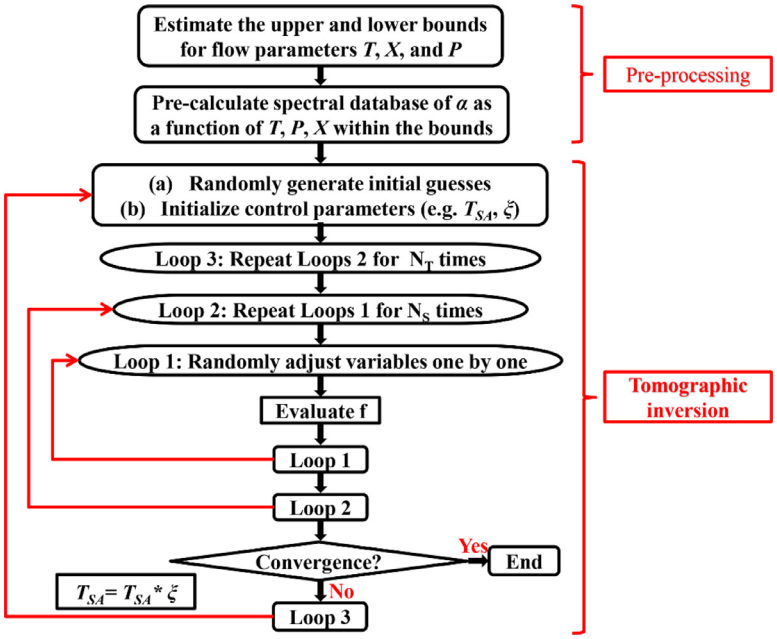

Fig. 16. Flow chart of a typical simulated annealing algorithm suited for the optimization of a nonlinear tomography problem. This figure was partially adapted from [305].

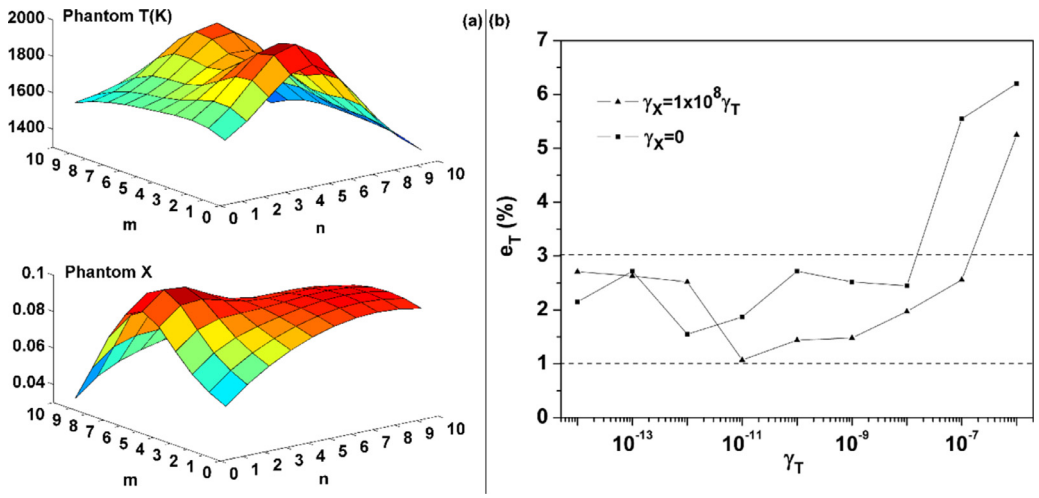

Fig. 17. (a) Simulated 10 × 10 phantom distributions for temperature, T in K, and water vapor concentration, X, used as input for the simulation to demonstrate the choice of regularization parameters on the temperature error e_T during simulated annealing; (b) Normalized error (e_T) of T reconstruction for different combinations of parameters γ_T and γ_X. Clearly the method is insensitive to both parameters over a wide range of values. Figures were adapted from [306].

3.2. Numerical investigations

In contrast to CAT, which leads to a set of linear algebraic equations with local absorption coefficients as the variables, both DAS- and CFWMS-based nonlinear tomographies result in an algebraic nonlinear equation system. Because of this, none of the tomographic algorithms introduced in Chapter 2 can be applied here. As discussed in previous sections, the nonlinear tomographic problem is usually converted to an optimization problem, so that additional information such as the smoothness conditions acting as the constraints can be incorporated to alleviate the underdetermined problem and guide the optimization process towards a more sound physical solution. However, optimization, or to be more specific, minimization of the cost function, is not a trivial task since it involves hundreds, or even thousands, of variables, which create millions of local minima in the solution space and make the gradient-based techniques [292,293] impractical. Thus, a robust global optimization algorithm is needed to escape local minima effectively and to land in the vicinity of the global minimum. It has been proven that heuristic algorithms such as the simulated annealing (SA) algorithm [294–298], genetic algorithm (GA) [299–301], and differential evolution (DE) algorithm [302–304] are efficient in solving large-scale optimization problems. So far, the SA algorithm has been favored for the solution of the nonlinear tomographic problems; it is briefly summarized here.

3.2.1. The simulated annealing algorithm

The SA algorithm is a well-established tool that has been widely employed in large-scale optimization problems to pinpoint the global minimum among interfering local minima. A well-recognized advantage of SA is its insensitivity to the initial guesses, which is a critical difference to derivative-based algorithms [119]. The SA concept originated from metallurgy and was first proposed in 1983 [15]. The algorithm mimics the annealing process of liquids, which are cooled down slowly until crystallization occurs, i.e. a state with minimal internal energy is reached. During the annealing process, the temperature of the liquid has to be lowered slowly enough such that the system can escape local energy minima via random thermal fluctuations; otherwise, the system can become trapped in a higher energy state. In the SA algorithm, the cost function that is to be minimized is analogous to the internal energy of the liquid system that has to be lowered. The corresponding parameter, T_{SA}, is defined so that the annealing rate can be artificially controlled. The random "thermal fluctuations" are simulated mathematically by the so-called Metropolis criterion, whose algorithm is defined as

$$\begin{aligned} &\text{if}\Delta F = F(\vec{x}_{new}) - F(\vec{x}_{old}) \le 0, \text{accept } \vec{x}_{new} \\ &\text{else accept } \vec{x}_{new} \text{with probability } p_{SA} = \exp(-\Delta F/T_{SA}) \end{aligned} \tag{3.14}$$

where x^- represents the variables of F; $\vec{x}_{new}$ is obtained by randomly adjusting one of the variables in $\vec{x}_{old}$; and ΔF is the change in the cost function. Eq. (3.14) represents the key step of the SA algorithm, in which a new solution ($\vec{x}_{new}$) is always accepted if it results in a lower F; however, even a new solution which results in a higher F, is not automatically rejected and is instead accepted with a certain probability p_{SA} (to mimic random thermal perturbations). During the annealing process, T_{SA} is gradually reduced, and the probability of acceptance as well as the magnitude of the thermal perturbations decrease, resulting in convergence toward the optimal solution within the searching space. The Metropolis criterion distinguishes SA from deterministic optimization algorithms, in which the improvement is always accepted and deterioration is always rejected.

The block diagram shown in Fig. 16 gives an exemplar implementation of the SA algorithm, which is detailed in [298]. Before the algorithm starts, the lower and upper bounds for the flow parameters, i.e. T and X, are estimated. For better computational efficiency, a database α of absorption coefficients for the chosen transition are pre-calculated for the flow parameters delimited by the bounds. The tomographic inversion process follows these two pre-processing steps and mainly consists of three computational loops. In the innermost loop (Loop 1), one variable of $\vec{x}_{old}$ is adjusted randomly (to become $\vec{x}_{new}$) and the cost function F is then calculated. The adjustment is accepted or rejected according to the Metropolis criterion. The loop cycles through all the variables sequentially and is repeated for N_S times by the middle loop (Loop 2). The step lengths (the magnitude of x^- variations) are then optimized according to the acceptance rate [298]. The outermost loop (Loop 3) then repeats the middle loop for N_T times. If the convergence criterion is met after completion of the three nested loops, the algorithm will be terminated; otherwise the temperature T_{SA} is reduced ($T_{SA} = T_{SA} \times \xi$, where $0 \le \xi \le 1$) and the loops are iterated until the termination criterion is satisfied. The termination criterion can be set, e.g., as the relative improvement in F_{opt} between the last two, or even more, consecutive temperature states (T_{SA}). The higher the thermal perturbation, the more iterations the algorithms will go through, the annealing rate slows down as ($\xi \to 1$), and the more likely the optimal solution can be located; however this comes at the cost of

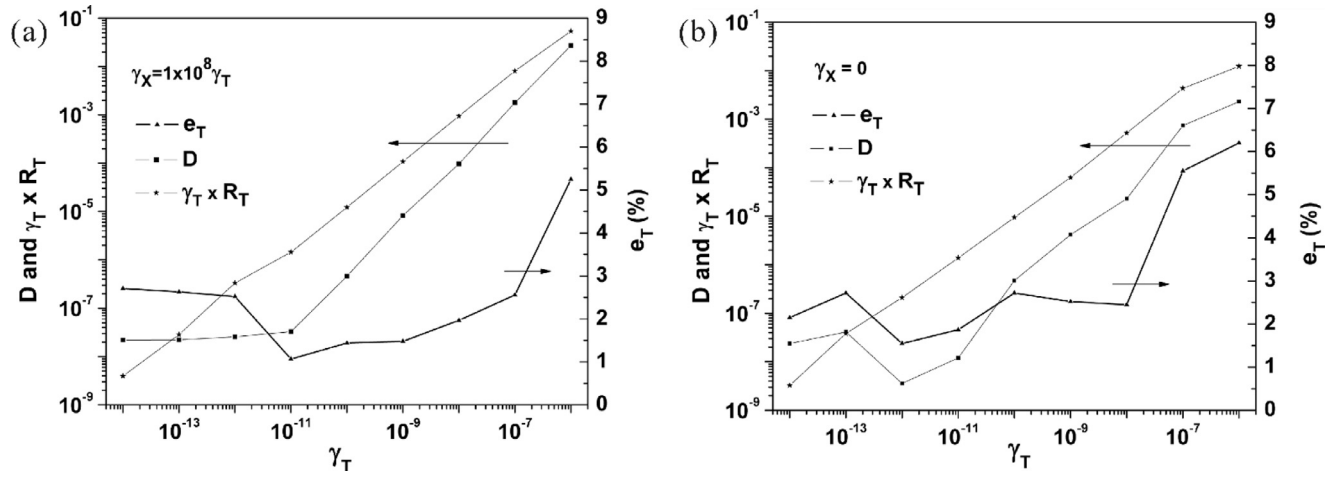

Fig. 18. Contribution from D and the regularization factor to the regularized cost function, F, at different values of γ_T, with (a), $\gamma_X = 1 \times 10^8 \gamma_T$; and (b), for $\gamma_X = 0$. Figures were adapted from [306].

increased computational time. It can be inferred from the optimization process that the number of function evaluations will increase as the discretization grid becomes more finely spaced. Since the computational cost for each function evaluation also increases with pixel number, the computational cost increases exponentially with the size of the nonlinear tomographic inversion problem. It has been shown in [108] that the performance of ABNT will first improve and then deteriorate as the meshing scale increases.

3.2.2. Determination of the regularization factors

As introduced in the previous sections, one of the advantages of nonlinear tomography is that additional flow information can easily be accommodated in the cost function. For example, the smoothness conditions for temperature and species concentration profiles can be integrated in the cost function, via inclusion of regularization terms as shown in Eqs. (3.4) and (3.13). However, the regularization factors, which control the relative strengths of the *posterior* and *a priori* information have to be determined properly, so that a good approximation of the optimal solution can be obtained. For example, if the regularization factors are larger than optimal, then the final solution will be over-smoothed; in the opposite case, the smoothness conditions will not be satisfied. The method of choosing appropriate regularization factors was systematically investigated through numerical simulations in Ref. [306]. In the study, H_2O was assumed to be the target species, and phantoms of T and X were created to mimic multimodal and asymmetric distributions as are typically encountered in practical combustion devices (Fig. 17(a)). The ROI was meshed into 10×10 square pixels. The simulations were performed for ten absorption transitions measured with two orthogonal projections, over ten LOS measurement locations. To quantify the reconstruction quality, the normalized temperature and concentration errors e_T and e_X were defined as

$$e_T = \|\vec{T}^{\,rec} - \vec{T}^{\,true}\|_1 / \|\vec{T}^{\,true}\|_1, \quad e_X = \|\vec{X}^{\,rec} - \vec{X}^{\,true}\|_1 / \|\vec{X}^{\,true}\|_1 \tag{3.15}$$

where superscripts distinguish between the phantoms as the ground truth distributions ('*true*') and the reconstructions ('*rec*'); $\|\|_1$ denotes the 1- norm.

As discussed earlier in Section 3.1.1, the temperature affects the lineshapes of the absorption features and the species concentration has a major impact on the magnitude of the absorbance. Due to their distinct signal responses, the profiles of temperature and concentration can be recovered in two separate steps. As demonstrated in Ref. [306], a faithful reconstruction of the temperature profile is achieved by optimizing Eq. (3.4), regardless of the quality of the concentration reconstruction. This is shown in Fig. 17(b) (squares), which was

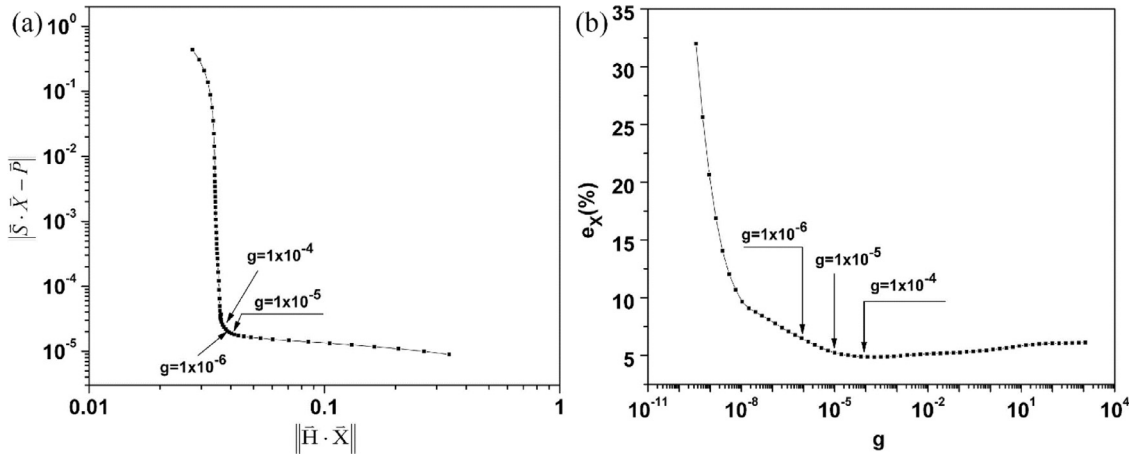

Fig. 19. (a) Plot of the residual versus the regularization factor with weightings g ranging from 10^{-9} to 10^3, resulting in an L-shaped curve with a distinct corner; (b) Values of the species concentration error e_X at different weightings g for the regularization, illustrating the minimum e_X corresponds to a g situated near the corner of the L-curve. Figures were adapted from [306].

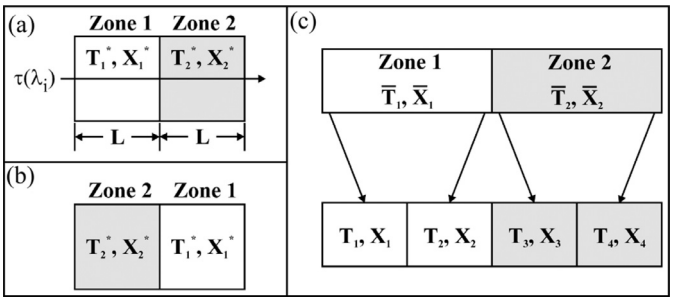

Fig. 20. (a) Illustration of the simple two-zone problem. (b) illustrates that the two-zone problem has at least two solutions regardless of the transitions used. (c) illustrates how the LOS features two spatially distinct regions with individual temperatures and species distributions T_i^*, X_i^*, respectively and how an arbitrary distribution can be broken down into a series of two-zone problems. Figure adapted from [312], with the permission from SAGE Publications.

obtained when the regularization parameter $\gamma_{\boldsymbol{X}}$ is set to 0, i.e. no smoothness condition is applied for the spatial concentration distribution. The triangles represent the cases for $\gamma_X = 1 \times 10^8 \gamma_T$. Good performance is evident for γ_T spanning multiple orders of magnitude for both settings of γ_X. At a certain $\gamma_{\boldsymbol{T}}$, both D and $R_{\boldsymbol{T}}$, as defined in Eq. (3.13) contribute equally to the regularized cost function as shown in both Fig. 18(a) and (b). In this case, good solutions were obtained. Sensitivity analyses of this type can be used to provide guidelines for the selection of values for $\gamma_{\boldsymbol{T}}$.

With the T distribution obtained from the previous discussion (denoted as T^{rec}), the reconstruction of species concentration becomes a linear inversion problem and can be written in the following matrix format:

$$\vec{p}_m = S(T^{rec}, \lambda) \cdot \vec{X} \tag{3.16}$$

where $\vec{p}_m$ represents the LOS measurements and $\vec{X}$ the concentration profile organized into column vectors respectively. S is a matrix with a dimension of 200×100 (20 beams, 10λ's, and 10×10 pixels), which contains the calculated absorbance values for a pure absorbing gas at each transition line within each individual pixel that is covered by each LOS measurement using the obtained T^{rec}. Eq. (3.16) can be solved via least-squares minimization to yield $\vec{X}$. However, the S matrix is usually ill-conditioned, i.e. with a large condition number, and the solution of Eq. (3.16) is therefore usually compromised by noise. A linear regularization technique is necessary to alleviate the rank-deficiency of Eq. (3.16). The regularized version of Eq. (3.16) is defined as follows:

$$\min \| \vec{p}_m - S(T^{rec}, \lambda) \cdot \vec{X} \| + g \cdot \| L \cdot \vec{X} \| \tag{3.17}$$

where the $\| \bullet \|$ notation represents the Euclidean norm of a vector, L again is a regularization operator realized in a matrix format, and g is the corresponding regularization factor that controls the relative strengths of the two terms in Eq. (3.17). This regularization method is well-established and has been studied extensively [307–310]. The so-called L-curve method described in Ref. [308] can be applied to determine the optimal g for a valid solution of the concentration distribution.

The method involves the solution of Eq. (3.17) at different values of g and the calculation of the corresponding residual (the left term in Eq. (3.17)), and the regularization term $\| H \cdot X^{-} \|$. When the two terms are plotted against each other, an L-shape curve is obtained as exemplified in Fig. 19(a). The optimal regularization factor is then determined by locating the position near the corner of the curve, which has the maximum curvature. In this example, a γT of 10^{-10} and a γX of 10^{-2} were used in a first step to obtain the *Trec*, corresponding to an e_T of 1.44%. After the S matrix is evaluated using this *Trec* obtained, Eq. (3.17) is solved for various values of g, ranging from, $g = 10^{-9}$ to 10^3. The range of g is suggested by the following quantity:

$$g^0 = Tr(S^T \cdot S) / Tr(H^T \cdot H) \tag{3.18}$$

where Tr is the trace of the matrix. A good choice of g, according to Eq. (3.18), results in the residual and regularization factor to become comparable in magnitude [311]. Then, a range, centered at g^0, is determined to vary g. The corresponding values of g around the corner are labelled on the plot and, as Fig. 19(b) demonstrates, these values of g indeed yield a small e_X. In this example, the minimum e_X (4.9%) occurs at a g of $\sim 1 \times 10^{-4}$, which is very close to the turning point of the corner. As demonstrated in Ref. [120], this method yields a stable and accurate reconstruction of X.

3.2.3. *Selection of the optimal transition lines*

In both DAS- and CFWMS-based tomography, multiple absorption transitions are used in the tomographic reconstruction. The selection of the optimal set of absorption transitions that can be covered by the laser sources are extremely important since their sensitivity and response to variations in temperature and species concentration vary greatly, which can significantly affect the reconstruction quality. The method of selecting the optimal set of transitions is detailed in Ref. [312] and is only briefly summarized here. In [263], a limited number of promising candidate transitions were pre-selected (only 15 were used in the demonstration to reduce the computational cost) according to criteria widely used in two-line thermometry methods with a view to maximize the temperature sensitivity of the LOS measurements. The details of the pre-selection can be found in Ref. [287]. The candidate transitions were then tested to solve the two-zone problems based on the hypothesis that if a set of transitions is optimal for a specific two-zone field, it should also be optimal for a general non-uniform field distribution. It has to be noted that for a two-zone problem, the absorption measurement

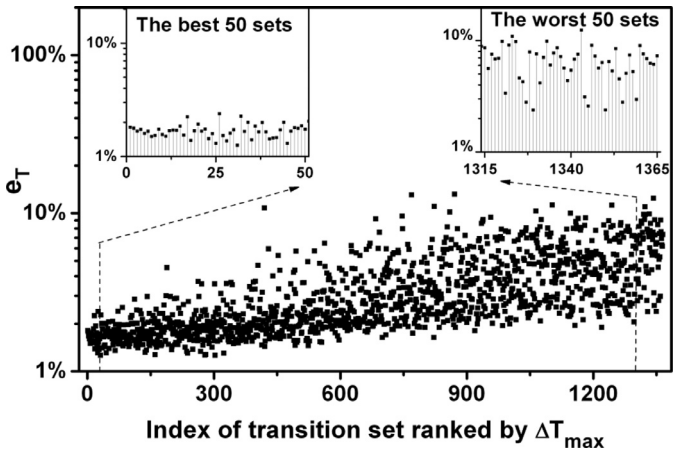

Fig. 21. Distribution of temperature errors e_T obtained with different sets of transitions. The index of each set is ranked according to ascending values of ΔT_{max}. This figure was adapted from [312], with the permission from SAGE Publications.

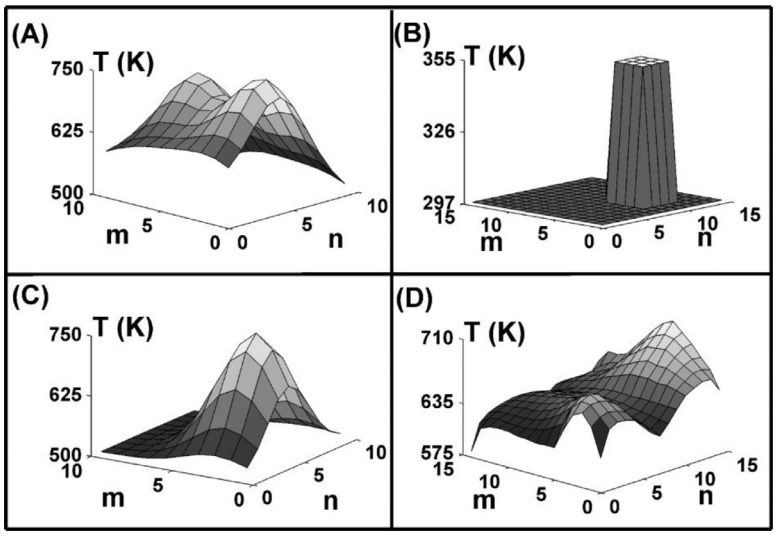

Fig. 22. Example phantoms tested in the validation. (From [312], with the permission from SAGE Publications).

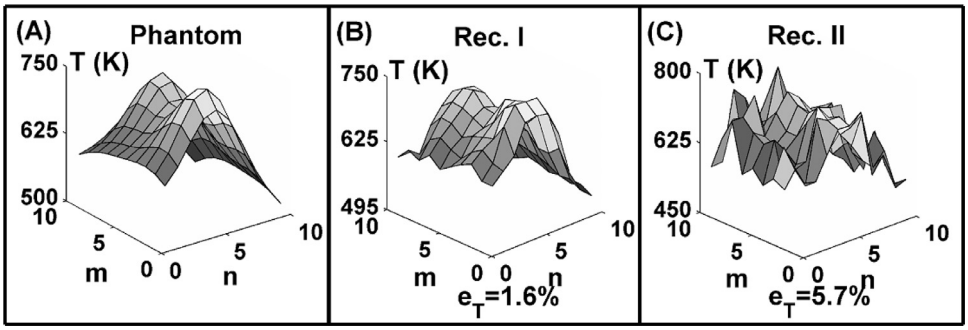

Fig. 23. Reconstruction quality with both the optimal set (Panel (B)) and a non-optimal set (Panel (C)) of transitions. (From [312], with the permission from SAGE Publications).

cannot distinguish the order of the two zones, even though correct T and X can be recovered for both, as demonstrated in Fig. 20(a) and (b). Fig. 20(c) illustrates how a series of two-zone problems is conceptually equivalent to a 1D problem with higher resolution. The field can first be decomposed into two zones with $(T_1^*, T_2^*, X_1^*, X_2^*)$ representing the average T and X for each zone respectively. This process is then repeated until the desired resolution is achieved. The subsets of the pre-selected transitions are then used to solve representative two-zone problems. Each subset is used to solve the problem repeatedly and the worst case featuring the maximal ΔT (defined in Eq. (3.19)) is recorded.

$$\Delta T = \min[\sqrt{(T_1-T_1^*)^2+(T_2-T_2^*)^2}, \sqrt{(T_1-T_2^*)^2+(T_2-T_1^*)^2}] \tag{3.19}$$

In the demonstration, all possible combinations of 4 out of the 15 pre-selected transitions were used to solve five basic two-zone problems. An artificial Gaussian noise of 1% (relative) was added to the LOS measurements to simulate experimental conditions. The ΔT's of each combination were calculated according to Eq. (3.21) and the maximum ΔT_{max} recorded. The overall ΔT_{max} was then obtained by summing up the ΔT_{max} obtained from each individual two-zone problem. The temperature error e_T obtained using each combination is plotted in Fig. 21 with ΔT_{max} arranged in an ascending order, so that the correlation between e_T and ΔT_{max} can be easily observed. The best 50 combinations feature a consistently smaller e_T and variance than the worst 50 combinations, which proves the validity of the method. Results from the selected optimal set of transitions were compared to those of a non-optimal set for various representative phantoms, of which four are shown in Fig. 22. The same conclusions were drawn for all examples. Hence, here we only reproduce one such example from [312] in Fig. 23. It clearly shows that the optimal transition set outperforms the non-optimal set.

3.2.4. Time-correlated reconstructions

It has been demonstrated that a high temporal resolution, reaching MHz repetition rates, can be realized for tomographic measurements. But the associated high cost for the tomographic reconstructions is often intractable. On the other hand, reactive flows can often be approximated to be smooth in the temporal domain, such that there is a correlation between consecutive measurement frames. This can be taken advantage of to reduce the size of the optimization problem, i.e. the number of variables, and hence the computational complexity is decreased. Even dynamic events, such as flame lift off and blow out, often occur on the ms timescale, and can be sampled frequently during their occurrence, such that flow properties are nearly unchanged within a grid element between consecutive frames. The overarching criterion is that the sampling rate exceeds the rate of change of flow properties to a significant degree. The tool that

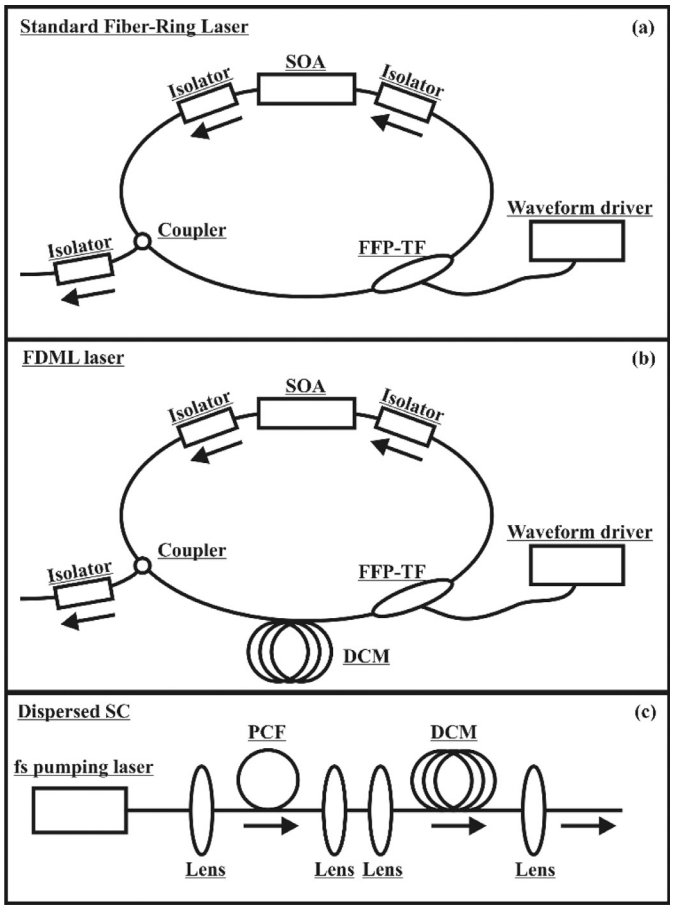

Fig. 24. Illustration of broadband light sources for ABNT. SOA: semiconductor optical amplifier; FFP-TF: fiber Fabry-Perot tunable filter; FDML: Fourier domain mode-locking; SC: supercontinuum; PCF: photonic crystal fiber. (a): a standard fiber-ring laser which contains a SOA as the gain media and a FFP-TF as the wavelength selector; (b): a FDML laser which is essentially a fiber-ring laser incorporating a delay line; (c): a dispersed SC source which uses a PCF for spectral broadening and a dispersion compensation module (DCM) for spectral dispersion.

can be employed to exploit temporal correlations is again the POD technique, which was briefly introduced in Section 2.2.5 and is also detailed in Ref. [305].

In difference to CAT, in which the training functions are the distributions of the absorption coefficients, the counterpart in DAS-based nonlinear tomography are the T and X distributions obtained from previous measurements or numerical simulations. By performing POD, the eigenfunctions for both T and X can be obtained. A fraction of the eigenvectors with the largest eigenvalues can be used to predict the reconstructions. The mathematical expression for this step is defined as

$$\vec{T} = \sum_{k=1}^{K} \zeta_k \vec{\Phi}_k \tag{3.20}$$

where $\vec{\Phi}_k$ are the eigenfunctions, ζ_k represents the weighting factors, T^- is the temperature distribution arranged in a vector format, and K is the total number of eigenfunctions used in the representation. The X distribution can be reproduced in a similar way. When the approximations of T and X are substituted into Eq. (3.4), the cost function, F, becomes a function of the weighting factors instead of T and X on each grid point. Since the number of weighting factors (K) is significantly less than that of the grid elements, the scale of the optimization problem can be greatly reduced. The POD approximation greatly reduces the number of variables in the problem with an associated reduction in the computational cost proportional to N^2/K, where N^2 is the number of elements in the ROI.

The major advantages of using the POD method are three-fold: 1) regularization is not needed since the extracted eigenfunctions are smooth; 2) better reconstructions can be obtained since the scale of the optimization problem is reduced and also the control of the bounds is improved; and 3) the application of POD also improves the noise-immunity of the tomographic inversion, as discussed in Ref. [305].

3.3. Experimental demonstration and applications

3.3.1. Wavelength-swept lasers

Theoretically, any lasers with sufficiently narrow line-width for gas sensing can be used for absorption tomography as long as it can be wavelength-tuned to cover a good number of absorption features of the target flow species. However, for certain reactive flows, such as turbulent flames, a high temporal resolution is necessary to freeze the flow and track transient phenomena. Thus, wavelength-swept lasers with high tuning agility are desirable for these applications. Rapid wavelength tuning can be realized by either extra- or intra-cavity filtering, depending on where the wavelength selection takes place. In the former case, the wavelength-selective element, e.g. a dispersing fiber, is positioned outside of the cavity and wavelength sweeping takes place after broadband laser radiation is generated. In the other case, the wavelength-selective element is contained inside the laser cavity so that only a certain wavelength is amplified during the lasing process. The wavelength agile lasers that have been successfully used, or have the potential to be used, for DAS-based nonlinear tomography are illustrated in Fig. 24 and are briefly introduced in the following sections.

Panel (a) of Fig. 24 shows a standard fiber-ring swept wavelength laser, which contains a fiber Fabry-Perot tunable filter (FFP-TF) within the ring cavity. The gain medium is a semiconductor optical amplifier (SOA) sandwiched between two optical isolators to suppress reflections from optical surfaces and to guarantee a unidirectional propagation of the photons. Through amplified spontaneous emission, the SOA starts to emit broadband radiation which is then spectrally filtered by the FFP-TF. The filtered radiation will then be amplified through stimulated emission (SE) after multiple round-trips within the cavity, until the active medium is saturated. The output wavelength can be tuned via the waveform driver, which tunes the FFP-TF to sweep through the gain window of the SOA. The sweeping rate of the laser is limited by the rate of slow lasing processes, i.e. ASE [313]. To overcome this limitation, a new design of the ring cavity was recently proposed, as illustrated in Panel (b). The new design incorporates a delay line, so called dispersion compensation module (DCM), within the cavity so that some photons remain in the cavity to act as seeds for the SE processes of following sweeps. The driving frequency of the filter must match the delay time of the stored sweep in the delay line so that the correct seeding wavelengths pass the filter at the correct time to be amplified by the SE processes. This conceptually simple modification greatly reduces the lasing buildup time and thus increases the achievable sweeping rate dramatically. Theoretically, the sweeping rate of the laser is only limited by the SOA carrier relaxation time, which is typically below a nanosecond. In addition, the spectral range of the laser is limited by the gain window of the SOA, which usually spans tens of nanometers. Since the frequency or spectral information is transformed into temporal information through wavelength chirping, the device is named Fourier domain mode locking (FDML) laser [283–285,314].

Supercontinuum radiation is another type of spatially coherent broad bandwidth radiation, which can be rapidly wavelength tuned outside of the laser cavity as depicted in Panel (c). Octave spanning supercontinuum radiation is generated by pumping short (ps or shorter) pulses into a photonic crystal fiber [25] where nonlinear effects such as self-phase modulation, stimulated Raman scattering, and four-wave mixing lead to massive spectral broadening [265,315]. The color spectrum of the ensuing broad bandwidth

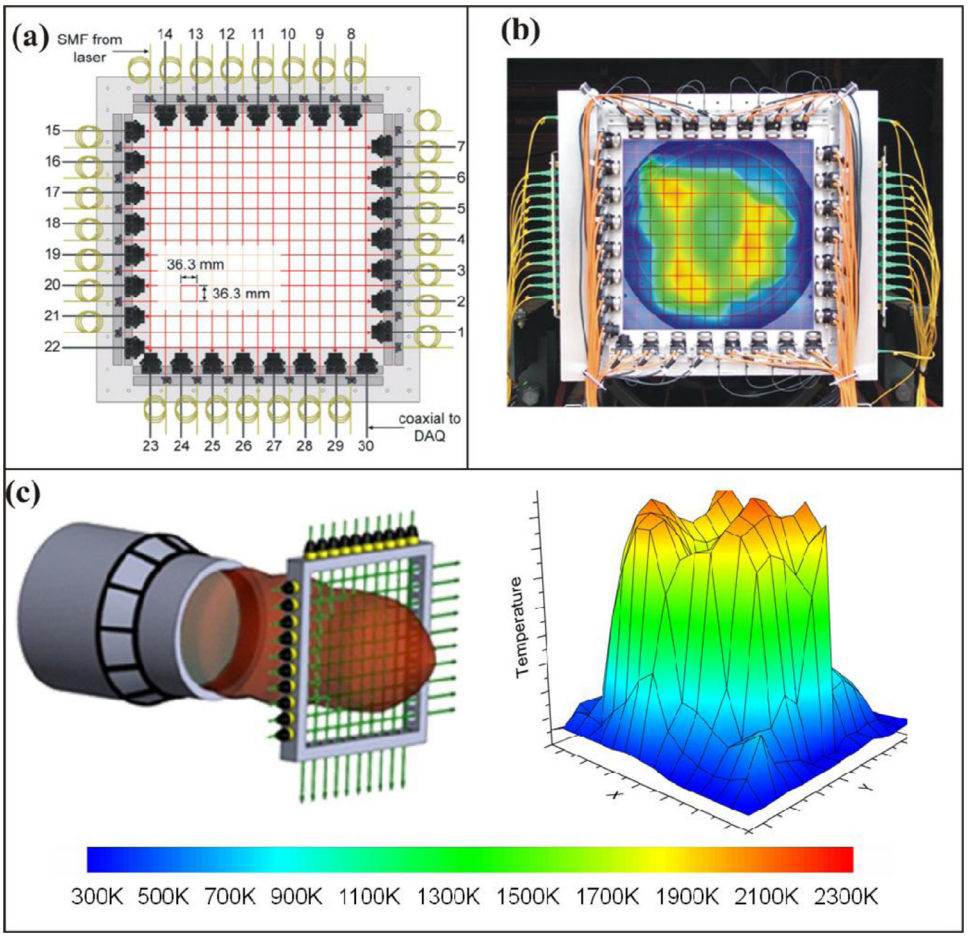

Fig. 25. Panels (a)-(c) give a schematic representation of the optical test section. A 15 × 15 grid pattern of crossing beams with a 36.3 mm beam spacing was used for the tomographic reconstruction. Panel (a): configuration of the probe beams; SMF: single mode fiber. Panel (b): a photograph of the frame and the optical components overlaid by a sample temperature reconstruction to illustrate the location of the flow field. Panel (c): schematic of the location of the measurements plane in the exhaust and a sample measurement of the 2D temperature distribution measured at this location. (adapted from [239]).

pulses is temporally dispersed *via* passage through a long dispersive fiber. A spectrum is then recorded for each pulse simply by recording the time resolved signal on a high bandwidth photo-detector and sweep rates of up to 1 nm per ns are possible, beyond which the spectral resolution becomes limited by the Heisenberg uncertainty principle [265]. Detailed implementations of this ultra-fast wavelength-sweeping technique are covered in [22,24,264].

3.3.2. *Experimental applications*

High-speed tomographic imaging has found a range of applications in the combustion area, e.g. the development of next-generation engines such as the Homogeneous Charge Compression Ignition and scramjet engines. The DAS-based nonlinear tomography, on the other hand, has so far been experimentally validated with a two-zone problem [316], and demonstrated on a Hencken burner [119] and a gas turbine engine [239].

Here we summarize the most recent application of DAS-based nonlinear tomography for flow measurements at the exhaust plane of the augmenter-equipped J85-GE-5 gas turbine engine as an example [239]. The tomographic sensor consisted of three synchronized FDML lasers covering different regions in the near-infrared spectrum. The outputs from the lasers were combined and split into 32 beams using an optical multiplexer. A total of 30 laser beams were used to probe the ROI, with 15 arranged horizontally and 15 vertically as shown in Panel (a) of Fig. 25. The remaining two beams were monitored to provide references for the laser intensity and wavelength scan, respectively. The probing beams were installed on a custom-built aluminum frame as shown in Panel (b) of Fig. 25, delivered by single-mode fibers and collected by photodetectors. Panel (c) depicts the location of the measurement plane in the exhaust and one example of the measured 2D distribution of temperature measured. The analog voltage signals from the photodetectors were digitized and stored for subsequent processing using the aforementioned tomographic algorithms. The measurements were taken at a repetition rate of 50 kHz and measured projection data used to recover temporally-resolved T and X distributions. Although only two orthogonal projections were used in this application, there is no limitation *per se* in the number of projections that can be accommodated by DAS-based nonlinear tomography. Both the spatial resolution and accuracy will be improved, as more projections are used. The reader is referred to Ref. [239] for more details.

4. Conclusions

Tomographic absorption spectroscopy (TAS) is evolving into a mature technique in studies of gas dynamics and reactive flows. It is capable of mapping major non-fluorescent flow species such as H_2O, CO_2 and hydrocarbons with high sensitivity and speed. Examples include the successful demonstration on multi-cylinder and single-cylinder automotive engines for hydrocarbon imaging with crank-angle resolved temporal resolution. This imaging capacity makes it a perfect complement to planar imaging techniques such as laser-induced fluorescence. The latter usually provide better temporal and spatial resolution compared to tomographic absorption methods,

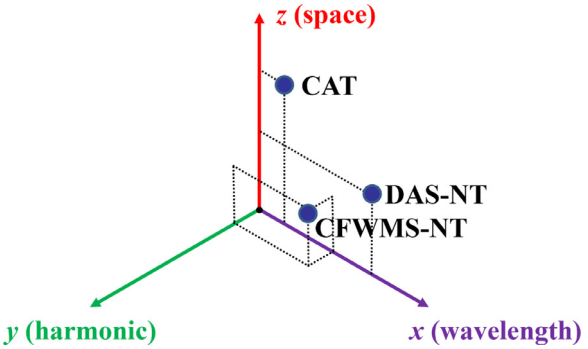

Fig. 26. Summary of tomographic absorption techniques in terms of sampling schemes. CAT: classical absorption tomography; CFWMS: calibration-free wavelength modulation spectroscopy; DAS: direct absorption spectroscopy; NT: nonlinear tomography.

however they are restricted to situations where optical access is abundant and to the detection of fluorescent species, which makes them impractical in many technical combustion environments. The field is likely to see enormous developments in the near future through recent progress in the technology of broadband sweeping lasers, detector technologies, advancing absorption spectroscopy modalities, and in the theory of nonlinear tomography, bringing new opportunities for TAS to be deployed for combustion diagnostics. For example, the advent of high-repetition rate, octave-spanning supercontinuum sources makes the simultaneous imaging of multiple flame species possible. The establishment of nonlinear tomography enables the incorporation of multispectral information within a single tomographic inversion, something that is not possible with classical tomography. Its realization also brings other advantages, such as an enhanced immunity against experimental noise. Furthermore nonlinear tomography enables a combination with wavelength modulation spectroscopy, which is calibration free and features high sensitivity.

The conceptual difference between classical absorption tomography (CAT) and absorption-based nonlinear tomography (ABNT) is not the number of absorption transitions that are used in a measurement but the way in which the measured data are processed. For example, multiple wavelengths can also be used in CAT but the sinograms are processed sequentially one by one to recover the distribution of absorption coefficients for a specific transition. In ABNT, on the other hand, the projection data for all transitions are assembled into one sinogram and processed simultaneously in a single tomographic inversion. In other words, the sinogram for nonlinear tomography has higher dimensionality (i.e. spectral dimensions) than the classical case. Furthermore, in ABNT the distributions of temperature, species, and pressure are reconstructed directly without prior recovery of the spatial profiles of absorption coefficients. We point out also that the ABNT is not inherently limited in spatial resolution; it achieves the same level of spatial resolution as CAT for the same number of projections but, as mentioned earlier, enjoys better noise immunity. However, in cases with extremely limited optical access, ABNT provides useful data already from only two orthogonal projections, which is not possible with CAT.

Fig. 26 summarizes all the tomographic absorption techniques that have been either numerically or experimentally demonstrated, in terms of optimal sampling schemes. The sampling in spatial, temporal, and harmonic dimensions is represented by three axes, respectively. The distance along each axis indicates the intensiveness of the sampling in the corresponding dimension. As can be seen, CAT is in the plane z-O-x and samples the spatial dimension intensively at only one specific absorption transition. With the aid of nonlinear tomography, the sampling in the other two dimensions can be accommodated in the inversion process. For example, DAS-based nonlinear tomography can effectively take advantage of the spectral sampling and CFWMS-based nonlinear tomography further extends the tomographic sampling into the harmonic domain, using the wavelength modulation method.

To summarize, this paper has reviewed the definition, mathematical formulation, inversion algorithms, and experimental demonstrations as well as applications of both CAT and ABNT for practical flow tomography. Tomographic absorption spectroscopy is complementary to planar imaging techniques and has been experimentally demonstrated with minimal optical access for engine measurements. Recent progress in ABNT is set to extend the applicability of CAT to more difficult combustion scenarios, such as coal-fired power plant boilers filled with flying ashes and in-flight engine monitoring in the presence of severe vibration, etc. We note though, that ABNT is still in its early days and work has so far been mostly theoretical in nature. Important topics such as spatial resolution and sensitivity offer scope for future numerical and experimental investigation. However, the many potential advantages of the technique hold great promise for the future and we hope that this review serves as a pointer into new directions along which the field will develop. Full scale experimental demonstrations and practical applications are bound to follow in the near future. In addition, the theory of nonlinear tomography is a new mathematical approach for data processing quite generally, which can potentially be applied to other tomographic areas, such as ultrasonic tomography [317], electrical resistance tomography [318], electrical impedance tomography [26], and interferometric tomography [319]. Finally, we point out again that tomographic absorption spectroscopy quite generally, whether linear or not, is not limited to reconstructions in 2 dimensions. There are interesting new developments in so called imaging Fourier transform spectroscopy [320] which may enable volumetric absorption tomography in the future and proof of concept numerical studies are being conducted to explore the viability of this concept [108].

Acknowledgements

This work was funded by the European Commission under Grant No. ASHTCSC 330840 and also the Chinese Government 'Thousand Youth Talent Program'. Clemens F. Kaminski also wishes to acknowledge the Engineering and Physical Sciences Research Council (EPSRC) for funding (Grant EP/L015889/1).

References

[1] Hansen N, Cool TA, Westmoreland PR, Kohse-Höinghaus K. Recent contributions of flame-sampling molecular-beam mass spectrometry to a fundamental understanding of combustion chemistry. Prog Energ Combust 2009;35(2):168–91.
[2] Law CK. Combustion physics. Cambridge, U.K.: Cambridge University Press; 2006.
[3] Wolfrum J, Dreier T, Ebert V, Schulz C. Laser-based combustion diagnostics. Encyclopedia Anal Chem 2000: 2118–48.
[4] Ballester J, García-Armingol T. Diagnostic techniques for the monitoring and control of practical flames. Prog Energ Combust 2010;36(4):375–411.
[5] El-Mahallawy F, Habik E. Fundamentals and technology of combustion. Amsterdam, Netherland: Elsevier; 2002.
[6] Williams B, Edwards M, Stone R, Williams J, Ewart P. High precision in-cylinder gas thermometry using laser induced gratings: quantitative measurement of evaporative cooling with gasoline/alcohol blends in a GDI optical engine. Combust Flame 2014;161(1):270–9.
[7] Roy S, Gord JR, Patnaik AK. Recent advances in coherent anti-Stokes Raman scattering spectroscopy: fundamental developments and applications in reacting flows. Prog Energ Combust 2010;36(2):280–306.
[8] Weikl MC, Beyrau F, Leipertz A. Simultaneous temperature and exhaust-gas recirculation-measurements in a homogeneous charge-compression ignition engine by use of pure rotational coherent anti-Stokes Raman spectroscopy. Appl Optics 2006;45(15):3646–51.
[9] Kaminski CF, Ewart P. Multiplex H_2 coherent anti-Stokes Raman scattering thermometry with a modeless laser. Appl Optics 1997;36(3):731–4.
[10] Steuwe C, Kaminski CF, Baumberg JJ, Mahajan S. Surface enhanced coherent anti-Stokes Raman scattering on nanostructured gold surfaces. Nano Lett 2011;11(12):5339–43.

[11] Engström J, Nygren J, Aldén M, Kaminski CF. Two-line atomic fluorescence as a temperature probe for highly sooting flames. Opt Lett 2000;25(19):1469–71.
[12] Hult J, Burns IS, Kaminski CF. Two-line atomic fluorescence flame thermometry using diode lasers. P Combust Inst 2005;30(1):1535–43.
[13] Burns IS, Hult J, Hartung G, Kaminski CF. A thermometry technique based on atomic lineshapes using diode laser LIF in flames. P Combust Inst 2007;31(1):775–82.
[14] Burns IS, Lamoureux N, Kaminski CF, Hult J, Desgroux P. Diode laser atomic fluorescence temperature measurements in low-pressure flames. Appl Phys B 2008;93(4):907–14.
[15] Chrystie RSM, Burns IS, Johan H, Kaminski CF. High-repetition-rate combustion thermometry with two-line atomic fluorescence excited by diode lasers. Opt Lett 2009;34(16):2492–4.
[16] Burns IS, Mercier X, Wartel M, Chrystie RSM, Hult J, Kaminski CF. A method for performing high accuracy temperature measurements in low-pressure sooting flames using two-line atomic fluorescence. P Combust Inst 2011;33(1):799–806.
[17] Lyn DA, Einav S, Rodi W, Park J. A laser-Doppler velocimetry study of ensemble-averaged characteristics of the turbulent near wake of a square cylinder. J Fluid Mech 1995;304(12):285–319.
[18] Sislian JP, Jiang L, Cusworth R. Laser Doppler velocimetry investigation of the turbulence structure of axisymmetric diffusion flames. Prog Energ Combust 1988;14(2):99–146.
[19] Allen MG. Diode laser absorption sensors for gas-dynamic and combustion flows. Meas Sci Technol 1998;9(4):545.
[20] Li F, Yu X, Cai W, Ma L. Uncertainty in velocity measurement based on diode-laser absorption in nonuniform flows. Appl Optics 2012;51(20):4788–97.
[21] Sun K, Wang S, Sur R, Chao X, Jeffries JB, Hanson RK. Time-resolved in situ detection of CO in a shock tube using cavity-enhanced absorption spectroscopy with a quantum-cascade laser near 4.6 μm. Opt Express 2014;22(20):24559–65.
[22] Laurila T, Burns I, Hult J, Miller J, Kaminski C. A calibration method for broad-bandwidth cavity enhanced absorption spectroscopy performed with super-continuum radiation. Appl Phys B 2011;102(2):271–8.
[23] Bernhardt B, Ozawa A, Jacquet P, Jacquey M, Kobayashi Y, Udem T, Holzwarth R, Guelachvili G, Hänsch TW, Picqué N. Cavity-enhanced dual-comb spectroscopy. Nat Photonics 2010;4(1):55–7.
[24] Watt RS, Laurila T, Kaminski CF, Hult J. Cavity enhanced spectroscopy of high-temperature H2O in the near-infrared using a supercontinuum light source. Appl Spectrosc 2009;63(12):1389–95.
[25] Langridge J, Laurila T, Watt R, Jones R, Kaminski C, Hult J. Cavity enhanced absorption spectroscopy of multiple trace gas species using a supercontinuum radiation source. Opt. Express 2008;16(14):10178–88.
[26] Evertsen R, Staicu A, Dam N, Van Vliet A, Ter Meulen J. Pulsed cavity ring-down spectroscopy of NO and NO_2 in the exhaust of a diesel engine. Appl Phys B 2002;74(4-5):465–8.
[27] Kaynaroglu B, Tuncer O. Resolving turbulent flame front from Mie scattering measurements. J Therm Sci Tech 2015;35(1):21–6.
[28] Hoffman D, Münch KU, Leipertz A. Two-dimensional temperature determination in sooting flames by filtered Rayleigh scattering. Opt Lett 1996;21(7):525–7.
[29] Abram C, Fond B, Heyes AL, Beyrau F. High-speed planar thermometry and velocimetry using thermographic phosphor particles. Appl Phys B 2013: 1–6.
[30] Cho KY, Satija A, Pourpoint TL, Son SF, Lucht RP. Time-resolved 3D OH planar laser-induced fluorescence system for multiphase combustion. 8th U.S. national combustion meeting; 2013.
[31] Rensberger KJ, Jeffries JB, Copeland RA, Kohse-Höinghaus K, Wise ML, Crosley DR. Laser-induced fluorescence determination of temperatures in low pressure flames. Appl Optics 1989;28(17):3556–66.
[32] Luong M, Zhang R, Schulz C, Sick V. Toluene laser-induced fluorescence for in-cylinder temperature imaging in internal combustion engines. Appl Phys B 2008;91(3-4):669–75.
[33] Itani L, Bruneaux G, Lella A, Schulz C. Two-tracer LIF imaging of preferential evaporation of multi-component gasoline fuel sprays under engine conditions. P Combust Inst 2015;35(3):2915–22.
[34] Cho KY, Satija A, Pourpoint TL, Son SF, Lucht RP. High-repetition-rate three-dimensional OH imaging using scanned planar laser-induced fluorescence system for multiphase combustion. Appl Optics 2014;53(3):316–26.
[35] Keane R, Adrian R, Zhang Y. Super-resolution particle imaging velocimetry. Meas Sci Technol 1995;6(6):754.
[36] Charogiannis A, Beyrau F. Laser induced phosphorescence imaging for the investigation of evaporating liquid flows. Exp Fluids 2013;54(5):1–15.
[37] Fuhrmann N, Brübach J, Dreizler A. Phosphor thermometry: a comparison of the luminescence lifetime and the intensity ratio approach. P Combust Inst 2012.
[38] Brübach J, Pflitsch C, Dreizler A, Atakan B. On surface temperature measurements with thermographic phosphors: a review. Prog Energ Combust 2013;39(1):37–60.
[39] Nygren J, Hult J, Richter M, Aldén M, Christensen M, Hultqvist A, Johansson B. Three-dimensional laser induced fluorescence of fuel distributions in an HCCI engine. P Combust Inst 2002;29(1):679–85.
[40] Roberts PJ, Tian X, Jung Y. Application of three-dimensional laser-induced fluorescence to thermal diffusers. Hydraulic measurements and experimental methods specialty conference; 2002.
[41] Schulz C, Sick V. Tracer-LIF diagnostics: quantitative measurement of fuel concentration, temperature and fuel/air ratio in practical combustion systems. Prog Energ Combust 2005;31(1):75–121.
[42] Gessenhardt C, Schulz C, Kaiser SA. Endoscopic temperature imaging in a four-cylinder IC engine via two-color toluene fluorescence. P Combust Inst 2014;35(3):3697–705.
[43] Feroughi OM, Kronemayer H, Dreier T, Schulz C. Effect of fluctuations on time-averaged multi-line NO-LIF thermometry measurements of the gas-phase temperature. Appl Phys B 2015;120(3):429–40.
[44] Hecht C, Abdali A, Dreier T, Schulz C. Gas-temperature imaging in a microwave-plasma nanoparticle-synthesis reactor using multi-line NO-LIF thermometry. Z Phys Chem 2011;225(11-12):1225–35.
[45] Boxx I, Arndt CM, Carter CD, Meier W. High-speed laser diagnostics for the study of flame dynamics in a lean premixed gas turbine model combustor. Exp Fluids 2012;52(3):555–67.
[46] Panda PP, Roa M, Slabaugh CD, Peltier S, Carter CD, Laster WR, Lucht RP. High-repetition-rate planar measurements in the wake of a reacting jet injected into a swirling vitiated crossflow. Combust Flame 2016;163:241–57.
[47] Ma L, Lei Q, Wu Y, Xu W, Ombrello TM, Carter CD. From ignition to stable combustion in a cavity flameholder studied via 3D tomographic chemiluminescence at 20 kHz. Combust Flame 2016;165:1–10.
[48] Coriton B, Frank JH, Gomez A. Effects of strain rate, turbulence, reactant stoichiometry and heat losses on the interaction of turbulent premixed flames with stoichiometric counterflowing combustion products. Combust Flame 2013;160(11):2442–56.
[49] Coriton B, Steinberg AM, Frank JH. High-speed tomographic PIV and OH PLIF measurements in turbulent reactive flows. Exp Fluids 2014;55(6):1–20.
[50] Sutton JA, Driscoll JF. Measurements and statistics of mixture fraction and scalar dissipation rates in turbulent non-premixed jet flames. Combust Flame 2013;160(9):1767–78.
[51] Soulopoulos N, Hardalupas Y, Taylor AMKP. Mixing and scalar dissipation rate statistics in a starting gas jet. Phys Fluids 2015;27(12):125103.
[52] Gordon RL, Heeger C, Dreizler A. High-speed mixture fraction imaging. Appl Phys B 2009;96(4):745–8.
[53] Kaminski CF, Engström J, Aldén M. Quasi-instantaneous two-dimensional temperature measurements in a spark ignition engine using 2-line atomic fluorescence. Int Sym Combust 1998;27(1):85–93.
[54] Nygren J, Engström J, Walewski J, Kaminski CF, Aldén M. Applications and evaluation of two-line atomic LIF thermometry in sooting combustion environments. Meas Sci Technol 2001;12(8):1294–303.
[55] Medwell PR, Masri AR, Pham PX, Dally BB, Nathan GJ. Temperature imaging of turbulent dilute spray flames using two-line atomic fluorescence. Exp Fluids 2014(11):1–11.
[56] Dworkin S, Schaffer A, Connelly B, Long M, Smooke M, Puccio M, McAndrew B, Miller J. Measurements and calculations of formaldehyde concentrations in a methane/N_2/air, non-premixed flame: Implications for heat release rate. P Combust Inst 2009;32(1):1311–8.
[57] Balachandran R, Ayoola B, Kaminski C, Dowling A, Mastorakos E. Experimental investigation of the nonlinear response of turbulent premixed flames to imposed inlet velocity oscillations. Combust Flame 2005;143(1):37–55.
[58] Ayoola B, Balachandran R, Frank J, Mastorakos E, Kaminski C. Spatially resolved heat release rate measurements in turbulent premixed flames. Combust Flame 2006;144(1):1–16.
[59] Armitage CA, Balachandran R, Mastorakos E, Cant RS. Investigation of the non-linear response of turbulent premixed flames to imposed inlet velocity oscillations. Combust Flame 2006;146(3):419–36.
[60] Hsu PS, Jiang N, Gord JR, Roy S. Fiber-coupled, 10 kHz simultaneous OH planar laser-induced fluorescence/particle-image velocimetry. Opt Lett 2013;38(2):130–2.
[61] Miller VA, Troutman VA, Mungal MG, Hanson RK. 20 kHz toluene planar laser-induced fluorescence imaging of a jet in nearly sonic crossflow. Appl Phys B 2014;117(1):401–10.
[62] Jiang N, Patton RA, Lempert WR, Sutton JA. Development of high-repetition rate CH PLIF imaging in turbulent nonpremixed flames. P Combust Inst 2011;33(1):767–74.
[63] Wellander R, Richter M, Alden M. Time resolved, 3D imaging (4D) of two phase flow at a repetition rate of 1 kHz. Opt Express 2011;19(22):21508–14.
[64] Hult J, Meier U, Meier W, Harvey A, Kaminski C. Experimental analysis of local flame extinction in a turbulent jet diffusion flame by high repetition 2-D laser techniques and multi-scalar measurements. P Combust Inst 2005;30(1):701–9.
[65] Kaminski C, Hult J, Aldén M. High repetition rate planar laser induced fluorescence of OH in a turbulent non-premixed flame. Appl Phys B 1999;68(4):757–60.
[66] Jiang N, Webster M, Nishihara M, Lempert WR. 500 kHz frame rate nitric oxide planar laser induced fluorescence imaging. AIAA aerospace sciences meeting including the new horizons forum and aerospace exposition; 2009.
[67] Zhou B, Brackmann C, Li Z, Aldén M. Development and application of CN PLIF for single-shot imaging in turbulent flames. Combust Flame 2015;162(2):368–74.
[68] Zhou B, Li Q, He Y, Petersson P, Li Z, Aldén M, Bai X. Visualization of multi-regime turbulent combustion in swirl-stabilized lean premixed flames. Combust Flame 2015;162(7):2954–8.
[69] Wellander R, Richter M, Aldén M. Time-resolved (kHz) 3D imaging of OH PLIF in a flame. Exp Fluids 2014;55(6):1–12.
[70] Weinkauff J, Greifenstein M, Dreizler A, Böhm B. Time resolved three-dimensional flamebase imaging of a lifted jet flame by laser scanning. Meas Sci Technol 2015;26(10):105201.

[71] Köser J, Becker L, Vorobiev N, Schiemann M, Scherer V, Böhm B, Dreizler A. Characterization of single coal particle combustion within oxygen-enriched environments using high-speed OH-PLIF. Appl Phys B 2015;121(4):459–64.
[72] Peterson B, Baum E, Böhm B, Dreizler A. Early flame propagation in a spark-ignition engine measured with quasi 4D-diagnostics. P Combust Inst 2015;35(3):3829–37.
[73] Weinkauff J, Trunk P, Frank J, Dunn M, Dreizler A, Böhm B. Investigation of flame propagation in a partially premixed jet by high-speed-Stereo-PIV and acetone-PLIF. P Combust Inst 2015;35(3):3773–81.
[74] Peterson B, Baum E, Böhm B, Sick V, Dreizler A. High-speed PIV and LIF imaging of temperature stratification in an internal combustion engine. P Combust Inst 2013;34(2):3653–60.
[75] Jainski C, Lu L, Sick V, Dreizler A. Laser imaging investigation of transient heat transfer processes in turbulent nitrogen jets impinging on a heated wall. Int J Heat Mass Tran 2014;74:101–12.
[76] Sick V. High speed imaging in fundamental and applied combustion research. P Combust Inst 2013;34(2):3509–30.
[77] Herman CT. Image reconstructions from projections – the fundamentals of computerized tomography. 2nd ed. New York, USA: Academic Press; 2010.
[78] Elsinga GE. Tomographic particle image velocimetry and its application to turbulent boundary layers. J Aerospace Eng 2008.
[79] Hain R, Kähler CJ, Michaelis D. Tomographic and time resolved PIV measurements on a finite cylinder mounted on a flat plate. Exp Fluids 2008;45(4):715–24.
[80] Halls BR, Heindel TJ, Kastengren AL, Meyer TR. Evaluation of X-ray sources for quantitative two-and three-dimensional imaging of liquid mass distribution in atomizing sprays. Int J Multiphas Flow 2014;59:113–20.
[81] Linne M. Imaging in the optically dense regions of a spray: a review of developing techniques. Prog Energ Combust 2013;39(5):403–40.
[82] Floyd J, Geipel P, Kempf AM. Computed tomography of chemiluminescence (CTC): instantaneous 3D measurements and phantom studies of a turbulent opposed jet flame. Combust Flame 2011;158(2):376–91.
[83] Cai W, Li X, Ma L. Numerical and experimental validation of a three-dimensional combustion diagnostic based on tomographic chemiluminescence. Opt Express 2013;21(6):7050–64.
[84] Wang J, Song Y, Li ZH, Kempf A, He AZ. Multi-directional 3D flame chemiluminescence tomography based on lens imaging. Opt Lett 2015;40(7):1231–4.
[85] Sun N, Song Y, Wang J, Li Z, He A. Volume moiré tomography based on double cross gratings for real three-dimensional flow field diagnosis. Appl Optics 2012;51(34):8081–9.
[86] Faris GW, Byer RL. Beam-deflection optical tomography of a flame. Opt Lett 1987;12(3):155–7.
[87] Chen Y, Zheng G, Yu Y, Gu F. Diagnosis of arc plasma jet flowing into air by integrating moiré and emission tomography. Opt Commun 2014;315:183–7.
[88] Wang J, Song Y, Li Z, He A. Realization of volume optical computerized tomography by circular gratings. Opt-Int J Light Electron Optics 2013;124(22):5822–5.
[89] Chen Y, Wang J, Wang Q, Li Z. Integrating moiré and emission tomography to visualize and diagnose high-temperature flow fields. Opt Lett 2012;37(13):2721–3.
[90] Shakher C, Daniel A. Talbot interferometer with circular gratings for the measurement of temperature in axisymmetric gaseous flames. Appl Optics 1994;33(25):6068–72.
[91] Agrawal AK, Butuk NK, Gollahalli SR, Griffin D. Three-dimensional rainbow schlieren tomography of a temperature field in gas flows. Appl Optics 1998;37(3):479–85.
[92] Stella A, Guj G, Giammartini S. Measurement of axisymmetric temperature fields using reference beam and shearing interferometry for application to flames. Exp Fluids 2000;29(1):1–12.
[93] Singh P, Faridi MS, Shakher C. Measurement of temperature of an axisymmetric flame using shearing interferometry and Fourier fringe analysis technique. Opt Eng 2004;43(2):387–92.
[94] Sharma S, Sheoran G, Shakher C. Investigation of temperature and temperature profile in axi-symmetric flame of butane torch burner using digital holographic interferometry. Opt Laser Eng 2012;50(10):1436–44.
[95] Sharma S, Sheoran G, Vyas A, Shakher C. Measurement of temperature of an axi-symmetric flame of butane torch burner using digital holographic interferometry. Optical instrumentation for energy and environmental applications; 2012.
[96] Tankam P, Song Q, Karray M, Li J, Michel Desse J, Picart P. Real-time three-sensitivity measurements based on three-color digital Fresnel holographic interferometry. Opt Lett 2010;35(12):2055–7.
[97] Doleček R, Psota P, Lédl V, Vít T, Václavík J, Kopecký V. General temperature field measurement by digital holography. Appl Optics 2013;52(1):A319–25.
[98] Wang F, Wu Q, Huang Q, Zhang H, Yan J, Cen K. Simultaneous measurement of 2-dimensional H_2O concentration and temperature distribution in premixed methane/air flame using TDLAS-based tomography technology. Opt Commun 2015;346:53–63.
[99] 洪延姬, 燃烧场吸收光谱诊断技术研究进展. 实验流体力学, (2014) 28(3): p. 12–25.
[100] Scarano F. Tomographic PIV: principles and practice. Meas Sci Technol 2013;24(1):012001.
[101] Elsinga G, Scarano F, Wieneke B, Van Oudheusden B. Tomographic particle image velocimetry. Exp Fluids 2006;41(6):933–47.
[102] Adrian RJ. Twenty years of particle image velocimetry. Exp Fluids 2005;39(2):159–69.
[103] Elsinga GE, Wieneke B, Scarano F, Schröder A. Tomographic 3D-PIV and applications. Particle image velocimetry. Springer; 2008. p. 103–25.
[104] Adrian RJ, Westerweel J. Particle image velocimetry. Cambridge, U.K.: Cambridge University Press; 2010.
[105] Herman GT. Image reconstruction from projections. Real-Time Imaging 1995;1(1):3–18.
[106] Floyd J, Kempf A. Computed tomography of chemiluminescence (CTC): high resolution and instantaneous 3-D measurements of a matrix burner. P Combust Inst 2011;33(1):751–8.
[107] Floyd J, Heyes A, Kempf A. Computed tomography of chemiluminescence (CTC): instantaneous measurements of a matrix burner. In: Proceedings of the 4th European combustion meeting; 2009.
[108] Cai W, Kaminski CF. A numerical investigation of high-resolution multispectral absorption tomography for flow thermometry. Appl Phys B 2015;119(1):29–35.
[109] Wang Z, Anderson MH, Sanders ST. Polymer film-based optical access to enclosed gas: demonstration of H_2O absorption tomography. Appl Phys B 2016;122(9):1–4.
[110] Bertero M, Boccacci P. Introduction to inverse problems in imaging. Boca Raton, Florida, USA: CRC Press; 1998.
[111] Chapter 5 McCann H, Wright P, Daun K. Chemical species tomography Chapter 5 In: Wang M, editor. Industrial tomography: systems and applications. Cambridge, U.K.: Woodhead Publishing; 2015.
[112] Liu C, Xu L, Cao Z, Yang Y. Fan-beam TDLAS tomography for gas concentration distribution with limited data. Imaging systems and techniques (IST); 2012.
[113] Daun K. Infrared species limited data tomography through Tikhonov reconstruction. JQSRT 2010;111(1):105–15.
[114] Wright P, Terzija N, Davidson JL, Garcia-Castillo S, Garcia-Stewart C, Pegrum S, Colbourne S, Turner P, Crossley SD, Litt T. High-speed chemical species tomography in a multi-cylinder automotive engine. Chem Eng J 2010;158(1):2–10.
[115] Li H, Rieker GB, Liu X, Jeffries JB, Hanson RK. Extension of wavelength-modulation spectroscopy to large modulation depth for diode laser absorption measurements in high-pressure gases. Appl Opt 2006;45(5):1052–61.
[116] Guha A, Schoegl I. Tomographic laser absorption spectroscopy using Tikhonov regularization. Appl Optics 2014;53(34):8095–103.
[117] Cai W, Kaminski CF. A tomographic technique for the simultaneous imaging of temperature, chemical species, and pressure in reactive flows using absorption spectroscopy with frequency-agile lasers. Appl Phys Lett 2014;104(3):034101.
[118] Cai W, Kaminski CF. Multiplexed absorption tomography with calibration-free wavelength modulation spectroscopy. Appl Phys Lett 2014;104(16):154106.
[119] Ma L, Cai W, Caswell AW, Kraetschmer T, Sanders ST, Roy S, Gord JR. Tomographic imaging of temperature and chemical species based on hyperspectral absorption spectroscopy. Optics Express 2009;17(10):8602–13.
[120] Ma L, Cai W. Numerical investigation of hyperspectral tomography for simultaneous temperature and concentration imaging. Appl Optics 2008;47(21):3751–9.
[121] Cai W, Ewing DJ, Ma L. Application of simulated annealing for multispectral tomography. Comput Phys Commun 2008;179(4):250–5.
[122] Yiguang J. Recent progress and challenges in fundamental combustion research. Prog Mech 2014;44:201402.
[123] Zhang Z, Sun P, Pang T, Xia H, Cui X, Li Z, Han L, Wu B, Wang Y, Sigrist MW. Reconstruction of combustion temperature and gas concentration distributions using line-of-sight tunable diode laser absorption spectroscopy. Opt Eng 2016;55(7):076107.
[124] Xia H, Kan R, Liu J, Xu Z, He Y. Analysis of algebraic reconstruction technique for accurate imaging of gas temperature and concentration based on tunable diode laser absorption spectroscopy. Chin Phys B 2016;25(6):064205.
[125] Tsekenis S, Wilson D, Lengden M, Hyvönen J, Leinonen J, Shah A, Andersson Ö, McCann H. Towards in-cylinder chemical species tomography on large-bore IC engines with pre-chamber. Flow Meas Instrum 2016.
[126] Polydorides N, Tsekenis S-A, McCann H, Prat V-D, Wright P. An efficient approach for limited-data chemical species tomography and its error bounds. In: Proc R Soc A; 2016.
[127] Daun KJ, Grauer SJ, Hadwin PJ. Chemical species tomography of turbulent flows: discrete ill-posed and rank deficient problems and the use of prior information. JQSRT 2016;172:58–74.
[128] Busa KM, Rice BE, McDaniel JC, Goyne CP, Rockwell RD, Fulton JA, Edwards JR, Diskin GS. Scramjet combustion efficiency measurement via tomographic absorption spectroscopy and particle image velocimetry. AIAA J 2016: 2463–71.
[129] Emmerman P, Goulard R, Santoro R, Semerjian H. Multiangular absorption diagnostics of a turbulent argon-methane jet. J Energy 1980;4(2):70–7.
[130] Cai W, Li X, Ma L. Practical aspects of implementing 3D tomography inversion for volumetric flame imaging. Appl Optics 2013;52(33):8106–16.
[131] Edwards JL, Gouldin FC, Becz S. Gas turbine engine combustor control using emission tomography. In: 44th AIAA aerospace sciences meeting and exhibit; 2006.
[132] Ishino Y, Ohiwa N. Three-dimensional computerized tomographic reconstruction of instantaneous distribution of chemiluminescence of a turbulent premixed flame. JSME Int J 2005;48(1):34–40.
[133] Leipertz A, Obertacke R, Wintrich F. Industrial combustion control using UV emission tomography. Symposium on combustion, 26; 1996. p. 2869–75.
[134] Philipp H, Plimon A, Fernitz G, Hirsch A, Fraidl G, Winklhofer E. A tomographic camera system for combustion diagnostics in SI engines. International congress & exposition; 1995.
[135] Hertz H, Faris G. Emission tomography of flame radicals. Opt Lett 1988;13(5):351–3.

[136] Anikin NB, Suntz R, Bockhorn H. Tomographic reconstruction of 2D-OH*-chemiluminescence distributions in turbulent diffusion flames. Appl Phys B 2013;107(3):591–602.
[137] Lv L, Tan J, Hu Y. Numerical and experimental investigation of computed tomography of chemiluminescence for hydrogen-air premixed laminar flames. Int J Aerospace Eng 2016.
[138] Uchiyama H, Nakajima M, Yuta S. Measurement of flame temperature distribution by IR emission computed tomography. Appl Optics 1985;24(23):4111–6.
[139] Halls BR, Thul DJ, Michaelis D, Roy S, Meyer TR, Gord JR. Single-shot, volumetrically illuminated, three-dimensional, tomographic laser-induced-fluorescence imaging in a gaseous free jet. Opt Express 2016;24(9):10040–9.
[140] Ma L, Lei Q, Ikeda J, Xu W, Wu Y, Carter CD. Single-shot 3D flame diagnostic based on volumetric laser induced fluorescence (VLIF). P Combust Inst 2016.
[141] Wu Y, Xu W, Lei Q, Ma L. Single-shot volumetric laser induced fluorescence (VLIF) measurements in turbulent flows seeded with iodine. Opt Express 2015;23(26).
[142] Elsinga GESF, Wieneke B, Oudheusden BW. Assessment of Tomo-PIV for three-dimensional flows. In: 6th international symposium on PIV; 2005.
[143] Ebi D, Clemens NT. Simultaneous high-speed 3D flame front detection and tomographic PIV. Meas Sci Technol 2016;27(3):035303.
[144] Irandoost MS, Ashjaee M, Askari MH, Ahmadi S. Temperature measurement of axisymmetric partially premixed methane/air flame in a co-annular burner using Mach–Zehnder interferometry. Opt Laser Eng 2015;74:94–102.
[145] Zhang B, Zhao M, Liu Z, Wu Z. Flame four-dimensional deflection tomography with compressed-sensing-revision reconstruction. Opt Laser Eng 2016;83:23–31.
[146] Keren E, Bar-Ziv E, Glatt I, Kafri O. Measurements of temperature distribution of flames by moire deflectometry. Appl Optics 1981;20(24):4263–6.
[147] Cai W, Powell CF, Yue Y, Narayanan S, Wang J, Tate MW, Renzi MJ, Ercan A, Fontes E, Gruner SM. Quantitative analysis of highly transient fuel sprays by time-resolved X-radiography. Appl Phys Lett 2003;83(8):1671–3.
[148] Marchitto L, Hampai D, Dabagov SB, Allocca L, Alfuso S, Polese C, Liedl A. GDI spray structure analysis by polycapillary X-ray -tomography. Int J Multiphas Flow 2015;70:15–21.
[149] Liu X, Im KS, Wang Y, Wang J, Tate MW, Ercan A, Schuette DR, Gruner SM. Four dimensional visualization of highly transient fuel sprays by microsecond quantitative x-ray tomography. Appl Phys Lett 2009;94(8):084101–084101-3.
[150] Wang J. Ultrafast X-ray imaging of fuel sprays. Ninth international conference on synchrotron radiation instrumentation; 2007.
[151] Kristensson E, Berrocal E, Aldén M. Quantitative 3D imaging of scattering media using structured illumination and computed tomography. Opt Express 2012;20(13):14437–50.
[152] Ginat DT, Gupta R. Advances in computed tomography imaging technology. Annu Rev Biomed Eng 2014;16:431–53.
[153] Williams RA, Beck MS. Process tomography : principles, techniques and applications. Oxford: Butterworth-Heinemann; 1995.
[154] Chen F, Goulard R. Retrieval of arbitrary concentration and temperature fields by multiangular scanning techniques. JQSRT 1976;16(10):819–27.
[155] Wright P, Garcia-Stewart CA, Carey SJ, Hindle FP, Pegrum SH, Colbourne SM, Turner PJ, Hurr WJ, Litt TJ, Murray SC, Crossley SD, Ozanyan KB, McCann H. Toward in-cylinder absorption tomography in a production engine. Appl Optics 2005;44(31):6578–92.
[156] Terzija N, Karagiannopoulos S, Begg S, Wright P, Ozanyan KB, Mccann H. Tomographic imaging of the liquid and vapour fuel distributions in a single-cylinder direct injection gasoline engine. Int J Engine Res 2015;16(4):565–79.
[157] Guha A, Schoegl I. Tomographic imaging of flames: assessment of reconstruction error based on simulated results. J Propul Power 2014;30(2):350–9.
[158] Åkesson EO, Daun KJ. Parameter selection methods for axisymmetric flame tomography through Tikhonov regularization. Appl Optics 2008;47(3):407–16.
[159] Ravichandran M, Gouldin F. Determination of temperature and concentration profiles using (a limited number of) absorption measurements. Combust Sci Technol 1986;45(1-2):47–64.
[160] Hughey B, Santavicca DA. A comparison of techniques for reconstructing axisymmetric reacting flow fields from absorption measurements. Combust Sci Technol 1982;29(3-6):167–90.
[161] Thorpe MJ, Adler F, Cossel KC, de Miranda MH, Ye J. Tomography of a supersonically cooled molecular jet using cavity-enhanced direct frequency comb spectroscopy. Chem Phys Lett 2009;468(1):1–8.
[162] Dahm WJ, Chen S, Silver JA, Mullin JA, Piltch ND. Mixture fraction measurements via WMS-ITAC in a microgravity vortex ring diffusion flame. P Combust Inst 2002;29(2):2519–26.
[163] Silver JA, Kane DJ, Greenberg PS. Quantitative species measurements in microgravity flames with near-IR diode lasers. Appl Optics 1995;34(15):2787–801.
[164] McNesby K, Daniel R, Morris J, Miziolek A. Tomographic analysis of CO absorption in a low-pressure flame. Appl Optics 1995;34(18):3318–24.
[165] Ouyang X, Varghese PL, Howell JR. Tomographic absorption spectroscopy of combustion gases using tunable infrared diode lasers. OE/LASE'92; 1992.
[166] Dasch CJ. One-dimensional tomography: a comparison of Abel, onion-peeling, and filtered backprojection methods. Appl Optics 1992;31(8):1146–52.
[167] Wei Y, Wang G, Jiang H. Relation between the filtered backprojection algorithm and the backprojection algorithm in CT. IEEE Signal Proc Let 2005;12(9):633–6.
[168] Herman GT, Lent A, Rowland SW. ART: mathematics and applications: a report on the mathematical foundations and on the applicability to real data of the algebraic reconstruction techniques. J Theor Biol 1973;42(1):1–32.
[169] Terzija N, Davidson J, Garcia-Stewart C, Wright P, Ozanyan K, Pegrum S, Litt T, McCann H. Image optimization for chemical species tomography with an irregular and sparse beam array. Meas Sci Technol 2008;19:094007.
[170] Chung KB, Gouldin FC, Wolga GJ. Experimental reconstruction of the spatial density distribution of a nonreacting flow with a small number of absorption measurements. Appl Optics 1995;34(24):5492–500.
[171] Edwards J, Gouldin F, MacDonald M. High speed absorption tomography with advanced reconstruction algorithms. 41st aerospace sciences meeting and exhibit; 2003.
[172] Twynstra MG, Daun KJ, Waslander SL. Line-of-sight-attenuation chemical species tomography through the level set method. JQSRT 2014;143:25–34.
[173] Johansson M, Galle B, Rivera C, Zhang Y. Tomographic reconstruction of gas plumes using scanning DOAS. B Volcanol 2009;71(10):1169–78.
[174] Martin EF, Goyne CP, Diskin GS. Development of a tomography technique for a scramjet wind tunnel. Int J Hypersonics 2010;1(3):173–80.
[175] Wondraczek L, Khorsandi A, Willer U, Heide G, Schade W, Frischat GH. Mid-infrared laser-tomographic imaging of carbon monoxide in laminar flames by difference frequency generation. Combust Flame 2004;138(1):30–9.
[176] Xia H, Xu Z, Kan R, He Y, Liu J, Zhang G. Numerical study of two-dimensional water vapor concentration and temperature distribution of combustion zones using tunable diode laser absorption tomography. Infrared Phys Techn 2015;72:170–8.
[177] Terzija N, McCann H. Wavelet-based image reconstruction for hard-field tomography with severely limited data. Sensors J IEEE 2011;11(9):1885–93.
[178] Busa KM, Ellison EN, McGovern BJ, McDaniel JC, Diskin GS, DePiro MJ, Capriotti DP, Gaffney RL. Measurements on NASA langley durable combustor rig by TDLAT: preliminary results. 51st AIAA aerospace sciences meeting including the new horizons forum and aerospace exposition; 2013.
[179] Busa KM, Bryner E, McDaniel JC, Goyne CP, Smith CT, Diskin GS. Demonstration of capability of water flux measurement in a scramjet combustor using tunable diode laser absorption tomography and stereoscopic PIV. 49th AIAA aerospace sciences meeting including the new horizons forum and aerospace exposition; 2011.
[180] Bryner E, Busa K, McDaniel JC, Goyne CP, Diskin GS. Spatially resolved temperature and water vapor concentration distributions in a flat Flame burner by tunable diode laser absorption tomography. 49th AIAA aerospace sciences meeting including the new horizons forum and aerospace exposition; 2011.
[181] Schleicher E, da Silva M, Thiele S, Li A, Wollrab E, Hampel U. Design of an optical tomograph for the investigation of single-and two-phase pipe flows. Meas Sci Technol 2008;19(9):094006.
[182] Mohamad EJ, Rahim RA, Ibrahim S, Sulaiman S, Manaf MS. Flame imaging using laser-based transmission tomography. Sensor Actuat A-Phys 2006;127(2):332–9.
[183] Rahim RA, Pang JF, Chan KS. Optical tomography sensor configuration using two orthogonal and two rectilinear projection arrays. Flow Meas Instrum 2005;16(5):327–40.
[184] Zhang FY, Fujiwara T, Komurasaki K. Diode-laser tomography for arcjet plume reconstruction. Appl Optics 2001;40(6):957–64.
[185] Zhang F, Fujiwara T, Komurasaki K, Miyasaka T, Harada J. Determination of parameters in arcjet plume by tomographic reconstruction. T Jpn Soc Aeronaut S 2000;43(140):77–87.
[186] Kawazoe H, Whitelaw J. Computer tomography of infra-red absorption and its application to internal-combustion engines. In: 10th international symposium on application of laser techniques to fluid mechanics; 2000.
[187] Baum RT, McGrattan KB, Nyden MR. An examination of the applicability of computed tomography for the measurement of component concentrations in fire-generated plumes. Combust Flame 1998;113(3):358–72.
[188] Bennett KE, Faris GW, Byer RL. Experimental optical fan beam tomography. Appl Optics 1984;23(16):2678–85.
[189] Guha A, Schoegl I. Simulation of 2D tomographic TDLAS using algebraic reconstruction and Tikhonov regularization. 8th US national combustion meeting; 2013.
[190] Li N, Weng C. Modified adaptive algebraic tomographic reconstruction of gas distribution from incomplete projection by a two-wavelength absorption scheme. Chin Opt Lett 2011;9(6):061201.
[191] Hartl A, Mettenorf K, Song B, Platt U, Pundt I. 2d tomographic reconstruction of trace gas distributions from long-path DOAS measurements: general approach, validation and outlook on an experiment on an urban site. Atmos Chem Phys 2009.
[192] Hartl A, Song B, Pundt I. 2-D reconstruction of atmospheric concentration peaks from horizontal long path DOAS tomographic measurements: parametrisation and geometry within a discrete approach. Atmos Chem Phys 2006;6(3):847–61.
[193] Song J, Hong Y, Wang G, Pan H. Algebraic tomographic reconstruction of two-dimensional gas temperature based on tunable diode laser absorption spectroscopy. Appl Phys B 2013: 1–9.
[194] Liu C, Xu L, Cao Z. Measurement of axisymmetric temperature distributions using single view fan-beam TDLAS tomography. Instrumentation and measurement technology conference (I2MTC); 2013.
[195] Kasyutich V, Martin P. Towards a two-dimensional concentration and temperature laser absorption tomography sensor system. Appl Phys B 2011;102(1):149–62.
[196] Wang F, Cen K, Li N, Jeffries JB, Huang Q, Yan J, Chi Y. Two-dimensional tomography for gas concentration and temperature distributions based on tunable diode laser absorption spectroscopy. Meas Sci Technol 2010;21(4):045301.

[197] Salem K, Tsotsas E, Mewes D. Tomographic measurement of breakthrough in a packed bed adsorber. Chem Eng Sci 2005;60(2):517–22.
[198] Gillet B, Hardalupas Y, Kavounides C, Taylor A. Infrared absorption for measurement of hydrocarbon concentration in fuel/air mixtures (MAST-B-LIQUID). Appl Therm Eng 2004;24(11-12):1633–53.
[199] McCann H, Carey SJ, Hindle FP, Ozanyan KB, Winterbone DE, Clough E. Near-infrared absorption tomography system for measurement of gaseous hydrocarbon distribution. Intelligent systems and smart manufacturing; 2001.
[200] Hindle FP, Carey SJ, Ozanyan K, Winterbone DE, Clough E, McCann H. Measurement of gaseous hydrocarbon distribution by a near-infrared absorption tomography system. J Electron Imaging 2001;10(3):593–600.
[201] Ravichandran M, Gouldin F. Reconstruction of smooth distributions from a limited number of projections. Appl Optics 1988;27(19):4084–97.
[202] Cai W, Ma L. Comparison of approaches based on optimization and algebraic iteration for binary tomography. Comput Phys Commun 2010;181(12):1974–81.
[203] Zhang L, Wang F, Zhang H, Yan J, Cen K. Simultaneous measurement of gas distribution in a premixed flame using adaptive algebraic reconstruction technique based on the absorption spectrum. Chin Opt Lett 2016;14(11):111201.
[204] Xia H, Kan R, Xu Z, He Y, Liu J, Chen B, Yang C, Yao L, Wei M, Zhang G. Two-step tomographic reconstructions of temperature and species concentration in a flame based on laser absorption measurements with a rotation platform. Opt Laser Eng 2017;90:10–8.
[205] Elfving T, Hansen PC, Nikazad T. Semi-convergence properties of Kaczmarz's method. Inverse Probl 2014;30(5).
[206] Natterer F. The mathematics of computerized tomography. New York, USA: John Wiley; 1986.
[207] Elfving T, Nikazad T, Hansen PC. Semi-convergence and relaxation parameters for a class of SIRT algorithms. El T Numer Anal 2010;37(37):321–36.
[208] Yang WQ, Spink DM, York TA, Mccann H. An image-reconstruction algorithm based on Landweber's iteration method for electrical-capacitance tomography. Meas Sci Technol 1999;10(11):1065–9.
[209] Wood MP, Ozanyan KB. Concentration and Temperature Tomography at Elevated Pressures. Sensors J IEEE 2012.
[210] Pal S, Ozanyan K, McCann H. A computational study of tomographic measurement of carbon monoxide at minor concentrations. Meas Sci Technol 2008;19:094018.
[211] Elfving T, Nikazad T. Stopping rules for Landweber-type iteration. Inverse Probl 2007;23(4):1417–32 1432.
[212] Busa KM, McDaniel JC, Brown MS, Diskin GS. Implementation of maximum-likelihood expectation-maximization algorithm for tomographic reconstruction of TDLAT measurements. 52nd aerospace sciences meeting; 2014.
[213] Verkruysse W, Todd LA. Novel algorithm for tomographic reconstruction of atmospheric chemicals with sparse sampling. Environ Sci Technol 2005;39(7):2247–54.
[214] Todd LA, Bhattacharyya R. Tomographic reconstruction of air pollutants: evaluation of measurement geometries. Appl Optics 1997;36(30):7678–88.
[215] Verkruysse W, Todd LA. Improved method "grid translation" for mapping environmental pollutants using a two-dimensional CAT scanning system. Atmos Environ 2004;38(12):1801–9.
[216] Kauranen P, Hertz HM, Svanberg S. Tomographic imaging of fluid flows by the use of two-tone frequency-modulation spectroscopy. Opt Lett 1994;19(18):1489–91.
[217] Worth NA, Dawson JR. Tomographic reconstruction of OH* chemiluminescence in two interacting turbulent flames. Meas Sci Technol 2013;24(2):024013.
[218] Chuang K, Jan M, Wu J, Lu J, Chen S, Hsu C, Fu Y. A maximum likelihood expectation maximization algorithm with thresholding. Comput Med Imag Grap 2005;29(7):571–8.
[219] Herman GT, Meyer LB. Algebraic reconstruction techniques can be made computationally efficient. Med Imaging IEEE Trans 1993;12(3):600–9.
[220] Torniainen ED, Hinz AK, Gouldin FC. Tomographic analysis of unsteady, reacting flows: numerical investigation. AIAA J 1998;36(7):1270–8.
[221] Torniainen E, Gouldin F. Tomographic reconstruction of 2-D absorption coefficient distributions from a limited set of infrared absorption data. Combust Sci Technol 1998;131(1-6):85–105.
[222] Chojnacki AM, Sarma A, Wolga GJ, Torniainen ED, Gouldin FC. Infrared tomographic inversion for combustion and incineration. Combust Sci Technol 1996: 583–606.
[223] Hansen PC. Rank-deficient and discrete ill-posed problems: numerical aspects of linear inversion. Philadelphia, USA: Society for Industrial and Applied Mathematics (SIAM) 491-491; 1999.
[224] Cheng J, Hofmann B. Regularization methods for ill-posed problems. Boca Raton, Florida, USA: CRC Press; 1993. p. 1–31.
[225] Grauer SJ, Hadwin PJ, Daun KJ. Bayesian approach to the design of chemical species tomography experiments. Appl Optics 2016;55(21):5772–82.
[226] Winklhofer E, Fraidl G, Plimon A. Monitoring of gasoline fuel distribution in a research engine. P I Mech Eng D-J Aut 1992;206(2):107–15.
[227] Santoro R, Semerjian H, Emmerman P, Goulard R. Optical tomography for flow field diagnostics. Int J Heat Mass Tran 1981;24(7):1139–50.
[228] Chojnacki AM, Wolga GJ, Gouldin FC. Infrared color center laser system for tomographic determination of temperature and species concentration distributions in combusting systems. Combust Sci Technol 1998: 165–81.
[229] Deguchi Y, Yasui D, Adachi A. Development of 2D temperature and concentration measurement method using tunable diode laser absorption spectroscopy. J Mech Eng Automat 2012;2:543–9.
[230] Pal S, McCann H. Auto-digital gain balancing: a new detection scheme for high-speed chemical species tomography of minor constituents. Meas Sci Technol 2011;22(11):115304.
[231] McCann H, Cheadle E, Davidson J, Ozanyan K, Terzija N, Wright P. In-cylinder chemical species tomography for CI engines. B Environ Contam Tox 2009;34(1):106–8.
[232] Lindstrom C, Tam CJ, Givens R, Davis D, Williams S. Diode laser absorption tomography using data compression techniques. Computational imaging VI; 2008.
[233] Hafiz R, Ozanyan KB. Digitally balanced detection for optical tomography. Rev Sci Instrum 2007;78(10):103101.
[234] Maddaloni P, Malara P, Gagliardi G, De Natale P. Two-tone frequency modulation spectroscopy for ambient-air trace gas detection using a portable difference-frequency source around 3 μm. Appl Phys B 2006;85(2-3):219–22.
[235] Villarreal R, Varghese PL. Frequency-resolved absorption tomography with tunable diode lasers. Appl Optics 2005;44(31):6786–95.
[236] Carey S, McCann H, Winterbone D, Clough E. Near infra-red absorption tomography for measurement of chemical species distribution. In: 1st world congress on industrial process tomography. . Greater Manchester; 1999.
[237] Beiting EJ. Fiber-optic fan-beam absorption tomography. Appl Optics 1992;31(9):1328–43.
[238] Carey SJ, McCann H, Hindle F, Ozanyan K, Winterbone D, Clough E. Chemical species tomography by near infra-red absorption. Chem Eng J 2000;77(1):111–8.
[239] Ma L, Li X, Sanders ST, Caswell AW, Roy S, Plemmons DH, Gord JR. 50-kHz-rate 2D imaging of temperature and H_2O concentration at the exhaust plane of a J85 engine using hyperspectral tomography. Opt Express 2013;21(1):1152–62.
[240] York T, McCann H, Ozanyan KB. Agile sensing systems for tomography. Sensors J IEEE 2011;11(12):3086–105.
[241] Nasim H, Jamil Y. Recent advancements in spectroscopy using tunable diode lasers. Laser Phys Lett 2013;10(4):043001.
[242] Nasim H, Jamil Y. Diode lasers: from laboratory to industry. Opt Laser Technol 2014;56:211–22.
[243] Zeller W, Naehle L, Fuchs P, Gerschuetz F, Hildebrandt L, Koeth J. DFB lasers between 760 nm and 16 μm for sensing applications. Sensors 2010;10(4):2492–510.
[244] Klotzkin DJ. Introduction to semiconductor lasers for optical communications. New York, USA: Springer; 2014.
[245] Morgan RA. Vertical-cavity surface-emitting lasers: present and future. Photonics West'97; 1997.
[246] Witzel O, Klein A, Meffert C, Wagner S, Kaiser S, Schulz C, Ebert V. VCSEL-based, high-speed, in situ TDLAS for in-cylinder water vapor measurements in IC engines. Opt Express 2013;21(17):19951–65.
[247] Hult J, Burns IS, Kaminski CF. High repetition-rate wavelength tuning of an extended cavity diode laser for gas phase sensing. Appl Phys B 2005;81(6):757–60.
[248] Lynch S, Chen F, Gates J, Holmes C, Staines S, James S, Hodgkinson J, Smith P, Tatam R. Bragg-grating-stabilized external cavity lasers for gas sensing using tunable diode laser spectroscopy. SPIE OPTO; 2014.
[249] Wright P, Ozanyan KB, Carey SJ, McCann H. Design of high-performance photodiode receivers for optical tomography. Sensors J IEEE 2005;5(2):281–8.
[250] Belotti C, Cuccoli F, Facheris L, Vaselli O. An application of tomographic reconstruction of atmospheric CO_2 over a volcanic site based on open-path IR laser measurements. IEEE T Geosci Remote 2003;41(11):2629–37.
[251] Best P, Chien P, Carangelo R, Solomon P, Danchak M, Ilovici I. Tomographic reconstruction of FT-IR emission and transmission spectra in a sooting laminar diffusion flame: species concentrations and temperatures. Combust Flame 1991;85(3):309–18.
[252] Hall RJ, Bonczyk PA. Sooting flame thermometry using emission/absorption tomography. Appl Optics 1990;29(31):4590–8.
[253] Bennett KE, Byer RL. Fan-beam-tomography noise theory. JOSA A 1986;3(5):624–33.
[254] Liu C, Xu L, Chen J, Cao Z, Lin Y, Cai W. Development of a fan-beam TDLAS-based tomographic sensor for rapid imaging of temperature and gas concentration. Opt Express 2015;23(17):22494–511.
[255] Twynstra MG, Daun KJ. Laser-absorption tomography beam arrangement optimization using resolution matrices. Appl Optics 2012;51(29):7059–68.
[256] Wood MP, Ozanyan KB. Optimisation of a tomography sensor for imaging of temperature in a gas turbine engine. Sensors J IEEE 2013: 1–4.
[257] Song J, Hong Y, Pan H, Wang G. Beam arrangement on two-dimensional temperature reconstruction based on laser absorption spectroscopy. ISPDI 2013-fifth international symposium on photoelectronic detection and imaging; 2013.
[258] Tsekenis S, Tait N, McCann H. Spatially resolved and observer-free experimental quantification of spatial resolution in tomographic images. Rev Sci Instrum 2015;86(3):035104.
[259] Xu L, Liu C, Zheng D, Cao Z, Cai W. Digital signal processor-based high-precision on-line Voigt lineshape fitting for direct absorption spectroscopy. Rev Sci Instrum 2014;85(12):123108.
[260] Shimizu S, Sakai S. High-speed tomography for simultaneous measurement of the histories of two-dimensional distributions of temperature and density of burnt gases. JSME Int J B-Fluid T 1994;37(3):596–603.
[261] Tsekenis SA. High speed chemical species tomography for advanced fuels and engines Ph.D. thesis. University of Manchester; 2013.
[262] Dupont S, Kiwanuka SS, Hooper LE, Knight JC, Keiding SR, Kaminski CF. Low noise all-normal dispersion PCF utilised for rapid sweeping spectroscopy. Laser Phys. Lett. 2014;11:075601.

[263] Watt R, Kaminski C, Hult J. High bandwidth H2O absorption spectroscopy in a flame using a dispersed supercontinuum source. In: Conference on lasers and electro-optics; 2008.
[264] Watt R, Kaminski C, Hult J. Generation of supercontinuum radiation in conventional single-mode fibre and its application to broadband absorption spectroscopy. Appl Phys B 2008;90(1):47–53.
[265] Kaminski C, Watt R, Elder A, Frank J, Hult J. Supercontinuum radiation for applications in chemical sensing and microscopy. Appl Phys B 2008;92(3):367–78.
[266] Hult J, Watt RS, Kaminski CF. Dispersion measurement in optical fibers using supercontinuum pulses. J Lightwave Technol 2007;25(3):820–4.
[267] Hult J, Watt RS, Kaminski CF. High bandwidth absorption spectroscopy with a dispersed supercontinuum source. Opt Express 2007;15(18):11385–95.
[268] Welzel S, Hempel F, Hübner M, Lang N, Davies PB, Röpcke J. Quantum cascade laser absorption spectroscopy as a plasma diagnostic tool: an overview. Sensors 2010;10(7):6861–900.
[269] Curl RF, Capasso F, Gmachl C, Kosterev AA, McManus B, Lewicki R, Pusharsky M, Wysocki G, Tittel FK. Quantum cascade lasers in chemical physics. Chem Phys Lett 2010;487(1):1–18.
[270] Kim C, Kim M, Abell J, Bewley W, Merritt C, Canedy C, Vurgaftman I, Meyer J. Mid-IR distributed-feedback interband cascade lasers. SPIE OPTO; 2013.
[271] Goldenstein CS, Strand CL, Schultz IA, Sun K, Jeffries JB, Hanson RK. Fitting of calibration-free scanned-wavelength-modulation spectroscopy spectra for determination of gas properties and absorption lineshapes. Appl Optics 2014;53(3):356–67.
[272] Goldenstein C, Spearrin R, Schultz I, Jeffries J, Hanson R. Wavelength-modulation spectroscopy near 1.4 μm for measurements of H_2O and temperature in high-pressure and-temperature gases. Meas Sci Technol 2014;25(5):055101.
[273] Sur R, Sun K, Jeffries JB, Hanson RK, Pummill RJ, Waind T, Wagner DR, Whitty KJ. TDLAS-based sensors for in situ measurement of syngas composition in a pressurized, oxygen-blown, entrained flow coal gasifier. Appl Phys B 2013: 1–10.
[274] Goldenstein C, Spearrin R, Jeffries J, Hanson R. Wavelength-modulation spectroscopy near 2.5 μm for H_2O and temperature in high-pressure and-temperature gases. Appl Phys B 2014: 1–12.
[275] Sun K. Ultilization of multiple harmonics of wavelength modulation spectroscopy for practical gas sensing Ph.D. thesis. Stanford University; 2013.
[276] Sun K, Chao X, Sur R, Goldenstein C, Jeffries J, Hanson R. Analysis of calibration-free wavelength-scanned wavelength modulation spectroscopy for practical gas sensing using tunable diode lasers. Meas Sci Technol 2013;24(12):125203.
[277] Yu G, Li J, Chang X, Chen L, Sung C. Investigation of kerosene combustion characteristics with pilot hydrogen in model supersonic combustors. J Propul Power 2001;17(6):1263–72.
[278] Cai W, Kaminski CF. Multiplexed absorption tomography with calibration-free wavelength modulation spectroscopy. Appl Phys Lett 2014;104(15):154106.
[279] Dudley JM, Genty G, Coen S. Supercontinuum generation in photonic crystal fiber. Rev Mod Phys 2006;78(4):1135.
[280] Bernhardt B, Sorokin E, Jacquet P, Thon R, Becker T, Sorokina I, Picqué N, Hänsch TW. Mid-infrared dual-comb spectroscopy with 2.4 μm Cr2+: ZnSe femtosecond lasers. Appl Phys B 2010;100(1):3–8.
[281] Baumann E, Giorgetta F, Swann W, Zolot A, Coddington I, Newbury N. Spectroscopy of the methane ν_3 band with an accurate midinfrared coherent dual-comb spectrometer. Phys Rev A 2011;84(6):062513.
[282] Ideguchi T, Poisson A, Guelachvili G, Picqué N, Hänsch TW. Adaptive real-time dual-comb spectroscopy. Nat Commun 2014;5.
[283] Huber R, Adler DC, Fujimoto JG. Buffered Fourier domain mode locking: unidirectional swept laser sources for optical coherence tomography imaging at 370,000 lines/s. Opt Lett 2006;31(20):2975–7.
[284] Huber R, Wojtkowski M, Fujimoto J. Fourier domain mode locking (FDML): a new laser operating regime and applications for optical coherence tomography. Opt Express 2006;14(8):3225–37.
[285] Jeon MY, Zhang J, Wang Q, Chen Z. High-speed and wide bandwidth Fourier domain mode-locked wavelength swept laser with multiple SOAs. Opt Express 2008;16(4):2547–54.
[286] Kranendonk LA, An X, Caswell AW, Herold RE, Sanders ST, Huber R, Fujimoto JG, Okura Y, Urata Y. High speed engine gas thermometry by Fourier-domain mode-locked laser absorption spectroscopy. Opt Express 2007;15(23):15115–28.
[287] Li H. Near-infrared diode laser absorption spectroscopy with applications to reactive systems and combustion control Ph.D. thesis. Stanford University; 2007.
[288] Silver JA. Frequency-modulation spectroscopy for trace species detection: theory and comparison among experimental methods. Appl Optics 1992;31(6):707–17.
[289] Philippe LC, Hanson RK. Laser diode wavelength-modulation spectroscopy for simultaneous measurement of temperature, pressure, and velocity in shock-heated oxygen flows. Appl Optics 1993;32(30):6090–103.
[290] Rieker GB, Jeffries JB, Hanson RK, Mathur T, Gruber MR, Carter CD. Diode laser-based detection of combustor instabilities with application to a scramjet engine. P Combust Inst 2009;32(1):831–8.
[291] Sun K, Chao X, Sur R, Jeffries J, Hanson R. Wavelength modulation diode laser absorption spectroscopy for high-pressure gas sensing. Appl Phys B 2013;110(4):497–508.
[292] Steihaug T. The conjugate gradient method and trust regions in large scale optimization. SIAM J Numer Anal 1983;20(3):626–37.
[293] Andrei N. Scaled conjugate gradient algorithms for unconstrained optimization. Comput Optim Appl 2007;38(3):401–16.
[294] Cai W, Ma L. Applications of critical temperature in minimizing functions of continuous variables with simulated annealing algorithm. Comput Phys Commun 2010;181:11–6.
[295] Leite JPB, Topping BHV. Parallel simulated annealing for structural optimization. Comput Struct 1999;73(1-5):545–64.
[296] Ingber L. Simulated annealing - practice versus theory. Math Comput Model 1993;18(11):29–57.
[297] Ingber L. Very fast simulated re-annealing. Math Comput Model 1989;12:967.
[298] Corana A, Marchesi M, Martini C, Ridella S. Minimizing multimodal functions of continuous-variables with the simulated annealing algorithm. ACM Trans Math Softw 1987;13(3):262–80.
[299] Goldberg DE. Genetic algorithms in search, optimization and machine learning. Boston, USA: Addison-Wesley Longman Publishing Co., Inc.; 1989.
[300] Karr CL, Weck B, Freeman LM. Solutions to systems of nonlinear equations via a genetic algorithm. Eng Appl Artif Intel 1998;11(3):369–75.
[301] Deb K, Agrawal S. Understanding interactions among genetic algorithm parameters. Foundations of genetic algorithms. San Mateo, CA, USA: Morgan Kauffman; 1999. p. 265–86.
[302] Das S, Abraham A, Konar A. Particle swarm optimization and differential evolution algorithms: technical analysis, applications and hybridization perspectives. Advances of computational intelligence in industrial systems. Springer; 2008. p. 1–38.
[303] Storn R, Price K. Differential evolution–a simple and efficient heuristic for global optimization over continuous spaces. J Global Optim 1997;11(4):341–59.
[304] Storn R, Price K. Minimizing the real functions of the ICEC'96 contest by differential evolution. In: Proceedings of IEEE international conference on evolutionary computation; 1996.
[305] Cai W, Ma L. Hyperspectral tomography based on proper orthogonal decomposition as motivated by imaging diagnostics of unsteady reactive flows. Appl Optics 2010;49(4):601–10.
[306] Ma L, Cai W. Determination of the optimal regularization parameters in hyperspectral tomography. Appl Optics 2008;47(23):4186–92.
[307] Twomey S, Howell HB. Some aspects of the optical estimation of microstructure in fog and cloud. Appl Optics 1967;6(12):2125–31.
[308] Hansen PC. Numerical tools for analysis and solution of Fredholm integral equations of the first kind. Inverse Probl 1992;8(6):849.
[309] Hansen PC. Analysis of discrete ill-posed problems by means of the L-curve. SIAM Rev 1992;34(4):561–80.
[310] Golub GH, Heath M, Wahba G. Generalized cross-validation as a method for choosing a good ridge parameter. Technometrics 1979;21(2):215–23.
[311] Press WH, Teukolsky SA, Vetterling WT, Flannery BP. Numerical recipes in FORTRAN: the art of scientific computing. New York, USA: Cambridge University Press; 1992.
[312] Lin M, Li X, Cai W, Roy S, Gord JR, Sanders ST. Selection of multiple optimal absorption transitions for nonuniform temperature sensing. Appl Spectrosc 2010;64(11):1274–82.
[313] Huber R, Wojtkowski M, Taira K, Fujimoto J, Hsu K. Amplified, frequency swept lasers for frequency domain reflectometry and OCT imaging: design and scaling principles. Opt Express 2005;13(9):3513–28.
[314] Eigenwillig CM, Wieser W, Todor S, Biedermann BR, Klein T, Jirauschek C, Huber R. Picosecond pulses from wavelength-swept continuous-wave Fourier domain mode-locked lasers. Nat Commun 2013;4:1848.
[315] Agrawal GP. Nonlinear fiber optics. New York, USA: Springer; 2000.
[316] An X, Kraetschmer T, Takami K, Sanders ST, Ma L, Cai W, Li X, Roy S, Gord JR. Validation of temperature imaging by H_2O absorption spectroscopy using hyperspectral tomography in controlled experiments. Appl Optics 2011;50(4):A29–37.
[317] Liu JN, Wang BX, Cui YY, Wang HY. Ultrasonic tomographic velocimeter for visualization of axial flow fields in pipes. Flow Meas Instrum 2015;41:57–66.
[318] Binley A, Shaw B, Henrypoulter S. Flow pathways in porous media: electrical resistance tomography and dye staining image verification. Meas Sci Technol 1996;7(3):384–90 (7).
[319] Kumar M, Kumar V, Shakher C. Measurement of temperature and temperature distribution in diffusion flames using digital speckle pattern interferometry. Eleventh international conference on correlation optics; 2013.
[320] Harley JL, Rankin BA, Blunck DL, Gore JP, Gross KC. Imaging Fourier-transform spectrometer measurements of a turbulent nonpremixed jet flame. Opt Lett 2014;39(8):2350–3.